Article

Neuron

Molecular Mechanisms of Synaptic Vesicle Priming by Munc13 and Munc18

Highlights

- Munc13-1 has a function independent from Munc18-1
- Munc13-1 and Munc18-1 cooperate to promote proper SNARE complex assembly
- Proper SNARE complex assembly yields near-physiological Ca^{2+} sensitivity in vitro
- Bypass of Munc13 in neurons with an open mutant of syntaxin is incomplete

Authors

Ying Lai, Ucheor B. Choi, Jeremy Leitz, ..., Nils Brose, JeongSeop Rhee, Axel T. Brunger

Correspondence

brunger@stanford.edu

In Brief

Lai et al. discovered that Munc13 promotes proper SNARE complex assembly together with Munc18, increasing evoked release probability. This suggests that the physiological functions of Munc13 in priming and short-term presynaptic plasticity are related to regulation of proper assembly of synaptic complexes.

Lai et al., 2017, Neuron *95*, 591–607
August 2, 2017
http://dx.doi.org/10.1016/j.neuron.2017.07.004

CellPress

Neuron
Article

Molecular Mechanisms of Synaptic Vesicle Priming by Munc13 and Munc18

Ying Lai,[1,2,3,4,5,7] Ucheor B. Choi,[1,2,3,4,5,7] Jeremy Leitz,[1,2,3,4,5] Hong Jun Rhee,[6] Choongku Lee,[6] Bekir Altas,[6] Minglei Zhao,[1,2,3,4,5] Richard A. Pfuetzner,[1,2,3,4,5] Austin L. Wang,[1,2,3,4,5] Nils Brose,[6] JeongSeop Rhee,[6] and Axel T. Brunger[1,2,3,4,5,8,*]

[1]Department of Molecular and Cellular Physiology
[2]Department of Neurology and Neurological Sciences
[3]Department of Structural Biology
[4]Department of Photon Science
[5]Howard Hughes Medical Institute
Stanford University, Stanford, CA 94305, USA
[6]Department of Molecular Neurobiology, Max Planck Institute for Experimental Medicine, 37075 Göttingen, Germany
[7]These authors contributed equally
[8]Lead Contact
*Correspondence: brunger@stanford.edu
http://dx.doi.org/10.1016/j.neuron.2017.07.004

SUMMARY

Munc13 catalyzes the transit of syntaxin from a closed complex with Munc18 into the ternary SNARE complex. Here we report a new function of Munc13, independent of Munc18: it promotes the proper syntaxin/synaptobrevin subconfiguration during assembly of the ternary SNARE complex. In cooperation with Munc18, Munc13 additionally ensures the proper syntaxin/SNAP-25 subconfiguration. In a reconstituted fusion assay with SNAREs, complexin, and synaptotagmin, inclusion of both Munc13 and Munc18 quadruples the Ca^{2+}-triggered amplitude and achieves Ca^{2+} sensitivity at near-physiological concentrations. In Munc13-1/2 double-knockout neurons, expression of a constitutively open mutant of syntaxin could only minimally restore neurotransmitter release relative to Munc13-1 rescue. Together, the physiological functions of Munc13 may be related to regulation of proper SNARE complex assembly.

INTRODUCTION

Membrane fusion of synaptic vesicles is an essential process for neurotransmitter release in the nervous system (Südhof, 2013; Rothman, 2014). The synaptic fusion machinery includes the neuronal SNARE (soluble NSF-attachment protein receptor) proteins synaptobrevin-2/VAMP2 (vesicle-associated membrane protein 2), syntaxin-1, and SNAP-25 (synaptosomal-associated protein 25); together, they form a *trans* ternary (syntaxin-1/SNAP-25/synaptobrevin-2) SNARE complex, bringing the synaptic vesicle and plasma membranes into close juxtaposition and ultimately providing the energy for membrane fusion (Sutton et al., 1998; Weber et al., 1998). The Ca^{2+} sensor synaptotagmin is essential for evoked neurotransmission (Geppert et al., 1994; Fernández-Chacón et al., 2001). The main isoform involved in fast synchronous release, synaptotagmin-1, forms a conserved, Ca^{2+}-independent "primary" interface with the neuronal ternary SNARE complex (Zhou et al., 2015). Complexin-1, a small cytosolic protein abundant in the presynaptic terminal (McMahon et al., 1995), cooperates with synaptotagmin-1 to activate Ca^{2+}-triggered neurotransmitter release, and it also regulates spontaneous neurotransmitter release (Mohrmann et al., 2015; Trimbuch and Rosenmund, 2016). In addition to the primary interface, another synaptotagmin-1 molecule forms a tripartite interface with both the SNARE complex and complexin-1 (Zhou et al., 2017).

Prior to Ca^{2+}-triggered neurotransmitter release, synaptic vesicles are "primed," a process that enables the synaptic vesicles to undergo fast-triggered fusion, i.e., to be "readily releasable" upon the arrival of an action potential. Munc13-1 and its homologs are primarily brain-specific, cytoplasmic proteins in the presynaptic terminal that are involved in synaptic vesicle priming and short-term synaptic plasticity (Südhof, 2012, 2013). Neurons in mice lacking Munc13-1 exhibit severely limited activity-dependent neurotransmitter release as well as hypertonic sucrose stimulation that causes fusion of all readily releasable synaptic vesicles (Augustin et al., 1999). Mutation of *unc-13* in *C. elegans* (Richmond et al., 1999) and elimination of *Dunc-13* in *Drosophila* (Aravamudan et al., 1999) also abolish neurotransmitter release. Munc13-1 and Munc13-2 double-knockout mice have essentially no release-competent synaptic vesicles (Varoqueaux et al., 2002) and exhibit a severe docking defect (Imig et al., 2014).

In addition to Munc13, Sec1/Munc18 (SM) proteins are also required components of all membrane trafficking pathways as exemplified by the block of synaptic vesicle fusion upon Munc18-1 knockout in mice (Verhage et al., 2000). Upon disassembly of SNARE complexes with N-ethylmaleimide-sensitive factor (NSF) and αSNAP (soluble NSF adaptor protein), Munc18-1 captures syntaxin-1A, locking it into a "closed" conformation and preventing reassembly of the ternary SNARE complex (Ma et al., 2013). Munc18-1 binds tightly (K_d ~1–4 nM) to syntaxin-1A, in which its Habc domain interacts in a *cis* conformation with its SNARE domain (Misura et al., 2000;

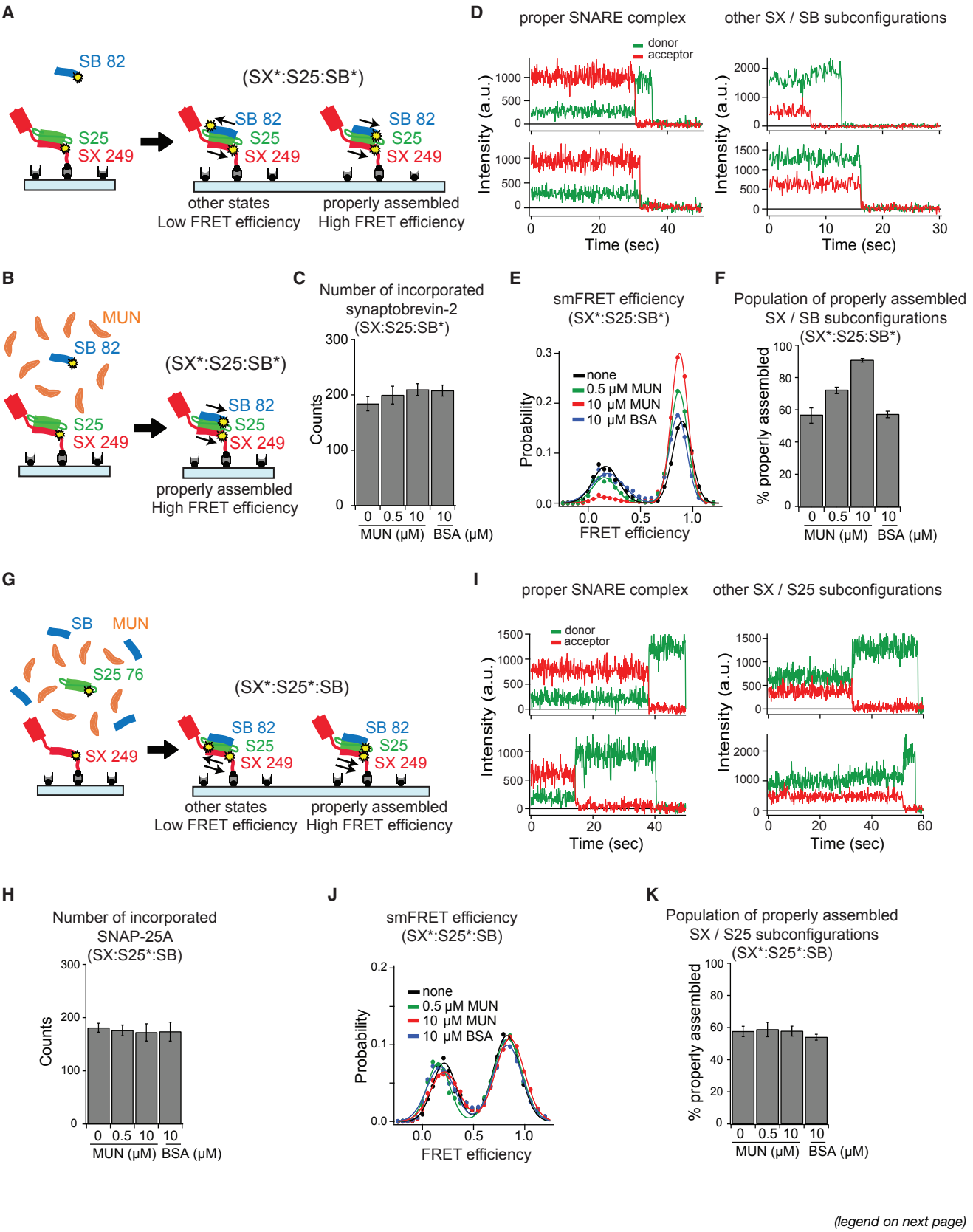

(legend on next page)

Chen et al., 2008), in turn hindering reassembly of SNARE complexes (Pevsner et al., 1994; Yang et al., 2000).

Munc13-1 contains a C1 domain, three C2 domains (C2A, C2B, and C2C), and an MUN domain. The MUN domain of Munc13-1 (amino acid range 859–1,531) catalyzes the transit of syntaxin-1A from the syntaxin-1A/Munc18-1 complex into the ternary SNARE complex (Basu et al., 2005; Ma et al., 2013; Yang et al., 2015). Earlier studies in *C. elegans* suggested a similar function of full-length *unc-13* (Richmond et al., 2001), although the role of the MUN domain has not been directly studied in that system. The so-called LE mutant of syntaxin-1A (syntaxin-1A^{LE}) (Dulubova et al., 1999) bypasses the requirement of Munc13-1 for the transit of syntaxin-1A into the ternary SNARE complex in the presence of SNAP-25A and synaptobrevin-2 in vitro (Ma et al., 2011). It accomplishes this by preferentially adopting an open conformation of syntaxin-1A (Figure 4G in Wang et al., 2017). However, this open syntaxin-1A mutant can only partially restore neurotransmitter release in *unc-13* mutants of *C. elegans* (Hammarlund et al., 2007).

Here we report a new additional molecular function of Munc13-1: the MUN domain of Munc13-1 promotes the proper syntaxin-1A/synaptobrevin-2 arrangement within the ternary SNARE complex when it is assembled from the syntaxin-1A/SNAP-25A complex via addition of synaptobrevin-2 in vitro. Moreover, when starting from the syntaxin-1A/Munc18-1 complex, Munc13-1 additionally ensures formation of the proper syntaxin-1A/SNAP-25A arrangement in the presence of SNAP-25A and synaptobrevin-2, i.e., Munc13-1 and Munc18-1 act together to ensure the proper assembly of the entire ternary SNARE complex. Inclusion of the MUN domain or the larger C1C2BMUN or C1C2BMUNC2C fragments of Munc13-1 in a fusion assay approximately quadrupled the Ca^{2+}-triggered fusion response. When Munc18-1 was included as well, the sensitivity of the assay for Ca^{2+}-triggered fusion reached the physiological range.

RESULTS

Munc13-1 Promotes the Proper Syntaxin-1A/Synaptobrevin-2 Subconfiguration

The properly assembled SNARE complex consists of a parallel four-helix bundle (Sutton et al., 1998). However, interacting SNARE domains can assume alternative configurations when the components are mixed in the absence of other factors that assist proper complex formation (Brunger, 2005). In particular, improperly assembled ternary SNARE complexes, including antiparallel configurations, have been observed (Weninger et al., 2003; Choi et al., 2016). These alternative "subconfigurations" are probably kinetically trapped dead-end states. The question arises how the neuronal *trans* ternary SNARE complex is properly assembled in vivo.

The syntaxin-1A/SNAP-25A complex is a starting point for the assembly of *trans* ternary SNARE complex (Fasshauer and Margittai, 2004; Weninger et al., 2008), although other complexes have also been implicated as possible starting points or intermediates (Woodbury and Rognlien, 2000; Chen et al., 2001; Ma et al., 2013). We used single-molecule fluorescence resonance energy transfer (smFRET) experiments to monitor the assembly of the ternary SNARE complex starting from surface-tethered syntaxin-1A/SNAP-25A complex (Figures 1A and 1B). Based on the crystal structure of the neuronal SNARE complex (PDB: 1SFC) (Sutton et al., 1998), we chose labeling sites for syntaxin-1A and synaptobrevin-2 such that the fluorescent label pair should produce high FRET efficiency upon proper assembly of the ternary SNARE complex. The cytoplasmic domain of synaptobrevin-2 was then added to form ternary SNARE complex in the absence (Figure 1A) or presence (Figure 1B) of the MUN domain at the specified concentration, or alternatively with BSA as a control.

Labeled synaptobrevin-2 was readily incorporated into ternary SNARE complex starting from the syntaxin-1A/SNAP-25A complex regardless of the presence of the MUN domain or BSA control (Figure 1C; Table S1). Next we examined the FRET efficiency of the label pairs to probe the syntaxin-1A/synaptobrevin-2 subconfiguration within the ternary SNARE complex (Figures 1D–1F; Table S2). In the absence of the MUN domain, two distinct FRET efficiency states emerged: a high FRET efficiency state that corresponds to the ternary SNARE complex with the proper parallel syntaxin-1A/synaptobrevin-2 subconfiguration, and a low FRET efficiency state that corresponds to other syntaxin-1A/synaptobrevin-2 subconfigurations, including antiparallel arrangements (Figures 1A and 1D) (Weninger et al., 2003). The stoichiometry of both properly

Figure 1. The MUN Domain Alone Promotes the Proper Syntaxin-1A/Synaptobrevin-2 Subconfiguration, but Not the Syntaxin-1A/SNAP-25A Subconfiguration

(A, B, and G) The syntaxin-1A (SX)/synaptobrevin-2 (SB) and the syntaxin-1A/SNAP-25A (S25) subconfigurations of the ternary SNARE complex were probed by single-molecule experiments. The yellow dots and the asterisks (*) indicate fluorescently labeled residues. The cytoplasmic domain of SX was tethered on a PEG-passivated microscope slide via streptavidin-biotin linkage and labeled with Alexa 647 at residue 249. The cytoplasmic domain of SB was labeled with Alexa 555 at residue 82 and S25 was labeled with Alexa 555 at residue 76. The thin arrows represent parallel or antiparallel SX/SB (A and B) or SX/S25 (G) subconfigurations.

(A and B) Beginning with surface-tethered SX, the binary complex with S25 was first formed, and then SB was added in the absence (A) or in the presence (B) of the MUN domain at the specified concentration or BSA control.

(G) Beginning with surface-tethered SX, the ternary SNARE complex was formed by adding S25 and SB at the same time in the presence of the MUN domain at the specified concentration or BSA control.

(C and H) Mean counts from three fields of view ± SD (Table S1) of SB (C) or S25 (H) incorporation into the ternary SNARE complex in presence of the MUN domain at the specified concentrations or BSA control.

(D and I) Representative fluorescence intensity time traces of properly (left panels) and improperly (right panels) assembled SNARE complexes that were formed starting from surface-tethered SX/S25 complex (D) or from surface-tethered SX molecules (I) in the absence of the MUN domain.

(E and J) smFRET efficiency histograms using labeled SB (E) or S25 (J).

(F and K) Percent of properly assembled SX/SB (F) or SX/S25 (K) subconfigurations. Shown are means ± SD for the two subsets of an equal partition of the data (Table S2).

and improperly assembled SNARE complexes is likely 1:1:1 (STAR Methods).

When the MUN domain was present during assembly of the ternary SNARE complex, the population of the low FRET efficiency state was reduced as a function of MUN domain concentration, with most of it being suppressed in the presence of 10 μM MUN domain (Figures 1E and 1F). In contrast, the BSA control did not suppress the low FRET efficiency population. Thus, the MUN domain promotes the proper syntaxin-1A/synaptobrevin-2 subconfiguration when the ternary SNARE complex is assembled by addition of synaptobrevin-2 to the syntaxin-1A/SNAP-25A complex in the presence of the MUN domain.

We next asked if the MUN domain could likewise promote the proper syntaxin-1A/SNAP-25A subconfiguration within the ternary SNARE complex when assembly is performed by addition of both SNAP-25A and synaptobrevin-2 to syntaxin-1A. Based on the crystal structure of the neuronal SNARE complex (PDB: 1SFC) (Sutton et al., 1998), we again designed fluorescent labeling sites on syntaxin-1A and SNAP-25A such that the label pair should produce high FRET efficiency when the ternary SNARE complex is properly assembled (Figure 1G). Labeled SNAP-25A was readily incorporated into ternary SNARE complex (Figure 1H; Table S1), regardless of the presence of the MUN domain or BSA control. Using this system, we probed the syntaxin-1A/SNAP-25A subconfiguration within the ternary SNARE complex (Figures 1I–1K; Table S2). The smFRET efficiency histogram showed two states regardless of the presence of the MUN domain or BSA control: a high FRET efficiency state that corresponds to the proper assembly of ternary SNARE complex with the proper parallel syntaxin-1A/SNAP-25A subconfiguration in the ternary SNARE complex, and a low FRET efficiency state that corresponds to other syntaxin-1A/SNAP-25A subconfigurations, such as antiparallel arrangements (Figure 1G) (Weninger et al., 2003) or situations where one of the SNAP-25A α helices is not fully incorporated into the ternary SNARE complex (Weninger et al., 2008). Thus, while the MUN domain alone promotes the proper syntaxin-1A/synaptobrevin-2 subconfiguration within the ternary SNARE complex, it has no effect on the proper syntaxin-1A/SNAP-25A subconfiguration.

The experiments presented in Figure 1 were performed without the involvement of Munc18-1, suggesting that the MUN domain has an autonomous function independent of Munc18-1. How does the MUN domain induce the proper syntaxin-1A/synaptobrevin-2 subconfiguration during assembly of the ternary SNARE complex? Previous reports showed that the MUN domain interacts with syntaxin-1A as well as with syntaxin-1A/SNAP-25A and ternary SNARE complexes (Guan et al., 2008; Weninger et al., 2008; Ma et al., 2011). However, these experiments did not address the possibility of interactions between the MUN domain and synaptobrevin-2. To re-investigate this question, we performed single-molecule binding experiments (Figures S1A–S1C) wherein the cytoplasmic domain of synaptobrevin-2 was labeled with the fluorescent dye Alexa 647 and tethered to a passivated surface. The MUN domain was labeled with the fluorescent dye Alexa 555 and added to the surface-tethered and labeled synaptobrevin-2 molecules. Alternating laser illumination was used to co-localize synaptobrevin-2 and MUN domain molecules. We observed transient binding events, as indicated by the stepwise increases in fluorescence intensity of the fluorescent label attached to the MUN domain (Figure S1A). We generated histograms of the bound and the unbound dwell times, and estimated the on and the off rates by fitting exponential functions to the histograms, respectively (Figures S1B and S1C). However, due to the low frequency of binding events over the observation period of 200 s and the high background of unbound MUN domain molecules at concentrations above 100 nM, the on rate and the resulting dissociation constant obtained by this method may be unreliable.

To further corroborate the binding of synaptobrevin-2 and the MUN domain, we performed bulk fluorescence anisotropy measurements to obtain an estimate of the dissociation constant (K_d). For this experiment, the cytoplasmic domain of synaptobrevin-2 was labeled with the fluorescent dye Alexa 488 and titrated with unlabeled MUN domain at different concentrations. The fluorescence anisotropy curves were fit to a Hill function, resulting in K_d ~109.9 ± 35.4 μM (red line in Figure S1D). To confirm the specificity of this interaction, we performed a competition experiment in the presence of 50 μM of unlabeled cytoplasmic domain of synaptobrevin-2, resulting in a substantial decrease of the binding with labeled synaptobrevin-2 molecules (black line in Figure S1D). For comparison with previously published binding experiments, we measured the interaction between syntaxin-1A and the MUN domain using the cytoplasmic domain of syntaxin-1A that was labeled with the fluorescent dye Alexa 488 (Figure S1E), resulting in K_d ~70.8 ± 5.9 μM, close to the previously published dissociation constant K_d ~46 μM (Ma et al., 2011).

The MUN Domain Nearly Quadruples Ca^{2+}-Triggered Vesicle Fusion

Since the MUN domain promotes formation of the proper syntaxin-1A/synaptobrevin-2 subconfiguration within the ternary SNARE complex, we asked if this property of the MUN domain has functional consequences in Ca^{2+}-triggered vesicle fusion. We investigated the effect of the MUN domain on Ca^{2+}-independent and Ca^{2+}-triggered fusion using a single-vesicle content mixing assay with reconstituted full-length neuronal SNAREs, synaptotagmin-1, and complexin-1 (Lai et al., 2014). Two types of vesicles were reconstituted: vesicles with reconstituted syntaxin-1A and SNAP-25A (referred to as PM vesicles) and vesicles with reconstituted synaptobrevin-2 and synaptotagmin-1 that mimic synaptic vesicles (referred to as SV vesicles) (Figure 2A; STAR Methods). The PM vesicles were tethered on a passivated surface after preincubation with the MUN domain (protocol "All" in Figure 2A and STAR Methods). After washing unbound PM vesicles, SV vesicles were added and incubated for a 1 min period, and then unbound SV vesicles were removed. Subsequently, Ca^{2+}-independent fusion was monitored for 1 min, followed by injection of 500 μM Ca^{2+}, after which Ca^{2+}-triggered fusion was monitored for an additional 1 min period. Complexin-1 was present when SV vesicles were added and in all subsequent stages.

Inclusion of 10 μM MUN domain in the fusion assay had no effect on the intrinsic Ca^{2+}-independent fusion probability (Figures 2B and S2A). We note that Ca^{2+}-independent fusion probabilities obtained from our in vitro fusion experiments are normalized with

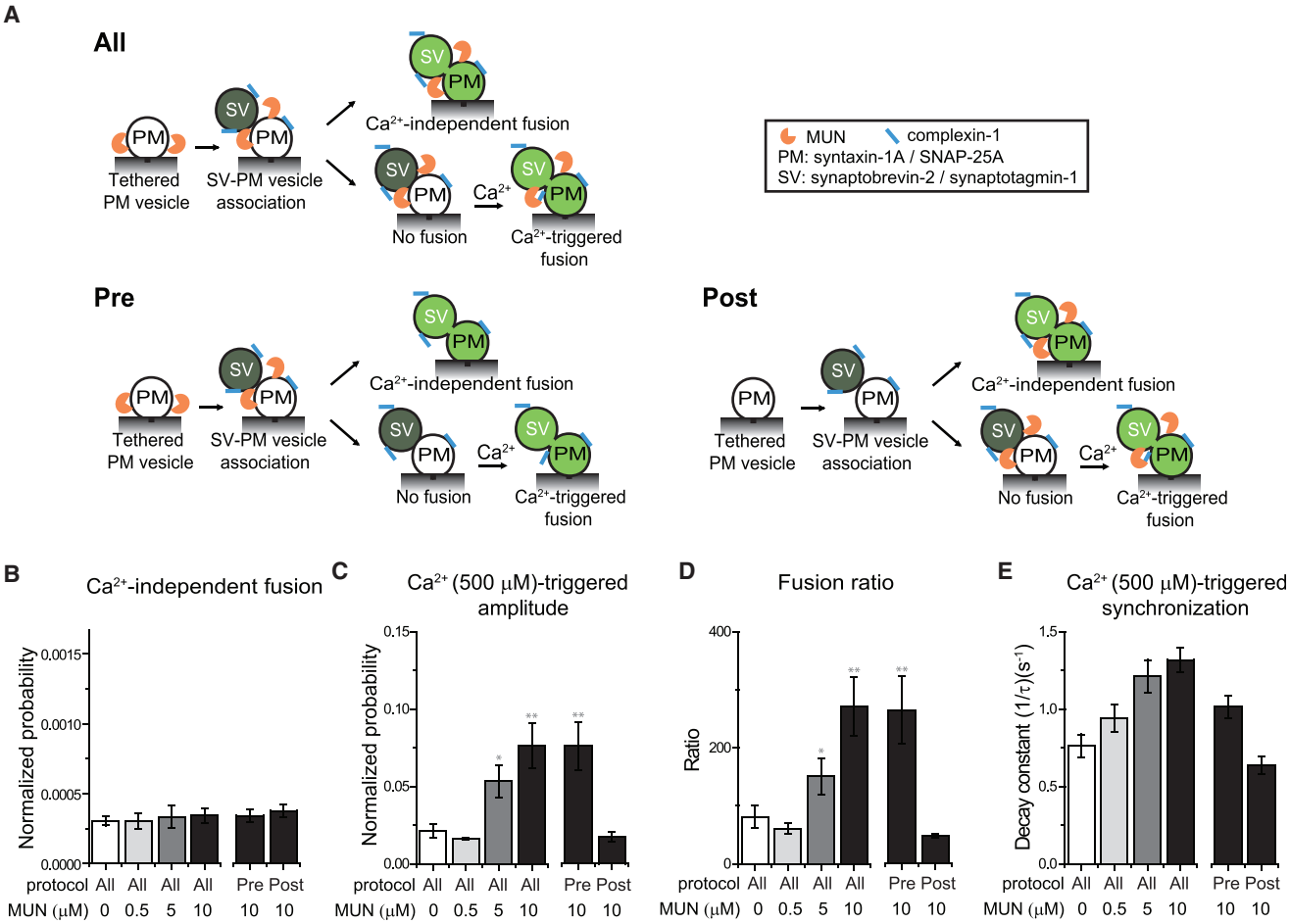

Figure 2. The MUN Domain Improves the Efficiency of Ca^{2+}-Triggered Fusion

(A) Single-vesicle content mixing assay. PM, plasma membrane mimic vesicles with reconstituted syntaxin-1A and SNAP-25A; SV, synaptic vesicle mimic with reconstituted synaptobrevin-2 and synaptotagmin-1. After SV-PM vesicle association, vesicle pairs either undergo Ca^{2+}-independent fusion or remain associated until fusion is triggered by Ca^{2+} addition. The MUN domain is only present during the specified stages. "0 μM MUN" refers to the absence of the MUN domain in all stages. In protocol "Pre" the MUN domain is only present before and during SV-PM vesicle association. In protocol "Post" the MUN domain is present only after SV-PM vesicle association.

(B–E) The bar graphs show the effects of MUN domain on the average probability of Ca^{2+}-independent fusion events per second (B), the amplitude of the first 1 s time bin upon 500 μM Ca^{2+} injection (C), the ratio of the Ca^{2+}-triggered amplitude to the average probability of Ca^{2+}-independent fusion per second (D), and the decay rate ($1/\tau$) of the Ca^{2+}-triggered fusion histogram (E). The fusion probabilities and amplitudes were normalized to the number of analyzed SV-PM vesicle pairs (Table S3). Individual histograms are in Figures S2A and S2F. (B)–(D) show means ± SD for multiple independent repeat experiments (Table S3).

(E) Decay constants and error estimates computed from the covariance matrix upon fitting the corresponding histograms with a single exponential decay function using the Levenberg-Marquardt algorithm. *$p < 0.05$, **$p < 0.01$ by Student's t test, compared to the experiment without the MUN domain.

respect to the number of associated vesicles. In contrast, the frequency of spontaneous (mini) release that is measured in electrophysiological experiments depends on both the number of functional synapses as well as the number of synaptic vesicles that are capable of undergoing spontaneous fusion. Moreover, spontaneous fusion in neurons likely depends on another Ca^{2+} sensor that is presently not included in our fusion assay (Xu et al., 2009; Zhou et al., 2017). Therefore, our observed Ca^{2+}-independent vesicle fusion does not necessarily correlate to spontaneous mini release in vivo.

The presence of the MUN domain increased the probability of fast Ca^{2+}-triggered fusion (i.e., the Ca^{2+}-triggered amplitude) by a factor of 3.6 (Figures 2C and S2F; Table S3). We also observed an increase in the ratio of the Ca^{2+}-triggered amplitude to the average probability of Ca^{2+}-independent fusion per second (referred to as "fusion ratio") by a factor of 3.3 (Figure 2D), and increased the synchronization (decay constant) by a factor of 1.7 (Figure 2E). These increases were dependent on the concentration of the MUN domain.

We next asked if the presence of the MUN domain upon Ca^{2+} triggering plays a direct role in Ca^{2+}-triggered fusion. Considering the weak affinity of the MUN domain to SNARE complexes (Guan et al., 2008; Weninger et al., 2008; Ma et al., 2011), we hypothesized that extensive washing could remove any bound MUN domain. Therefore, we repeated the fusion experiment but extensively washed the SV-PM vesicles with

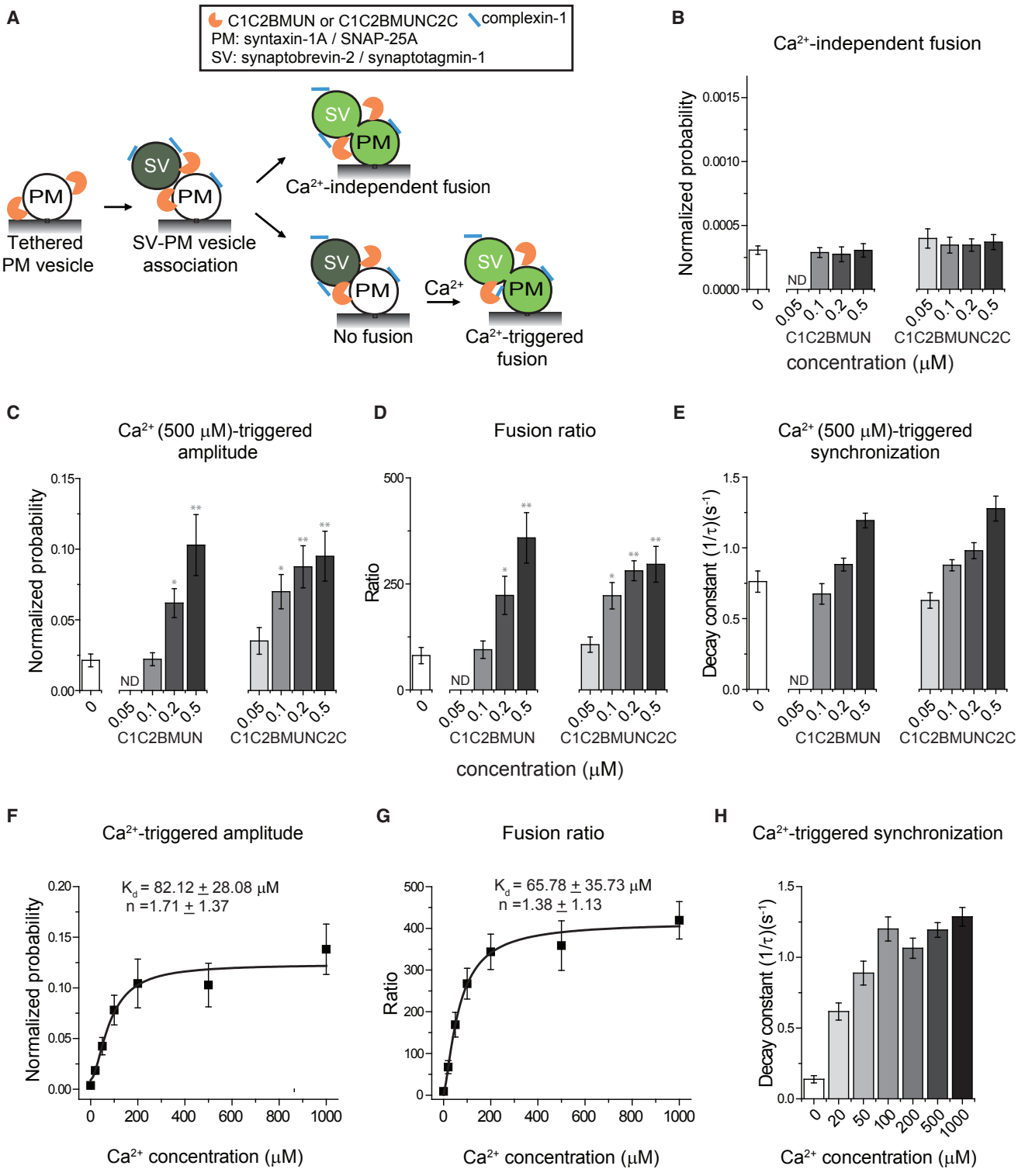

Figure 3. The C1C2BMUN and C1C2BMUNC2C Fragments Improve the Efficiency of Ca^{2+}-Triggered Fusion

(A) The experimental scheme is identical to that shown in Figure 2A, protocol "all," except that the C1C2BMUN or the C1C2BMUNC2C fragment is used instead of the MUN domain.

(B–E) The bar graphs show the effects of the C1C2BMUN or the C1C2BMUNC2C fragment on the average probability of Ca^{2+}-independent fusion events per second (B), the amplitude of the first 1 s time bin upon Ca^{2+} injection (C), the ratio of the Ca^{2+}-triggered amplitude to the average probability of Ca^{2+}-independent fusion per second (D), and the decay rate ($1/\tau$) of the histogram upon Ca^{2+} injection (E).

(legend continued on next page)

buffer that only contained complexin-1, but not the MUN domain, after vesicle association (protocol "Pre"; Figure 2A). We confirmed that this washing protocol removed all the MUN domain molecules that were present during vesicle association (Figure S3). The extensive washing protocol still increased the Ca^{2+}-triggered amplitude and the fusion ratio to levels similar to when the MUN domain is present at all stages (Figures 2C and 2D). Conversely, when the MUN domain was added only after vesicle association (protocol "Post"; Figure 2A), the Ca^{2+}-independent fusion rate, Ca^{2+}-triggered amplitude, the fusion ratio, and the Ca^{2+}-triggered synchronization were not changed from levels where the MUN domain was never present (Figures 2B–2E). Together these data suggest that the effect of the MUN domain on Ca^{2+}-triggered fusion is a consequence of promoting the proper syntaxin-1A/synaptobrevin-2 subconfiguration, rather than a direct effect on Ca^{2+}-triggered fusion itself.

The C1C2BMUN and C1C2BMUNC2C Fragments Act Similarly to the MUN Domain, but at Lower Concentrations

We next investigated the effect of the larger C1C2BMUN and C1C2BMUNC2C fragments (Liu et al., 2016; Xu et al., 2017) in our fusion assay. We used the same protocol as in Figure 2A, except that the MUN domain was replaced with one of these fragments at the specified concentrations (Figures 3A, S2B, S2G, and S4; Table S4). Similar to the MUN domain, inclusion of these fragments in the fusion assay had no effect on the intrinsic Ca^{2+}-independent fusion probability (Figure 3B), but increased the Ca^{2+}-triggered fusion amplitude by a factor of ~5, the fusion ratio by a factor of ~4, and the synchronization by a factor of ~1.6 (Figures 3C–3E). Moreover, inclusion of the C1C2BMUN and C1C2BMUNC2C fragments achieved similar effects to the MUN domain at 20- and 100-fold lower concentrations, respectively. As shown in Figure S5, inclusion of the C2C domain in the Munc13 fragment (i.e., C1C2BMUNC2C) increases vesicle association in vitro, consistent with an increase of the readily releasable pool (RRP) upon inclusion of the C2C domain as in neurons (Liu et al., 2016) and chromaffin cells (Stevens et al., 2005). However, due to a relatively low yield of purified C1C2BMUNC2C fragment, we used the C1C2BMUN fragment in all of the following experiments.

The C1 and C2B domains of Munc13-1 bind to DAG and PIP2, respectively (Rhee et al., 2002; Shin et al., 2010), both of which were included in the PM vesicles in the experiments shown above. Even at zero Ca^{2+} concentration, there is a weak but significant interaction between C2B and PIP2. When either DAG or both DAG and PIP2 were omitted from the PM vesicles, smaller effects of the C1C2BMUN fragment on Ca^{2+}-triggered fusion were observed (Figures S6C–S6E and S2H; Table S4), suggesting that the DAG-C1 and PIP2-C2B interactions cooperate in enhancing the effect of the C1C2BMUN fragment on Ca^{2+}-triggered fusion. However, even in the absence of both PIP2 and DAG, inclusion of 0.5 μM C1C2BMUN fragment in the fusion assay slightly increased the Ca^{2+}-triggered fusion amplitude and synchronization (Figures S6C–S6E).

In the absence of complexin-1, inclusion of the C1C2BMUN fragment in the fusion assay increased both the Ca^{2+}-independent fusion probability and the Ca^{2+}-triggered fusion amplitude (Figures S7, S2D, and S2I; Table S4). When complexin-1 is included as well, the Ca^{2+}-independent fusion probability is decreased while the Ca^{2+}-triggered fusion amplitude is greatly increased. Likewise, complexin-1 has similar effects on these fusion probabilities in the absence of C1C2BMUN. These experiments show that these two functions of complexin-1 are independent from the inclusion of Munc13-1 or the combination of Munc18-1 and Munc13-1 in the fusion assay.

In neurons, the Ca^{2+} sensitivity of synaptic vesicle fusion starts at ~10 μM and saturates at ~100 μM (Heidelberger et al., 1994; Schneggenburger and Neher, 2000). Yet the best Ca^{2+} sensitivity that we have been able to achieve in the past with our fusion assay was around 500 μM (Diao et al., 2012). We re-assessed the Ca^{2+} sensitivity of our fusion assay, but now in the presence of the C1C2BMUN fragment (Figures 3F–3H). We observed a substantial increase in Ca^{2+}-triggered fusion amplitude below 100 μM Ca^{2+}. Fitting the Ca^{2+}-triggered fusion amplitude and the fusion ratio to Hill functions produced half-maximal Ca^{2+} concentrations of 82 ± 28 μM for the Ca^{2+}-triggered fusion amplitude and 66 ± 36 μM for the fusion ratio. Although this is already a major improvement of our assay, we describe below how we achieved an even more substantial increase in Ca^{2+} sensitivity in our fusion assay.

Munc13-1 and Munc18-1 Cooperate to Properly Assemble the Ternary SNARE Complex

Instead of the syntaxin-1A/SNAP25A complex, the syntaxin-1A/Munc18-1 complex may serve as another starting point for ternary SNARE complex formation upon addition of synaptobrevin-2, SNAP-25, and Munc13-1 (Ma et al., 2013). We asked if the syntaxin-1A/Munc18-1 complex is also a good starting point for proper assembly of ternary SNARE complex. We again used single-molecule fluorescence microscopy in order to monitor the assembly of the ternary SNARE complex starting from the syntaxin-1A/Munc18-1 complex (Figures 4A and 4E). We subsequently assembled ternary SNARE complex by addition of SNAP-25A and synaptobrevin-2 in the presence or absence of the MUN domain.

We first assessed the incorporation of labeled synaptobrevin-2 (Figure 4B; Table S1) or labeled SNAP-25A (Figure 4F; Table S1) into ternary SNARE complex starting from the

(F–H) Ca^{2+} concentration dependence of triggered fusion in the presence of 500 nM C1C2BMUN fragment. Shown are the amplitude of the first 1 s time bin upon 500 μM Ca^{2+} injection (F), the ratio of the Ca^{2+}-triggered amplitude, and the average probability of Ca^{2+}-independent fusion per second (G). (F) and (G) were fit to Hill functions yielding the Ca^{2+} concentration at half occupation K_d and the Hill coefficient n. (H) Decay rate ($1/\tau$) of fusion histograms as a function of Ca^{2+}. The fusion probabilities and amplitudes were normalized to the number of analyzed SV-PM vesicle pairs (Table S4). Individual histograms are in Figures S2B and S2G. (B)–(D), (F), and (G) show means ± SD (Table S4). (E) and (H) show decay constants and error estimates computed from the covariance matrix upon fitting the corresponding histograms with a single exponential decay function using the Levenberg-Marquardt algorithm. *$p < 0.05$, **$p < 0.01$ by Student's t test, compared to the experiment without the C1C2BMUN fragment.

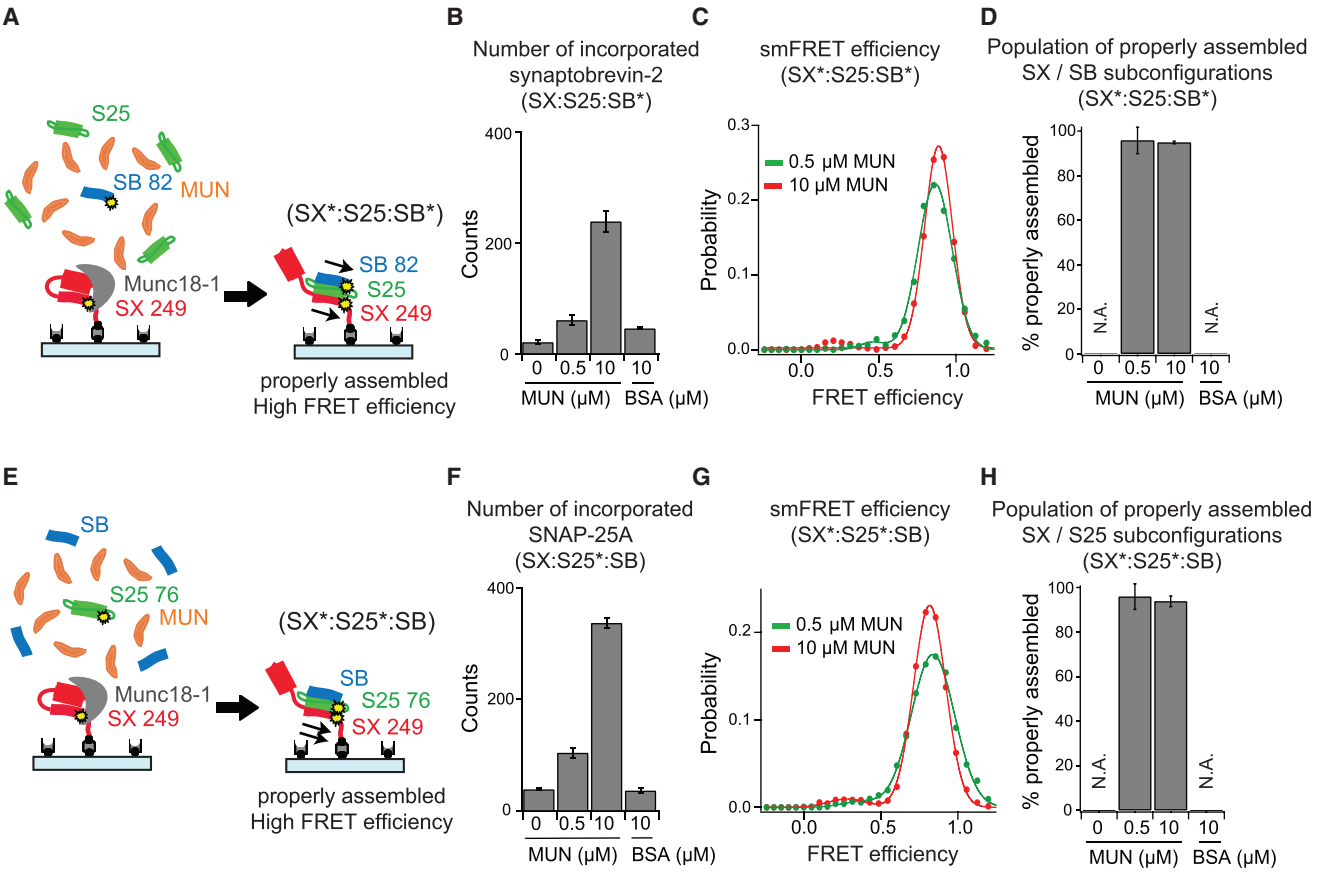

Figure 4. Munc13-1 and Munc18-1 Promote Proper Assembly of the Ternary SNARE Complex

(A and E) The configurations of the ternary SNARE complex were probed by single-molecule experiments. The cytoplasmic domain of syntaxin-1A (SX) was tethered on a PEG-passivated microscope slide via streptavidin-biotin linkage. Munc18-1 was added to assemble the SX/Munc18-1 complex. SNAP-25A (S25) and the cytoplasmic domain of synaptobrevin-2 (SB) were then added in the presence of the MUN domain at the specified concentration or BSA control. The yellow dots and the asterisks (*) indicate the fluorescently labeled residues. The thin arrows represent parallel SX/SB (A) or SX/S25 (E) subconfigurations. The labeling sites are SX residue 249, SB residue 82, and S25 residue 76.

(B) Beginning with surface-tethered SX/Munc18-1 complex, SB incorporation into the ternary SNARE complex was measured by counting the number of labeled (Alexa 555) SB molecules in the presence of unlabeled S25 and the MUN domain at the specified concentrations or BSA control.

(C) smFRET efficiency histograms for labels attached to SB (Alexa 555) and SX (Alexa 647) in the presence of MUN at the specified concentrations.

(D) Percent of properly assembled ternary SNARE subconfigurations.

(E–H) Similar to (A)–(D), starting from surface-tethered SX/Munc18-1 complex and forming ternary SNARE complex in the presence of unlabeled SB, labeled (Alexa 555) S25, and the MUN domain at the specified concentration or BSA control.

(B) and (F) show means of the counts from three fields of view ± SD; (D) and (H) show means ± SD for the two subsets of an equal partition of the data (Tables S1 and S2).

surface-tethered syntaxin-1A/Munc18-1 complex. As expected, the MUN domain was required for the transit of syntaxin-1A into the ternary SNARE complex (Ma et al., 2011; Yang et al., 2015). When the MUN domain concentration was increased, more ternary SNARE complex was formed and, in contrast, BSA control did not lead to ternary complex formation (Figures 4B and 4F; Table S1).

Using FRET label pairs, we probed the syntaxin-1A/synaprobrevin-2 subconfiguration (Figures 4C and 4D; Table S2) and the syntaxin-1A/SNAP-25A subconfiguration (Figures 4G and 4H; Table S2) within ternary SNARE complexes that were assembled starting from syntaxin-1A/Munc18-1 with the addition of synaptobrevin-2, SNAP-25A, and MUN domain. The smFRET histograms revealed a majority of high FRET efficiency populations (~95%) for both subconfigurations, demonstrating that the MUN domain and Munc18-1 cooperate to properly assemble ternary SNARE complex by promoting both the proper syntaxin-1A/synaptobrevin-2 and syntaxin-1A/SNAP-25A subconfigurations within the ternary SNARE complex.

Inclusion of Both Munc18-1 and Munc13-1 Leads to Near-Physiological Ca^{2+} Sensitivity in the Fusion Assay

Since Munc18-1 and Munc13-1 cooperate to promote proper assembly of the ternary SNARE complex (Figure 4), we also wanted to perform our fusion assay starting from reconstituted syntaxin-1A/Munc18-1 complex. However, direct reconstitution

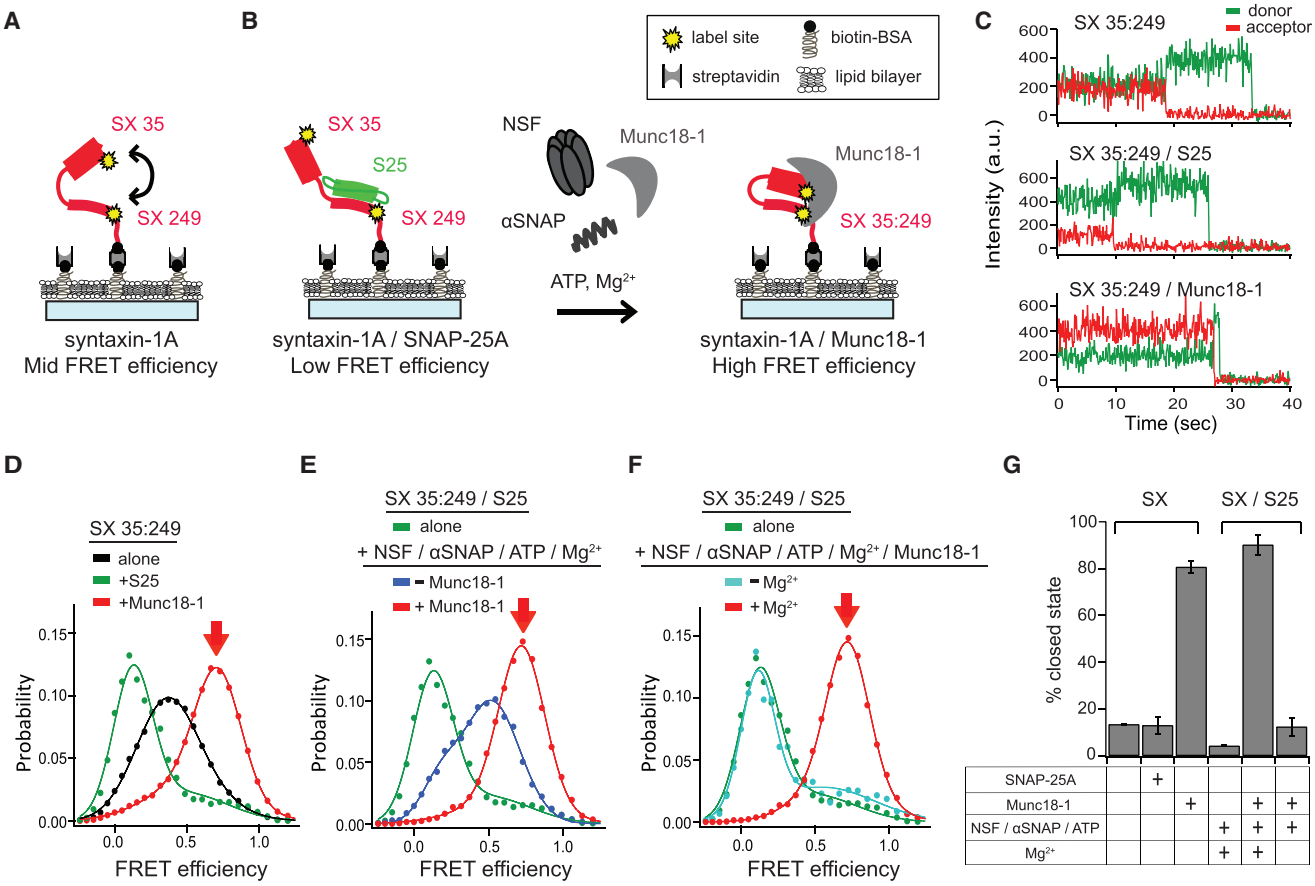

Figure 5. Formation of Syntaxin-1A/Munc18-1 Complex Starting from Syntaxin-1A/SNAP-25A Complex

(A and B) smFRET experiments starting from surface-tethered cytoplasmic domain of syntaxin-1A (SX) alone (A) or SX/SNAP-25A (S25) complex (B). SX/S25 or SX/Munc18-1 complexes were formed by incubating S25 or Munc18-1 to surface-tethered SX, respectively. The yellow stars indicate residues that are used for labeling with fluorescent dyes. To form SX/Munc18-1 complex starting from SX/S25 complex, 1 μM Munc18-1 was added in the presence of the disassembly factors (1 μM NSF, 10 μM αSNAP, 1 mM ATP, and 1 mM Mg^{2+}).

(C) Representative fluorescence intensity time traces for smFRET efficiency measurements on surface-tethered SX (top panel), in complex with S25 (middle panel) or Munc18-1 (bottom panel).

(D) smFRET efficiency histograms of surface-tethered SX (black line) in SX/S25 complex (green line) or SX/Munc18-1 complex (red line).

(E) smFRET efficiency histograms starting from SX/S25 complex (green line) in the presence (red line) and absence (blue line) of 1 μM Munc18-1.

(F) smFRET efficiency histograms starting from SX/S25 complex (green line) in the presence of 1 μM Munc18-1 in the presence (red line) or absence (cyan line) of 1 mM Mg^{2+}.

(G) The bar chart shows means ± SD of the percent closed state for the two subsets of an equal partition of the data (Table S5). In each smFRET histogram, the red arrow indicates the closed state of SX.

of the syntaxin-1A/Munc18-1 complex into liposomes is technically challenging due to poor solubility of the syntaxin-1A/Munc18-1 complex and dissociation of the complex by certain detergents (Rickman and Davletov, 2005). We therefore reconstituted syntaxin-1A/SNAP-25A complex in PM vesicles, followed by addition of the "disassembly factors" (NSF, αSNAP, ATP, and Mg^{2+}) along with Munc18-1, similar to previous bulk fusion experiments (Ma et al., 2013).

We first determined the efficiency of formation of the syntaxin-1A/Munc18-1 complex starting from syntaxin-1A/SNAP-25A complex by adding the disassembly factors in the presence of Munc18-1 using smFRET efficiency experiments (Figure 5; Tables S5 and S6). The surface-tethered cytoplasmic domain of syntaxin-1A was labeled with a pair of dyes, such that high FRET efficiency is expected in the closed state of syntaxin-1A based on the crystal structure of the syntaxin-1A/Munc18-1 complex (Misura et al., 2000) (Figures 5A, 5C, and 5D). Indeed, the syntaxin-1A/Munc18-1 complex exhibits high FRET efficiency, corresponding to the closed conformation of syntaxin-1A (Figure 5C, bottom panel; Figure 5D, red arrow; Figure 5G), whereas the syntaxin-1A/SNAP-25A SNARE complex shows predominantly low FRET efficiency, corresponding to the open conformation of syntaxin-1A (Figure 5C, middle panel; Figure 5D, green line; Figure 5G).

Upon disassembly of the syntaxin-1A/SNAP-25A complex with the disassembly factors (Figure 5B), syntaxin-1A sampled a wide range of conformations similar to isolated syntaxin-1A (black line in Figure 5D versus blue line in Figure 5E). When

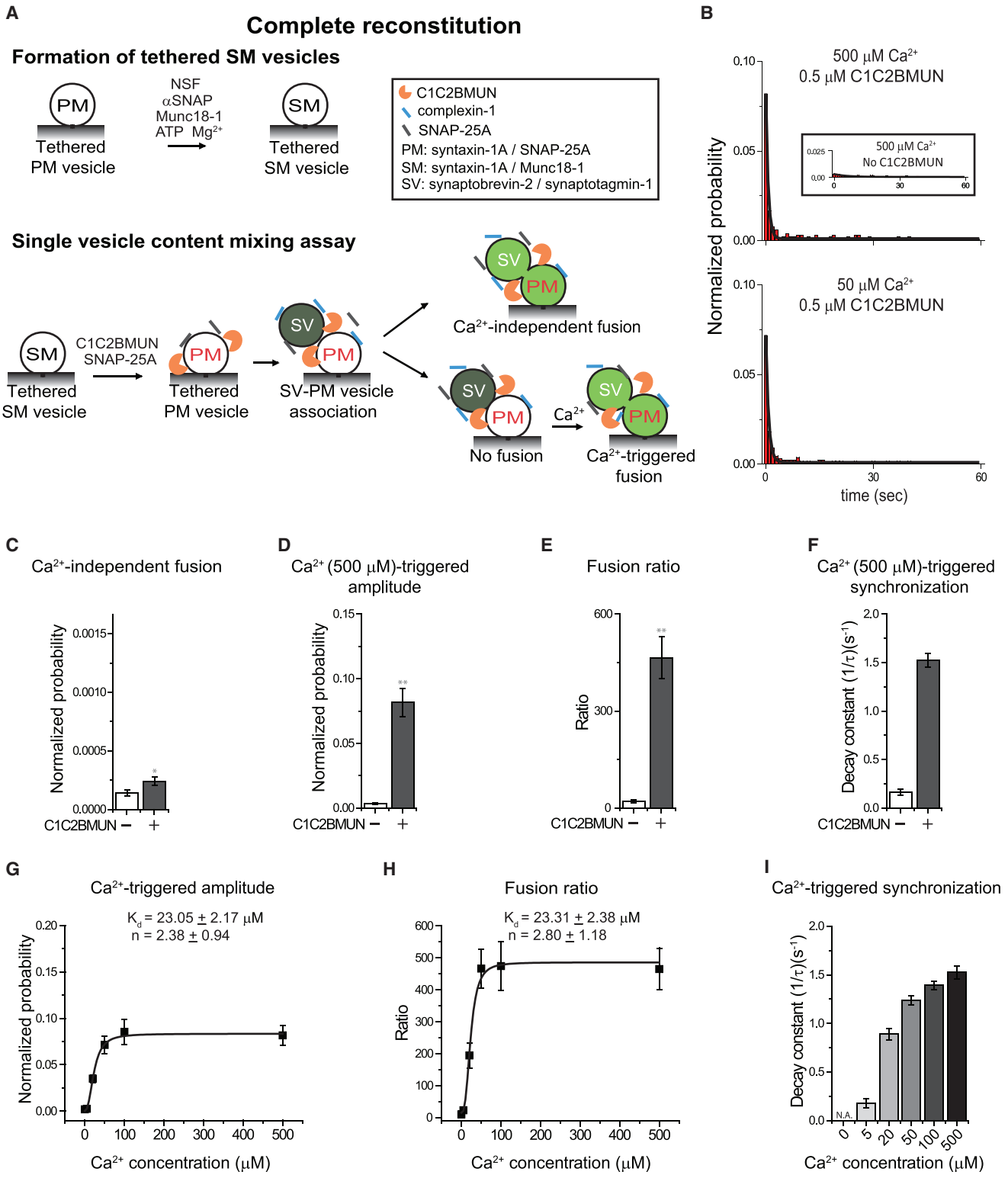

Figure 6. Fusion Experiments with Complete Reconstitution

(A) Single-vesicle content mixing assay with complete reconstitution. PM and SV defined in Figure 2; SM, vesicles with reconstituted syntaxin-1A/Munc18-1 complex. The C1C2BMUN fragment was added after formation of the SM vesicles and during all subsequent stages.

(legend continued on next page)

Munc18-1 was present in addition to the disassembly factors, syntaxin-1A is primarily in the closed conformation (Figure 5E, red line; Figure 5G). In contrast, formation of the syntaxin-1A/Munc18-1 complex did not occur in the absence of Mg^{2+} since lack of Mg^{2+} prevents ATP hydrolysis (Figures 5F and 5G). Taken together, the disassembly factors dissociate syntaxin-1A from the syntaxin-1A/SNAP-25A complex, allowing Munc18-1 to capture it.

We applied this disassembly method for formation of the syntaxin-1A/Munc18-1 complex as the starting point for our fusion assay (Figure 6A) (we refer to this experiment as "complete reconstitution"). Robust Ca^{2+}-triggered fusion histograms were observed in the range of 20–500 μM Ca^{2+} (Figures 6B and S2J; Table S7). When comparing the complete reconstituted fusion assay with the assay starting from PM vesicles, without the intervening steps involving Munc18-1 and the disassembly factors, the Ca^{2+}-independent fusion probability is similar (Figure 3B versus presence of C1C2BMUN in Figure 6C), the 500 μM Ca^{2+}-triggered fusion amplitude and fusion ratio are similar, and the synchronization is slightly improved (0.5 μM C1C2BMUN in Figures 3C–3E versus presence of C1C2BMUN in Figures 6D–6F). In the absence of the C1C2BMUN fragment, no fusion events were observed within experimental error (Figures 6C–6F), since ternary SNARE complex formation cannot occur starting from the syntaxin-1A/Munc18-1 complex without Munc13-1.

A Ca^{2+} titration revealed that the complete reconstituted fusion assay (starting from the syntaxin-1A/Munc18-1 complex) was 3-fold more sensitive than the fusion assay starting from the syntaxin-1A/SNAP-25A complex (Figures 3F–3H versus Figures 6G–6I), with half-maximal Ca^{2+} concentrations of 23.1 ± 2.2 μM for the Ca^{2+}-triggered fusion amplitude and 23.3 ± 2.4 μM for the fusion ratio. In summary, the full reconstitution that includes neuronal SNAREs, synaptotagmin-1, complexin-1, Munc13-1, Munc18-1, NSF, and αSNAP improved the Ca^{2+} sensitivity in the fusion assay by an order of magnitude, and the Ca^{2+} sensitivity is now in the physiological range. Taken together, we have reached a major milestone in reconstituting synaptic vesicle fusion.

We note that in vitro Ca^{2+} sensitivity experiments do not necessarily mimic experiments with varying extracellular Ca^{2+} concentration in neurons. Nevertheless, we note that neurons from ELKS- and RIM-deficient mice exhibit a loss of Munc13 and a lower sensitivity to extracellular Ca^{2+} concentration (Wang et al., 2016). Moreover, manipulations of the Ca^{2+}-binding regions of the C2A and C2B domains of the distant Munc13-4 homolog resulted in lower Ca^{2+} sensitivity of granule exocytosis in mast, neuroendocrine, and platelet cells (Boswell et al., 2012).

Overexpression of the Syntaxin-1A^{LE} Mutant in Munc13-1/2-Deficient Neurons

As previously reported, the syntaxin-1A^{LE} mutant bypasses the need for Munc13 in promoting the transit into the ternary SNARE complex by favoring a largely open conformation of syntaxin-1A^{LE} (Wang et al., 2017). We tested the effect of the LE mutations on the configurations of the SNARE complex (Figure S8). While the syntaxin-1A^{LE} readily allows ternary SNARE complex formation starting from the Munc18-1/syntaxin-1A^{LE} complex upon addition of synaptobrevin-2 and SNAP-25A in the absence of Munc13, it leads to mixtures of both parallel and anti-parallel syntaxin-1A/synaptobrevin-2 and syntaxin-1A/SNAP-25A subconfigurations (Figure S8) in the absence of Munc13. The syntaxin-1A^{LE} mutant therefore in principle allows one to decouple these two molecular functions of Munc13 in vivo since it bypasses one of the functions of Munc13, i.e., the transit of syntaxin into the ternary SNARE complex, but not the proper assembly of the SNARE complex.

We next turned to experiments with autaptic Munc13-1/2 double-deficient neurons that lack any synaptic responses. Overexpression of Munc13-1 or Munc13-2 rescues this phenotype with differential effects on short-term presynaptic plasticity (Rhee et al., 2002; Rosenmund et al., 2002; Varoqueaux et al., 2002). Here we show that overexpression of syntaxin-1A^{LE} in the Munc13-1/2 double-knockout neurons was able to restore some neurotransmission, with approximately 14% of neurons that overexpressed the syntaxin-1A^{LE} mutant exhibiting synaptic release (Figures 7A–7C and 7E). Moreover, the evoked excitatory postsynaptic currents (EPSCs) were significantly decreased in those mutants compared to overexpression using wild-type Munc13-1 (Munc13-1, 4.5 ± 0.36 nA; syntaxin-1A^{LE} mutant, 0.05 ± 0.037 nA) (Figures 7D and 7E). We also observed a concomitant decrease in the size of the RRP, as assessed by the EPSC induced by the exogenous application of a hypertonic sucrose (0.5 M) solution (Munc13-1, 0.30 ± 0.051 nC; syntaxin-1A^{LE} mutant, 0.018 ± 0.0034 nC) (Figures 7D and 7F). We calculated an overall vesicle fusion probability as the ratio of the average EPSC amplitude to the RRP size (Figure 7G) and observed a decrease in vesicle fusion probability from 7.2% ± 0.8% for neurons expressing Munc13-1 to 4.0% ± 1.2% in syntaxin-1A^{LE}-expressing neurons that showed responses.

Next, we examined short-term synaptic plasticity by measuring synaptic responses during low-frequency stimulation (trains of 13 stimuli delivered at 0.2 Hz; Figure 7H) and high-frequency stimulation (50 stimuli delivered at 10 Hz; Figure 7I). In

(B) Representative histograms for triggered fusion at 50 and 500 μM Ca^{2+}. Inset, triggered fusion without C1C2BMUN (note that without C1C2BMUN, ternary SNARE complex cannot form; thus, little fusion is observed).

(C–F) The bar graphs show the effects of C1C2BMUN fragment on the average probability of Ca^{2+}-independent fusion events per second (C), the amplitude of the first 1 s time bin upon 500 μM Ca^{2+} injection (D), the ratio of the Ca^{2+}-triggered amplitude to the average probability of Ca^{2+}-independent fusion per second (E), and the decay rate ($1/\tau$) of the histogram upon Ca^{2+} injection (F). Individual histograms are shown in Figures S2E and S2J.

(G–I) Ca^{2+} concentration dependence of triggered fusion in the presence of 500 nM C1C2BMUN fragment. Shown are the amplitude of the first 1 s time bin upon Ca^{2+} injection (G), the ratio of the Ca^{2+}-triggered amplitude to the average probability of Ca^{2+}-independent fusion per second (H), and the decay rate ($1/\tau$) of the histogram upon Ca^{2+} injection (I) as a function of Ca^{2+} concentration. Hill functions were fit yielding the Ca^{2+} concentration at half occupation K_d and the Hill coefficient n. Individual histograms are in Figure S2J.

(C)–(E), (G), and (H) show means ± SD for multiple independent repeat experiments (Table S7). (F) and (I) show decay constants and error estimates computed from the covariance matrix upon fitting the corresponding histograms with a single exponential decay function using the Levenberg-Marquardt algorithm. *$p < 0.05$, **$p < 0.01$ by Student's t test.

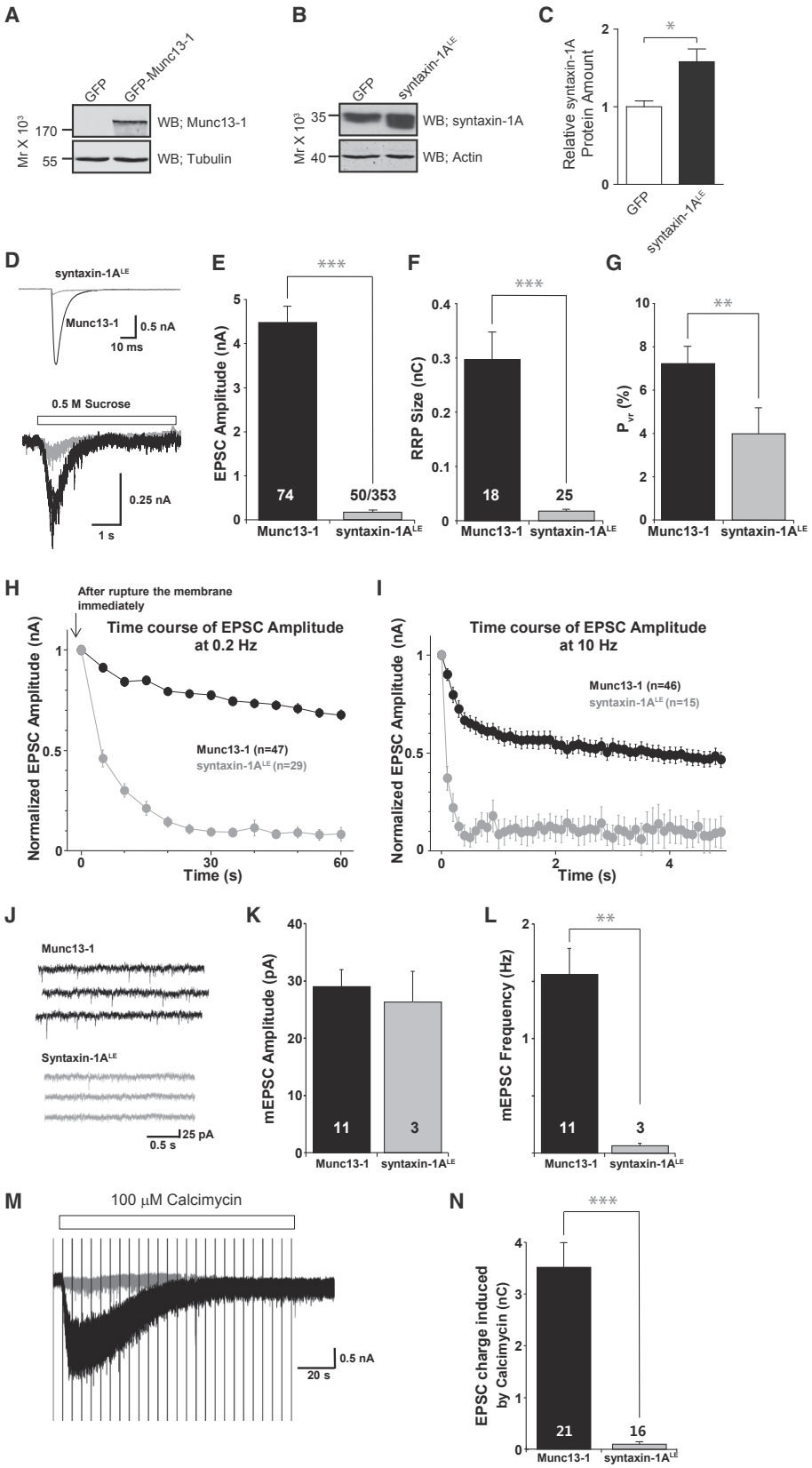

(legend on next page)

both stimulation paradigms, we observed a strong progressive rundown of EPSC amplitudes. In some cases, the evoked EPSCs in the syntaxin-1A^{LE} mutant-expressing neurons that showed responses were not sustained and disappeared entirely during high-frequency 10 Hz stimulation. Regardless of stimulation frequency, within three to four stimulations, vesicle fusion was largely depleted in syntaxin-1A^{LE} mutant neurons, suggesting that a rapid depletion of release sites, or a severe deficit in synaptic vesicle priming or re-priming, is produced by the loss of Munc13-1, or both.

We detected a significant reduction of mEPSC frequency for syntaxin-1A^{LE} mutant overexpression compared to Munc13-1 overexpression (Munc13-1, 1.56 ± 0.23 Hz; syntaxin-1A^{LE} mutant, 0.07 ± 0.002 Hz), but not amplitude (Munc13-1, 29.0 ± 2.96 pA; syntaxin-1A^{LE} mutant, 26.4 ± 5.30 pA) (Figures 7J–7L), suggesting that the postsynaptic sensitivity to quantal release at single synapses was not changed but that the overall release probability was decreased. To confirm that the observed impairments in neurotransmission in syntaxin-1A^{LE} mutant neurons are due to problems relating to presynaptic fusion machinery, and not Ca^{2+} entry or action potential generation, we measured synaptic responses produced by the Ca^{2+} ionophore, calcimycin (Figures 7M and 7N). As expected, treatment with 100 μM calcimycin also revealed a significant deficit in neurotransmission (Munc13-1, 3.52 ± 0.49 nC compared to syntaxin-1A^{LE}, 0.10 ± 0.047 nC). Together with a previous report that showed that the total number of synapses in Munc13-1/2 double-knockout and control neurons was identical (Varoqueaux et al., 2002; Imig et al., 2014), the overall reduction of synaptic neurotransmitter release by syntaxin-1A^{LE} mutant overexpression is likely due to an impairment of the synaptic vesicle machinery.

DISCUSSION

Previous studies of Munc13 and Munc18 actions in situ have demonstrated a critical requirement of these proteins in neuron function. Knockout of either Munc13 or Munc18 results in near total loss of synaptic transmission (Augustin et al., 1999; Richmond et al., 1999; Verhage et al., 2000). However, the lack of detailed structural information of the complex between Munc13, Munc18, and the SNARE complex, in combination with the severity of knockout studies, has hindered a detailed description of the molecular mechanisms of Munc13 or Munc18. Therefore, we turned to an in vitro approach using two techniques: smFRET measurements and an in vitro single-vesicle fusion assay utilizing reconstituted proteins. Together, these techniques uncovered a new coordinated function of Munc13 and Munc18 as critical in not only the mere formation of the SNARE complex, but also in the assembly of a SNARE complex in which all components are in proper relative orientation. Taken together, the consequences of Munc13 knockout go beyond its role in the transfer of syntaxin from Munc18 into the ternary SNARE complex, but also result in the generation of evoked-fusion incompetent, improperly assembled ternary SNARE complexes.

Munc13-1 Has a Molecular Function that Is Independent of Munc18-1

We found that the MUN domain of Munc13-1 promotes the proper parallel subconfiguration between syntaxin-1A and synaptobrevin-2 when assembling the ternary SNARE complex starting from the syntaxin-1A/SNAP-25A complex (Figures 1B–1F), i.e., it prevents improper subconfigurations. Proper formation of the syntaxin-1A/synaptobrevin-2 subconfiguration

Figure 7. Syntaxin-1A^{LE} Mutant Overexpression in Munc13-1/2 Double-Knockout Neurons

Experiments in hippocampal autaptic neurons cultured from Munc13-1/2 double-knockout mice. Neurons were infected with recombinant Semliki Forest virus expressing either wild-type Munc13-1 or syntaxin-1A^{LE} mutant.

(A) Western blot using an anti-Munc13-1 antibody showed the level of expression of Munc13-1 in Munc13-1/2 double-knockout hippocampal neurons infected with Semliki Forest virus expressing GFP only, or Munc13-1 (upper panel). Tubulin was used as a loading control (bottom panel).

(B) Western blot using an anti-syntaxin-1A antibody showed the level of expression of syntaxin-1A/syntaxin-1A^{LE} in Munc13-1/2 double-knockout hippocampal neurons expressing GFP-only syntaxin-1A^{LE} (upper panel). Actin was used as a loading control.

(C) Relative quantification of syntaxin-1A protein amounts in Munc13-1/2 double-knockout hippocampal neurons. Signals were normalized to the level of endogenous syntaxin-1A in GFP-only overexpressing neurons (white bar; 1.0 + 0.1, n = 4). Overexpression of syntaxin-1A^{LE} increased the signal 1.7- ± 0.2-fold (black bar; n = 3, p = 0.037; Student's t test).

(D) EPSCs were recorded in whole-cell patch-clamp mode. Representative traces of EPSCs (top) and postsynaptic currents evoked by 0.5 M sucrose (bottom).

(E) Average values of EPSC amplitudes of the first three stimuli of a 0.2 Hz series of stimuli in neurons expressing Munc13-1 (black; from 74 neurons from 5 mice) and syntaxin-1A^{LE} mutant (gray; from 50 neurons from 5 mice) that showed a response out of 353 that expressed GFP.

(F) Apparent readily releasable vesicle pool (RRP) size calculated by the integral of the sucrose response over 4 s in Munc13-1 (black; from 18 neurons from 3 mice) and syntaxin-1A^{LE} mutant neurons (gray; from 25 neurons from 3 mice).

(G) Release probability calculated as the ratio of the EPSC amplitude to that of the RRP in Munc13-1 (black; from 18 neurons from 3 mice) and syntaxin-1A^{LE} mutant neurons (gray; from 25 neurons from 3 mice).

(H) Normalized EPSC amplitudes in Munc13-1 wild-type (black) and syntaxin-1A^{LE} mutant neurons (gray) during 0.2 Hz stimulation.

(I) Normalized EPSC amplitudes during 10 Hz stimulation.

(J) Representative traces of miniature EPSCs (mEPSCs) in neurons with overexpressed Munc13-1 (top) or syntaxin-1A^{LE} mutant (bottom) in the presence of 200 nM TTX.

(K) Average mEPSC amplitudes of Munc13-1 (black; from 11 neurons from 1 mouse) and syntaxin-1A^{LE} mutant neurons (gray; from 3 neurons from 1 mouse).

(L) Average mEPSC frequencies of Munc13-1 (black) and syntaxin-1A^{LE} mutant neurons (gray).

(M) Example traces of neurons in the presence of 100 μM calcimycin. The vertical lines are stimulation artifacts resulting from intermittent monitoring of evoked EPSCs.

(N) EPSC charge induced by calcimycin in Munc13-1 (from 21 neurons from 3 mice) and syntaxin-1A^{LE} mutant neurons (from 16 neurons from 4 mice). Note *p < 0.05, **p < 0.01, and ***p < 0.001.

(C), (E)–(I), (K), (L), and (N) show mean values ± SEM.

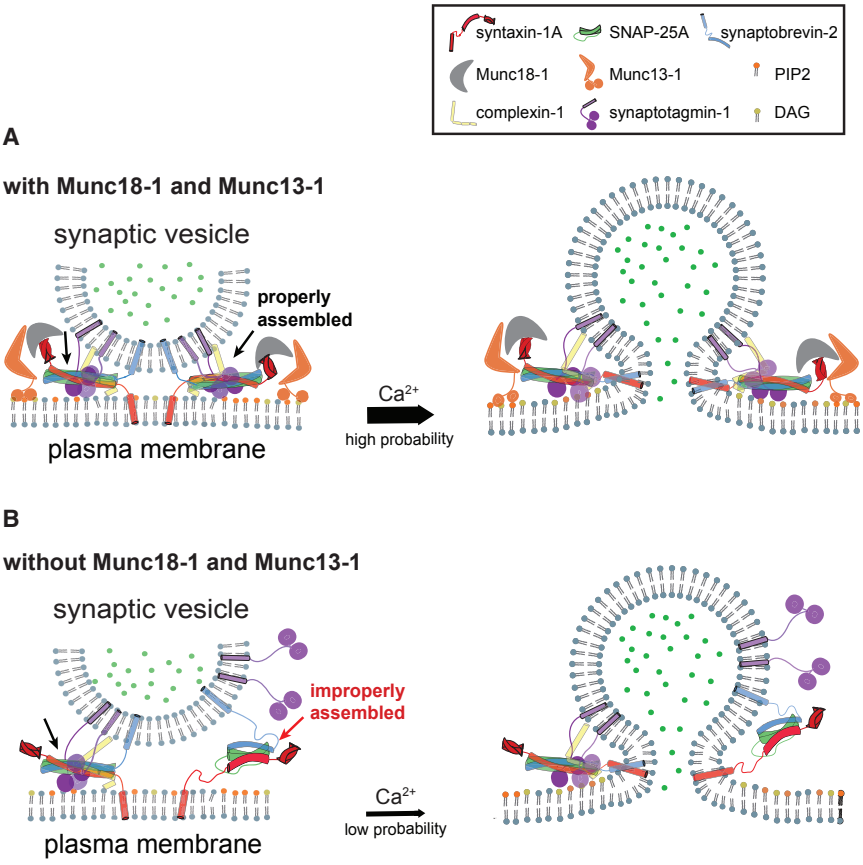

Figure 8. Model of Concerted Munc18-1/Munc13-1 Action to Properly Assemble Ternary SNARE Complex

Model of the combined effect of Munc13-1 and Munc18-1 on Ca^{2+}-triggered fusion.

(A) Munc13-1 and Munc18-1 cooperate to produce proper *trans* ternary SNARE complex.

(B) Without Munc13-1 and Munc18-1, *trans* ternary SNARE complex assembly is error prone, resulting in much reduced Ca^{2+}-triggered fusion probability.

has profound functional consequences: inclusion of the MUN domain in our single-vesicle fusion assay approximately quadrupled the Ca^{2+}-triggered amplitude and the fusion ratio (Figures 2C–2E). This increase in Ca^{2+}-triggered amplitude is due to the ability of the MUN domain to produce the proper syntaxin-1A/synaptobrevin-2 subconfiguration during ternary SNARE complex assembly rather than a direct role in fusion itself since removal of the MUN domain after SV-PM vesicle association but prior to Ca^{2+} triggering produced similar results to keeping the MUN domain present throughout stages (compare protocols "All" and "Pre" in Figure 2; Figure S3). Moreover, addition of the MUN domain only after SV-PM vesicle association had no effect whatsoever on fusion (protocol "Post" in Figure 2).

Inclusion of the longer C1C2BMUN or C1C2BMUNC2C fragments of Munc13-1 in the fusion assay enhanced the Ca^{2+}-triggered amplitude and fusion ratio in a manner similar to the MUN domain (Figures 3C and 3D). However, these longer fragments were able to achieve these effects at 20- and 100-fold lower concentrations than the MUN domain, respectively. This enhanced activity of these fragments is likely due to increased binding to the PM vesicle membrane via its C1 and C2B domains (Figure S6). Inclusion of the C2C domain in the Munc13 fragment (i.e., C1C2BMUNC2C) further lowered the concentration of the Munc13 fragment that was required to maximize the effect on the Ca^{2+}-triggered fusion amplitude by a factor of ~5 (Figure 3C), likely through an increased synaptic vesicle association via the C2C domain (Figure S5). Together the C1, C2B, and C2C domains act by effectively increasing the local concentration of the MUN domain near synaptic fusion sites.

Electron cryo-tomography studies revealed that nearly all associated SV-PM vesicle pairs fused upon Ca^{2+} addition within 1 min (Gipson et al., 2017). Moreover, the lack of C1C2BMUN fragments at a considerable number of contact sites before Ca^{2+} addition is consistent with the notion that Munc13 catalyzed proper SNARE complex assembly and then dissociated from some of the primed prefusion complexes, prior to Ca^{2+} triggering.

Cooperation of Munc13-1 with Munc18-1

In addition to its autonomous function of promoting the proper syntaxin-1A/synaptobrevin-2 subconfiguration, the MUN domain also cooperates with Munc18-1 to promote the proper syntaxin-1A/SNAP-25A subconfiguration within the assembled ternary SNARE complex (Figures 4E–4H). Thus, while the MUN domain alone is sufficient to promote the proper syntaxin-1A/synaptobrevin-2 subconfiguration starting from the syntaxin-1A/SNAP-25A complex (Figures 1D–1F) and consequently increasing the Ca^{2+}-triggered fusion amplitude (Figure 3), the proper syntaxin-1A/SNAP-25A subconfiguration is only achieved when starting from the syntaxin-1A/Munc18-1 complex. Indeed, we observed a substantially improved Ca^{2+} sensitivity when both Munc13-1 and Munc18-1 are included (compare Figures 3F and 6G).

Taken together, Munc13-1 and Munc18-1 are factors for establishing the proper subconfigurations during *trans* ternary SNARE complex assembly (with parallel arrangements of the SNARE components and 1:1:1 stoichiometry) by suppressing improper subconfigurations, i.e., they promote proper ternary SNARE complex assembly (Figure 8). The cooperation of Munc18-1 and Munc13-1 in promoting the proper SNARE complex assembly suggests that Munc18-1 has an indirect, but essential, role in achieving high fusion efficiency, perhaps explaining the severe phenotype of deletion of Munc18-1 in neurons (Verhage et al., 2000).

The existence of factors for proper assembly of ternary SNARE complex may be a general phenomenon since in the context of a different SNARE-mediated fusion process, the so-called HOPS complex, these factors are essential in promoting maximum

efficiency of homotypic vacuolar fusion (Zick and Wickner, 2014). However, while there is a Munc18-1 homolog in the HOPS complex (Vps33) and it has an effect on ternary SNARE complex formation as suggested by structural studies (Baker et al., 2015), there is no Munc13-1 homolog. These findings suggest that evolution of Ca^{2+}-triggered fusion machineries deviated from that of constitutive homotypic membrane fusion. In support of this notion, all Munc13 homologs are thought to be involved in Ca^{2+}-triggered exocytosis (Koch et al., 2000; Lipstein et al., 2012).

Overexpression of the Syntaxin-1A^{LE} Mutant in Munc13-1/2-Deficient Mice

The syntaxin-1A^{LE} mutant promotes ternary SNARE complex formation in the absence of Munc13, but it is unable to promote the proper subconfigurations of the components of the SNARE complex (Figure S8). In further support of the newly discovered molecular function of Munc13, we performed overexpression experiments with either Munc13-1 or the constitutively open mutant of syntaxin (syntaxin-1A^{LE}) in neuronal cultures from Munc13-1/2-deficient mice. The arrest of release in Munc13-1/2 double-knockout mice was only minimally restored when syntaxin-1A^{LE} was expressed (Figure 7).

Molecular Mechanisms of Priming by Munc13-1 and Munc18-1

When some of the SNARE complexes around the contact site between the synaptic and plasma membranes are improperly assembled in the absence of Munc13, they have a large effect on morphologies of the contact sites between SV and PM vesicles (Gipson et al., 2017). Upon inclusion of Munc13, the contacts are largely restricted to point contacts only, i.e., no long contacts are present and very few "dead-end" hemifusion diaphragms were observed prior to Ca^{2+} addition. The ternary SNARE complex interacts with both synaptotagmin-1 and complexin-1, forming a primed and "locked" complex (Zhou et al., 2015, 2017) that is required for maximum probability of Ca^{2+}-triggered release. These interactions will not occur if there are improper subconfigurations within the ternary SNARE complex. In particular, an anti-parallel subconfiguration between syntaxin-1A and synaptobrevin-2 would prevent formation of the SNARE/complexin-1/synaptotagmin-1 tripartite interface (Zhou et al., 2017). Moreover, an anti-parallel subconfiguration between SNAP-25A and syntaxin-1A would prevent formation of the primary interface between synaptogagmin-1 and the ternary SNARE complex since it involves the SNAP-25A and syntaxin-1A components of the SNARE complex (Zhou et al., 2015). This model explains why there is a further substantial increase in Ca^{2+} sensitivity upon inclusion of both Munc13 and Munc18 in vitro (Figures 3 and 6).

Multiple SNARE complexes may be cooperating to achieve maximum speed and efficiency of Ca^{2+}-triggered fusion. If such assemblies included improperly assembled SNARE complexes, they would lose cooperativity and thus fail to maximally evoke fusion upon Ca^{2+} triggering while suppressing Ca^{2+}-independent fusion. This is indeed what we observe: the MUN domain mediated assembly of proper SNARE complex by a factor of 1.6 (Figure 1F), while increasing the Ca^{2+}-triggered amplitude by a factor of 3.6 (Figure 2C), suggesting a cooperative process.

Conclusions

The role of Munc13-1 in short-term plasticity may be related to both molecular functions of Munc13-1 since the amount of properly assembled SNARE complex will depend on the effective concentration of the MUN domain, which may in turn be subject to regulation by the other domains of Munc13-1, including its calmodulin-binding domain. Ca^{2+} binding to the C2B domain; the synergy between C1, C2B, and C2C domains (Liu et al., 2016); and the Ca^{2+}-dependent interaction between calmodulin and Munc13 (Junge et al., 2004) may localize Munc13 to sites of docked synaptic vesicles and increase its ability to assist in proper SNARE complex assembly, as corroborated by the concentration dependence of the various Munc13 fragments in our fusion experiments (Figures 3C–3E). Indeed, mutations of the Munc13-2 C2B domain affect neurotransmitter release upon a single action potential as well as short-term synaptic plasticity (Shin et al., 2010) and mutations in the interface regions between the C1, C2B, and MUN domains have differential effects on evoked release and the RRP (Xu et al., 2017), suggesting that the two molecular functions of Munc13 may be differentially regulated in the neuron. It is of course possible that Munc13 has a more direct role in the fusion process, although our fusion experiments suggest that Munc13 can be removed after proper assembly and prior to Ca^{2+} triggering without a significant effect on Ca^{2+}-triggered fusion. Taken together, regulation of presynaptic plasticity via Munc13 may be in part accomplished by its profound molecular function on ensuring proper assembly of the ternary SNARE complex.

STAR★METHODS

Detailed methods are provided in the online version of this paper and include the following:

- KEY RESOURCES TABLE
- CONTACT FOR REAGENT AND RESOURCE SHARING
- EXPERIMENTAL MODEL AND SUBJECT DETAILS
  - Animals
  - Generation of Munc13-1/2 DKO mice and mouse breeding
- METHODS DETAILS
  - Protein expression and purification
  - Proteins labeling
  - Instrument setup
  - Single molecule experiments
  - Stoichiometry of SNARE complexes in the single molecule experiments
  - Fluorescence anisotropy binding assays
  - PM and SV vesicles
  - Single vesicle-vesicle content mixing assay
  - Data collection and analysis
  - MUN domain removal experiment
  - Neuronal cultures
  - Experiments with Semliki Forest virus
  - Western blotting
  - Electrophysiology
- QUANTIFICATION AND STATISTICAL ANALYSIS

SUPPLEMENTAL INFORMATION

Supplemental Information includes eight figures and seven tables and can be found with this article online at http://dx.doi.org/10.1016/j.neuron.2017.07.004.

AUTHOR CONTRIBUTIONS

Y.L. performed the fusion experiments; U.B.C. the single-molecule fluorescence experiments; and H.J.R., B.A., C.L., and J.R. the neuronal culture experiments. R.A.P., A.L.W., U.B.C., and M.Z. expressed and purified proteins. Y.L., U.B.C., N.B., and J.R. analyzed the data. Y.L., U.B.C., J.R., and A.T.B. designed the experiments. Y.L., U.B.C., R.A.P., A.L.W., J.L., J.R., and A.T.B. wrote the manuscript.

ACKNOWLEDGMENTS

We thank J. Diao, P. Gipson, C. Ma, T.C. Südhof, W.I. Weis, and K.I. White for discussions; L. Almagor for help with fluorescence anisotropy experiments; J. Rizo for providing expression constructs; T. Ha for the smCamera program; Y. Zhang for a fusion analysis program; and the NIH for support (R37-MH63105 to A.T.B.).

Received: September 2, 2016
Revised: May 8, 2017
Accepted: July 6, 2017
Published: August 2, 2017

REFERENCES

Aravamudan, B., Fergestad, T., Davis, W.S., Rodesch, C.K., and Broadie, K. (1999). Drosophila UNC-13 is essential for synaptic transmission. Nat. Neurosci. *2*, 965–971.

Ashery, U., Betz, A., Xu, T., Brose, N., and Rettig, J. (1999). An efficient method for infection of adrenal chromaffin cells using the Semliki Forest virus gene expression system. Eur. J. Cell Biol. *78*, 525–532.

Augustin, I., Rosenmund, C., Südhof, T.C., and Brose, N. (1999). Munc13-1 is essential for fusion competence of glutamatergic synaptic vesicles. Nature *400*, 457–461.

Baker, R.W., Jeffrey, P.D., Zick, M., Phillips, B.P., Wickner, W.T., and Hughson, F.M. (2015). A direct role for the Sec1/Munc18-family protein Vps33 as a template for SNARE assembly. Science *349*, 1111–1114.

Basu, J., Shen, N., Dulubova, I., Lu, J., Guan, R., Guryev, O., Grishin, N.V., Rosenmund, C., and Rizo, J. (2005). A minimal domain responsible for Munc13 activity. Nat. Struct. Mol. Biol. *12*, 1017–1018.

Boswell, K.L., James, D.J., Esquibel, J.M., Bruinsma, S., Shirakawa, R., Horiuchi, H., and Martin, T.F.J. (2012). Munc13-4 reconstitutes calcium-dependent SNARE-mediated membrane fusion. J. Cell Biol. *197*, 301–312.

Breustedt, J., Gundlfinger, A., Varoqueaux, F., Reim, K., Brose, N., and Schmitz, D. (2010). Munc13-2 differentially affects hippocampal synaptic transmission and plasticity. Cereb. Cortex *20*, 1109–1120.

Brunger, A.T. (2005). Structure and function of SNARE and SNARE-interacting proteins. Q. Rev. Biophys. *38*, 1–47.

Brunger, A.T., Cipriano, D.J., and Diao, J. (2015). Towards reconstitution of membrane fusion mediated by SNAREs and other synaptic proteins. Crit. Rev. Biochem. Mol. Biol. *50*, 231–241.

Burgalossi, A., Jung, S., Man, K.N., Nair, R., Jockusch, W.J., Wojcik, S.M., Brose, N., and Rhee, J.-S. (2012). Analysis of neurotransmitter release mechanisms by photolysis of caged Ca^{2+} in an autaptic neuron culture system. Nat. Protoc. *7*, 1351–1365.

Chen, Y.A., Scales, S.J., and Scheller, R.H. (2001). Sequential SNARE assembly underlies priming and triggering of exocytosis. Neuron *30*, 161–170.

Chen, X., Lu, J., Dulubova, I., and Rizo, J. (2008). NMR analysis of the closed conformation of syntaxin-1. J. Biomol. NMR *41*, 43–54.

Choi, U.B., Weninger, K.R., and Bowen, M.E. (2012). Immobilization of proteins for single-molecule fluorescence resonance energy transfer measurements of conformation and dynamics. In Intrinsically Disordered Protein Analysis (Springer New York), pp. 3–20.

Choi, U.B., Zhao, M., Zhang, Y., Lai, Y., and Brunger, A.T. (2016). Complexin induces a conformational change at the membrane-proximal C-terminal end of the SNARE complex. eLife *5*, e16886.

Diao, J., Grob, P., Cipriano, D.J., Kyoung, M., Zhang, Y., Shah, S., Nguyen, A., Padolina, M., Srivastava, A., Vrljic, M., et al. (2012). Synaptic proteins promote calcium-triggered fast transition from point contact to full fusion. eLife *1*, e00109.

Dulubova, I., Sugita, S., Hill, S., Hosaka, M., Fernandez, I., Südhof, T.C., and Rizo, J. (1999). A conformational switch in syntaxin during exocytosis: role of munc18. EMBO J. *18*, 4372–4382.

Fasshauer, D., and Margittai, M. (2004). A transient N-terminal interaction of SNAP-25 and syntaxin nucleates SNARE assembly. J. Biol. Chem. *279*, 7613–7621.

Fernández-Chacón, R., Königstorfer, A., Gerber, S.H.H., García, J., Matos, M.F.F., Stevens, C.F.F., Brose, N., Rizo, J., Rosenmund, C., and Südhof, T.C.C. (2001). Synaptotagmin I functions as a calcium regulator of release probability. Nature *410*, 41–49.

Geppert, M., Goda, Y., Hammer, R.E., Li, C., Rosahl, T.W., Stevens, C.F., and Südhof, T.C. (1994). Synaptotagmin I: a major Ca2+ sensor for transmitter release at a central synapse. Cell *79*, 717–727.

Gipson, P., Fukuda, Y., Danev, R., Lai, Y., Chen, D.-H., Baumeister, W., and Brunger, A.T. (2017). Morphologies of synaptic protein membrane fusion interfaces. Proc. Natl. Acad. Sci. USA. Published online July 24, 2017. http://dx.doi.org/10.1073/pnas.1708492114.

Guan, R., Dai, H., and Rizo, J. (2008). Binding of the Munc13-1 MUN domain to membrane-anchored SNARE complexes. Biochemistry *47*, 1474–1481.

Hammarlund, M., Palfreyman, M.T., Watanabe, S., Olsen, S., and Jorgensen, E.M. (2007). Open syntaxin docks synaptic vesicles. PLoS Biol. *5*, e198.

Heidelberger, R., Heinemann, C., Neher, E., and Matthews, G. (1994). Calcium dependence of the rate of exocytosis in a synaptic terminal. Nature *371*, 513–515.

Imig, C., Min, S.-W., Krinner, S., Arancillo, M., Rosenmund, C., Südhof, T.C., Rhee, J., Brose, N., and Cooper, B.H. (2014). The morphological and molecular nature of synaptic vesicle priming at presynaptic active zones. Neuron *84*, 416–431.

Jockusch, W.J., Speidel, D., Sigler, A., Sørensen, J.B., Varoqueaux, F., Rhee, J.-S., and Brose, N. (2007). CAPS-1 and CAPS-2 are essential synaptic vesicle priming proteins. Cell *131*, 796–808.

Junge, H.J., Rhee, J.S., Jahn, O., Varoqueaux, F., Spiess, J., Waxham, M.N., Rosenmund, C., and Brose, N. (2004). Calmodulin and Munc13 form a Ca2+ sensor/effector complex that controls short-term synaptic plasticity. Cell *118*, 389–401.

Katyal, S.L., Barilaro, L., and Hanin, I. (1985). Lipid composition of different areas of murine brain: effects of lipid extraction procedures. Lipids *20*, 201–203.

Koch, H., Hofmann, K., and Brose, N. (2000). Definition of Munc13-homology-domains and characterization of a novel ubiquitously expressed Munc13 isoform. Biochem. J. *349*, 247–253.

Kyoung, M., Zhang, Y., Diao, J., Chu, S., and Brunger, A.T. (2013). Studying calcium-triggered vesicle fusion in a single vesicle-vesicle content and lipid-mixing system. Nat. Protoc. *8*, 1–16.

Lai, Y., Diao, J., Cipriano, D.J., Zhang, Y., Pfuetzner, R.A., Padolina, M.S., and Brunger, A.T. (2014). Complexin inhibits spontaneous release and synchronizes Ca2+-triggered synaptic vesicle fusion by distinct mechanisms. eLife *3*, e03756.

Lai, Y., Choi, U.B., Zhang, Y., Zhao, M., Pfuetzner, R.A., Wang, A.L., Diao, J., and Brunger, A.T. (2016). N-terminal domain of complexin independently activates calcium-triggered fusion. Proc. Natl. Acad. Sci. USA *113*, E4698–E4707.

Lipstein, N., Schaks, S., Dimova, K., Kalkhof, S., Ihling, C., Kölbel, K., Ashery, U., Rhee, J., Brose, N., Sinz, A., and Jahn, O. (2012). Nonconserved Ca(2+)/calmodulin binding sites in Munc13s differentially control synaptic short-term plasticity. Mol. Cell. Biol. *32*, 4628–4641.

Liu, X., Seven, A.B., Camacho, M., Esser, V., Xu, J., Trimbuch, T., Quade, B., Su, L., Ma, C., Rosenmund, C., and Rizo, J. (2016). Functional synergy between the Munc13 C-terminal C1 and C2 domains. eLife *5*, 1–27.

Ma, C., Li, W., Xu, Y., and Rizo, J. (2011). Munc13 mediates the transition from the closed syntaxin-Munc18 complex to the SNARE complex. Nat. Struct. Mol. Biol. *18*, 542–549.

Ma, C., Su, L., Seven, A.B., Xu, Y., and Rizo, J. (2013). Reconstitution of the vital functions of Munc18 and Munc13 in neurotransmitter release. Science *339*, 421–425.

McCann, J.J., Choi, U.B., Zheng, L., Weninger, K., and Bowen, M.E. (2010). Optimizing methods to recover absolute FRET efficiency from immobilized single molecules. Biophys. J. *99*, 961–970.

McMahon, H.T., Missler, M., Li, C., and Südhof, T.C. (1995). Complexins: cytosolic proteins that regulate SNAP receptor function. Cell *83*, 111–119.

Misura, K.M., Scheller, R.H., and Weis, W.I. (2000). Three-dimensional structure of the neuronal-Sec1-syntaxin 1a complex. Nature *404*, 355–362.

Mohrmann, R., Dhara, M., and Bruns, D. (2015). Complexins: small but capable. Cell. Mol. Life Sci. *72*, 4221–4235.

Pevsner, J., Hsu, S.C., Braun, J.E., Calakos, N., Ting, A.E., Bennett, M.K., and Scheller, R.H. (1994). Specificity and regulation of a synaptic vesicle docking complex. Neuron *13*, 353–361.

Rhee, J.S., Betz, A., Pyott, S., Reim, K., Varoqueaux, F., Augustin, I., Hesse, D., Südhof, T.C., Takahashi, M., Rosenmund, C., and Brose, N. (2002). Beta phorbol ester- and diacylglycerol-induced augmentation of transmitter release is mediated by Munc13s and not by PKCs. Cell *108*, 121–133.

Richmond, J.E., Davis, W.S., and Jorgensen, E.M. (1999). UNC-13 is required for synaptic vesicle fusion in *C. elegans*. Nat. Neurosci. *2*, 959–964.

Richmond, J.E., Weimer, R.M., and Jorgensen, E.M. (2001). An open form of syntaxin bypasses the requirement for UNC-13 in vesicle priming. Nature *412*, 338–341.

Rickman, C., and Davletov, B. (2005). Arachidonic acid allows SNARE complex formation in the presence of Munc18. Chem. Biol. *12*, 545–553.

Rosenmund, C., Sigler, A., Augustin, I., Reim, K., Brose, N., and Rhee, J.-S. (2002). Differential control of vesicle priming and short-term plasticity by Munc13 isoforms. Neuron *33*, 411–424.

Rothman, J.E. (2014). The principle of membrane fusion in the cell (Nobel lecture). Angew. Chem. Int. Ed. Engl. *53*, 12676–12694.

Schneggenburger, R., and Neher, E. (2000). Intracellular calcium dependence of transmitter release rates at a fast central synapse. Nature *406*, 889–893.

Shin, O.-H., Lu, J., Rhee, J.-S., Tomchick, D.R., Pang, Z.P., Wojcik, S.M., Camacho-Perez, M., Brose, N., Machius, M., Rizo, J., et al. (2010). Munc13 C2B domain is an activity-dependent Ca2+ regulator of synaptic exocytosis. Nat. Struct. Mol. Biol. *17*, 280–288.

Stevens, D.R., Wu, Z.X., Matti, U., Junge, H.J., Schirra, C., Becherer, U., Wojcik, S.M., Brose, N., and Rettig, J. (2005). Identification of the minimal protein domain required for priming activity of Munc13-1. Curr. Biol. *15*, 2243–2248.

Südhof, T.C. (2012). The presynaptic active zone. Neuron *75*, 11–25.

Südhof, T.C.C. (2013). Neurotransmitter release: the last millisecond in the life of a synaptic vesicle. Neuron *80*, 675–690.

Sutton, R.B., Fasshauer, D., Jahn, R., and Brunger, A.T. (1998). Crystal structure of a SNARE complex involved in synaptic exocytosis at 2.4 A resolution. Nature *395*, 347–353.

Trimbuch, T., and Rosenmund, C. (2016). Should I stop or should I go? The role of complexin in neurotransmitter release. Nat. Rev. Neurosci. *17*, 118–125.

Varoqueaux, F., Sigler, A., Rhee, J.-S., Brose, N., Enk, C., Reim, K., and Rosenmund, C. (2002). Total arrest of spontaneous and evoked synaptic transmission but normal synaptogenesis in the absence of Munc13-mediated vesicle priming. Proc. Natl. Acad. Sci. USA *99*, 9037–9042.

Verhage, M., Maia, A.S., Plomp, J.J., Brussaard, A.B., Heeroma, J.H., Vermeer, H., Toonen, R.F., Hammer, R.E., van den Berg, T.K., Missler, M., et al. (2000). Synaptic assembly of the brain in the absence of neurotransmitter secretion. Science *287*, 864–869.

Wang, S.S.H., Held, R.G., Wong, M.Y., Liu, C., Karakhanyan, A., and Kaeser, P.S. (2016). Fusion competent synaptic vesicles persist upon active zone disruption and loss of vesicle docking. Neuron *91*, 777–791.

Wang, S., Choi, U.B., Gong, J., Yang, X., Li, Y., Wang, A.L., Yang, X., Brunger, A.T., and Ma, C. (2017). Conformational change of syntaxin linker region induced by Munc13s initiates SNARE complex formation in synaptic exocytosis. EMBO J. *36*, 816–829.

Weber, T., Zemelman, B.V., McNew, J.A., Westermann, B., Gmachl, M., Parlati, F., Söllner, T.H., and Rothman, J.E. (1998). SNAREpins: minimal machinery for membrane fusion. Cell *92*, 759–772.

Weninger, K., Bowen, M.E., Chu, S., and Brunger, A.T. (2003). Single-molecule studies of SNARE complex assembly reveal parallel and antiparallel configurations. Proc. Natl. Acad. Sci. USA *100*, 14800–14805.

Weninger, K., Bowen, M.E., Choi, U.B., Chu, S., and Brunger, A.T. (2008). Accessory proteins stabilize the acceptor complex for synaptobrevin, the 1:1 syntaxin/SNAP-25 complex. Structure *16*, 308–320.

Winter, U., Chen, X., and Fasshauer, D. (2009). A conserved membrane attachment site in alpha-SNAP facilitates N-ethylmaleimide-sensitive factor (NSF)-driven SNARE complex disassembly. J. Biol. Chem. *284*, 31817–31826.

Woodbury, D.J., and Rognlien, K. (2000). The t-SNARE syntaxin is sufficient for spontaneous fusion of synaptic vesicles to planar membranes. Cell Biol. Int. *24*, 809–818.

Xu, J., Pang, Z.P., Shin, O.-H., and Südhof, T.C. (2009). Synaptotagmin-1 functions as a Ca2+ sensor for spontaneous release. Nat. Neurosci. *12*, 759–766.

Xu, J., Camacho, M., Xu, Y., Esser, V., Liu, X., Trimbuch, T., Pan, Y.-Z., Ma, C., Tomchick, D.R., Rosenmund, C., and Rizo, J. (2017). Mechanistic insights into neurotransmitter release and presynaptic plasticity from the crystal structure of Munc13-1 C1C2BMUN. eLife *6*, http://dx.doi.org/10.7554/eLife.22567.

Yang, B., Steegmaier, M., Gonzalez, L.C., Jr., and Scheller, R.H. (2000). nSec1 binds a closed conformation of syntaxin1A. J. Cell Biol. *148*, 247–252.

Yang, X., Wang, S., Sheng, Y., Zhang, M., Zou, W., Wu, L., Kang, L., Rizo, J., Zhang, R., Xu, T., and Ma, C. (2015). Syntaxin opening by the MUN domain underlies the function of Munc13 in synaptic-vesicle priming. Nat. Struct. Mol. Biol. *22*, 547–554.

Zhou, Q., Lai, Y., Bacaj, T., Zhao, M., Lyubimov, A.Y., Uervirojnangkoorn, M., Zeldin, O.B., Brewster, A.S., Sauter, N.K., Cohen, A.E., et al. (2015). Architecture of the synaptotagmin-SNARE machinery for neuronal exocytosis. Nature *525*, 62–67.

Zhou, Q., Zhou, P., Wang, A.L., Wu, D., Zhao, M., Südhof, T.C., and Brunger, A.T. (2017). The primed SNARE-complexin-synaptotagmin complex for neuronal exocytosis. Nature. Published online August 24, 2017. http://dx.doi.org/10.1038/nature23484.

Zick, M., and Wickner, W.T. (2014). A distinct tethering step is vital for vacuole membrane fusion. eLife *3*, e03251.

STAR★METHODS

KEY RESOURCES TABLE

REAGENT or RESOURCE	SOURCE	IDENTIFIER
Antibodies		
Rabbit anti-Actin	Sigma	Cat#A5060; RRID: AB_476738
Mouse anti-Syntaxin-1	SySy	Cat#110 011; RRID: AB_887842
Rabbit anti-Munc13-1	SySy	Cat#126 103; RRID: AB_887733
Mouse anti-Tubulin	Sigma	Cat#T4026; RRID: AB_477577
Goat anti-Rabbit IgG-IRDye800	Rockland	Cat#611-132-122; RRID: AB_220152
Goat anti-Mouse IgG-IRDye700	Rockland	Cat#610-130-121; RRID: AB_220121
Chemicals, Peptides, and Recombinant Proteins		
Alexa 488 C5	Thermo Fisher Scientific	Cat#A10254
Alexa 555 C2	Thermo Fisher Scientific	Cat#A20346
Alexa 647 C2	Thermo Fisher Scientific	Cat#A20347
Alexa 555 NHS Ester	Thermo Fisher Scientific	Cat#A20009
glucose oxidase	Sigma	Cat#G2133
catalase	Sigma	Cat#C100
glucose	Sigma	Cat#D9434
cyclooctatetraene	Sigma	Cat#138924
egg phosphatidylcholine (PC)	Avanti Polar Lipid	Cat#840051
Brain total lipid extract	N/A	Cat#131101C
1-Palmitoyl-2-oleoyl-sn-glycero-3-phosphocholine (POPC)	Avanti Polar Lipid	Cat#850457C
1,2-Dioleoyl-sn-glycerol-3-phosphoethanolamine (DOPE)	Avanti Polar Lipid	Cat#850725C
1,2-dioleoyl-sn-glycero-3-phospho-L-serine (DOPS)	Avanti Polar Lipid	Cat#840035C
Cholesterol	Avanti Polar Lipid	Cat#70000P
L-α-phosphatidylinositol-4,5-bisphosphate (PIP2)	Avanti Polar Lipid	Cat#8400046X
1-2-dioleoyl-sn-glycerol	Avanti Polar Lipid	Cat#800811
1-Oleoyl-2-(12-biotinyl(aminododecanoyl))-sn-glycero-3-phosphoethanolamine (Biotin-PE)	Avanti Polar Lipid	Cat#860562C
sulforhodamine B	Invitrogen	Cat#S1307
mPEG-SVA	Laysan Bio	Cat#mPEG-SVA-5000
Biotin-PEG-SVA-5000	Laysan Bio	Cat#Biotin-PEG-SVA-5000
DMEM medium	GIBCO	Cat#41966-029
Neurobasal A medium	GIBCO	Cat#10888-022
NBQX disodium salt	Tocris Bioscience	Cat#1044
Tetrodotoxin (TTX)	Tocris Bioscience	Cat#1078
(-)-Bicuculline methochloride	Tocris Bioscience	Cat#0131
Calcium Ionophore A23187	HelloBio	Cat#HB1000
Experimental Models: Cell Lines		
Sf9 insect cell	GIBCO	Cat#11496015
E.Coli.DH10 Bac	Thermo Fisher Scientific	Cat#10361012
E.coli. BL21 (DE3)	Invitrogen	Cat#C600003
Experimental Models: Organisms/Strains		
Mouse: M13-DKOs: Unc13atm1Bros; Unc13btm1Rmnd	(Augustin et al., 1999; Varoqueaux et al., 2002)	RRID: MGI2654056

(*Continued on next page*)

Continued

REAGENT or RESOURCE	SOURCE	IDENTIFIER
Recombinant DNA		
pACYC184-BirA	Avidity	Cat#AVB101
Munc13-1-EGFP	(Ashery et al., 1999)	N/A
syntaxin-1ALE-IRES-GFP	(Richmond et al., 2001)	N/A
Software and Algorithms		
OriginPro	Origin lab	http://www.originlab.com/
MATLAB	MathWorks	https://www.mathworks.com/
Igor	WaveMetrics	https://www.wavemetrics.com/products/igorpro/igorpro.htm
smCamera	Taekjip Ha	http://ha.med.jhmi.edu/resources/#1464200861600-0fad9996-bfd4
GraphPad Prism 5	GraphPad Software	http://www.graphpad.com/
AxoGraph Version 1.4.3	John Clements	https://axograph.com/

CONTACT FOR REAGENT AND RESOURCE SHARING

Further information and requests for resources and reagents should be directed to and will be fulfilled by the Lead Contact, Axel T. Brunger (brunger@stanford.edu).

EXPERIMENTAL MODEL AND SUBJECT DETAILS

Animals

Mouse lines, age: DIV10-15, the sex for the cultures were not distinguished.

Generation of Munc13-1/2 DKO mice and mouse breeding

Mouse breeding was done with permission of the Niedersächsisches Landesamt für Verbraucherschutz und Lebensmittelsicherheit (LAVES; 33.19.42502-04-15/1817). All animals were kept according to the European Union Directive 63/2010/EU and ETS 123 in individually ventilated cages (IVCs) under specific pathogen-free conditions at 21 ± 1°C and 55% ± 10% relative humidity. The light/dark cycle was 12 h/12 hr. Mice were group-housed in IVCs type I superlong (435 cm^2 floor area; TECHNIPLAST). The mouse environment consisted of food and tap water ad libitum, bedding, and nesting material. Cages were changed once a week. The animal health status was controlled daily by animal caretakers as well as by a veterinarian. Systematic health monitoring was carried out quarterly according to FELASA recommendations with either NMRI sentinel mice or animals directly taken from the colony. Health monitoring consisted of serological analyses and microbiological, parasitological, and pathological examinations. The mouse colony used for experiments did not exhibit signs of the pathogens routinely tested for. Mice lacking Munc13-1 (Unc13A) and Munc13-2 (Unc13B) (Augustin et al., 1999; Varoqueaux et al., 2002) were initially generated using 129/ola embryonic stem cells. Since the establishment of the initial M13-DKO line, the line has been bred into the C57BL/6N background more than 10 times. As the remaining 129/ola genetic contribution has not been assessed in the M13-DKO colony, the line must be regarded to be on a mixed C57BL/6N;129/ola background, with a minimal 129/ola contribution. M13-DKO and CTR littermates, obtained by interbreeding Unc13A+/−; Unc13B+/− and Unc13A+/−;Unc13B−/− mice, were used for all experiments. CTRs with genotypes Unc13A+/+;Unc13B−/−, Unc13A+/+;Unc13B+/− and Unc13A+/−;Unc13B+/− show no obvious changes in brain morphology or cage behavior, and cultured neurons and hippocampal slices of mice with these genotypes show essentially normal transmitter release (Varoqueaux et al., 2002; Breustedt et al., 2010). The gender of animals used for experimentation was not checked because all previous studies on M13-DKOs had indicated that the gender does not affect the M13 DKO phenotype.

METHODS DETAILS

Protein expression and purification

We used the same constructs and protocols to purify cysteine-free SNAP-25A, synaptotagmin-1, complexin-1 as described in Lai et al. (2014). For syntaxin-1A and synaptobrevin-2 we used the hexa-histidine tagged constructs and protocol described in Lai et al. (2016). The protein sample concentrations were measured by UV absorption at 280 nm, aliquots were flash frozen in liquid nitrogen and stored at −80°C.

Munc18-1a was expressed in BL21(DE3) cells using 0.5mM IPTG for 12-16 hr at 20°C from a pPROExHTa vector (Invitrogen, Carlsbad, CA) as an N-terminal hexa-histidine tag with a tobacco etch virus (TEV) protease cleavage site to remove the tag. Cells from 6 L of

induced culture were re-suspended in 200 mL of buffer A (20 mM sodium phosphate pH 8, 300 mM NaCl, 10 mM imidazole) containing 1 mM PMSF and 4 EDTA free protease inhibitor tablets (Roche, Basel, Switzerland). Cells were lysed by three passes through the Emulsiflex C5 homogenizer (Avestin, Ottawa, Canada) at 15000 psi. Lysate was clarified by centrifugation in the Ti45 rotor (Beckman Coulter, Brea, CA) for 35 min at 40,000 RPM. The supernatant was bound to 5 mL of Nickel NTA beads (QIAGEN, Hilden, Germany) for 30 min with stirring at 4°C. The beads were harvested by centrifugation, poured into a column, attached to the AKTA prime (GE Healthcare, Uppsala, Sweden) and washed with 60 mL of buffer A supplemented with 50mM Imidazole. Munc18a was eluted with buffer A supplemented with 300mM Imidazole. Protein containing fractions were combined, 70ug of TEV protease was added to cleave the tag and the mixture was dialyzed against 1 L of 20 mM Tris pH 8, 50 mM NaCl, 1 mM EDTA, 5 mM DTT (monoQ buffer A) at 4°C overnight. Any precipitate was removed from the dialyzed sample by centrifugation and the supernatant was injected on the monoQ column (GE Healthcare, Uppsala, Sweden) equilibrated in monoQ buffer A. The column was washed with 25 column volumes of monoQ buffer A and then eluted using a linear NaCl gradient from 50 to 500 mM NaCl over 30 column volumes. Protein containing fractions were combined and dialyzed against 1 L of 20 mM HEPES pH 7.5, 180 mM NaCl, 20 μM EGTA, 0.1% 2-mercaptoethanol. The protein concentration was measured by absorption at 280 nm and aliquots were flash frozen in liquid nitrogen and stored at −80°C.

The MUN domain (amino acid range 859-1531, excluding residues 1408-1452) was cloned into a N-terminal hexa-histidine TEV cleavable construct and was expressed in BL21 *E. coli* and grown in 2L of TB. The deletion in this construct prevents aggregation (Ma et al., 2013). The cells were IPTG induced at OD 0.6-0.8 and grown for at least 12 hr at 25°C. The cells were collected by centrifuging the solution in a JA-14 rotor (Beckman Coulter) at 10,000 RPM for 10 min. The cells were resuspended and homogenized in a lysis buffer composed of 20 mM Tris, pH 8.5, 300 mM NaCl, 2 mM DTT, 10% glycerol, 1 mM PMSF, and supplemented with EDTA-free protease inhibitor tablets (Roche Applied Science). The cells were lysed by sonication using a Sonicator ultrasonic processor XL (Misonix Corporation) with the following program: 3 s on, 8 s off, for 10 min at power 8.5. The cell lysate was then centrifuged at 40,000 RPM for 1 hr in a Ti-45 rotor (Beckman Coulter). The supernatant was then applied to 5 mL bed volume of Ni-NTA-agarose column (QIAGEN) for 2 hr stirring at 4°C. The column was washed with the lysis buffer, then the protein was eluted using 50 mM Tris, pH 8.5, 300 mM NaCl, 400 mM imidazole, 0.5 mM DTT, and 10% glycerol. The elution was then collected into a 10,000 molecular mass cut off SnakeSkin Dialysis Tubing (Thermo Scientific), a 50 μL aliquot of TEV at 48 mg/mL was added, and placed in dialysis buffer of consisting of 20 mM Tris, pH 8.5, 50 mM NaCl, 0.5 mM DTT, and 10% glycerol overnight at 4°C. The cleaved protein solution was applied to a MonoQ 4.6/100 ion exchange column (GE Healthcare) equilibrated with 20 mM Tris, pH 8.5, 50 mM NaCl, 1 mM DTT, 10% glycerol (MonoQ buffer A). The protein was eluted with 20 mM Tris, pH 8.5, 1 M NaCl, 1 mM DTT, 10% glycerol using a linear gradient from 50 mM NaCl to 1 M NaCl over 30 column volumes. The appropriate fractions were pooled and applied to a HiLoad Superdex 200 16/60 PG size exclusion column (GE Healthcare) equilibrated in 20 mM Tris, pH 8.5, 150 mM NaCl, 10% glycerol, and 5 mM DTT (Superdex buffer). The protein containing fractions were pooled and concentrated, the protein concentration was measured by UV absorption at 280 nm, and aliquots were flash frozen in liquid Nitrogen and stored at −80°C.

The C1C2BMUN fragment (amino acid range 529-1531, excluding residues 1408-1452) was cloned into a pFastBac HTB vector with an N-terminal hexa-histidine tag and a TEV cleavage site, as described in Ma et al. (2013). Cells from 8L of SF9 cell culture were re-suspended in 300 mL re-suspension buffer (RB) (50 mM Tris, pH 8.0, 250 mM NaCl, 10 mM imidazole, 1 mM TCEP) containing 6 EDTA-free protease inhibitor tablets (Roche Applied Science). The cells were lysed via 3 passes through the Avestin C5 homogenizer at 15000 psi. The lysate was clarified by centrifugation for 1 hr at 40,000 RPM in the Ti45 rotor (Beckman). The supernatant was mixed with 8 mL Ni-NTA beads (QIAGEN) at 4°C stirring for 1 hr. The beads were washed using an AKTA prime system (GE Healthcare) with 50 mL each of RB, RB + 1% Triton X-100, RB + 750 mM NaCl, RB, then eluted with RB + 300 mM imidazole. Peak fractions were pooled and then 200 μL of 11 mg/mL TEV protease, and glycerol to 10% (w/v) was added. The mixture was dialyzed overnight against 1L of 20 mM Tris, pH 8.0, 0.5 mM TCEP, 50 mM NaCl, 10% glycerol. The TEV cleaved protein was injected on a MonoQ 4.6/100 column (GE healthcare) equilibrated in 20 mM Tris, pH 8.0, 50 mM NaCl, 0.5 mM TCEP, 10% glycerol. The column was washed with 20 column volumes of the equilibration buffer and eluted with a NaCl gradient to 500 mM over 30 column volumes. Peak fractions were combined and the protein concentration was measured by UV absorption at 280 nm. Aliquots of 100 μL were flash frozen in liquid nitrogen and stored at −80°C.

The C1C2BMUNC2C fragment (amino acid range 529-1735, excluding residues 1408-1452) was cloned into a pFASTBAC vector with a N-terminal GST tag and a TEV cleavage site, as described in Liu et al. (2016). Cells from 4 L of SF9 cell culture were re-suspended in 300 mL re-suspension buffer (RB) (50 mM Tris, pH 8.0, 250 mM NaCl, 1 mM TCEP, 10% (w/v) glycerol) containing 6 EDTA-free protease inhibitor tablets (Roche Applied Science) and 10 mM imidazole. The cells were lysed via 3 passes through the Avestin C5 homogenizer at 15000 psi. The lysate was clarified by centrifugation for 1 hr at 40,000 RPM in the Ti45 rotor (Beckman). The supernatant was mixed with 10 mL of glutathione Sepharose 4b (GE Healthcare) at 4°C stirring for 2 hr. The beads were washed using an Akta Start system (GE Healthcare) with 80 mL each of RB, RB + 1% Triton X-100, RB + 750 mM NaCl, RB, then eluted with RB + 20mM reduced Glutathione. Peak fractions were pooled and 100 μL of 11 mg/mL TEV protease was added to remove the GST. The protein was concentrated using a 50 kDa Molecular Weight cutoff filter (Millipore) to 5 mL and injected on a superdex 200 16/60 column (GE Healthcare). Peak fractions were combined and the protein concentration was measured by UV absorption at 280 nm. Aliquots of 200 μL were flash frozen in liquid N2 and stored at −80°C.

Chinese hamster NSF with a TEV cleavable N-terminal hexa-histidine tag was expressed from pPROEX-1 in *E.coli*. BL21 (DE3) RIL cells (Agilent Technologies). After lysis and clarification, the lysate was loaded onto a 5 mL Ni-NTA agarose column (QIAGEN), washed with 50 mL of 50 mM Tris, pH 8.0, 300 mM NaCl, 60 mM imidazole, and eluted in the wash buffer supplemented with

350 mM imidazole. Fractions containing NSF were pooled and supplemented with 1 mM EDTA, 1 mM ATP, and 10% glycerol. TEV protease was added to pooled fractions, and the sample was left at 4°C overnight. The protein was then concentrated using an Amicon Ultra-15 centrifugal filter with 100-kDa molecular mass cut off (Millipore) to reduce the volume, and run through a Superdex 200 16/600 size exclusion column (GE Healthcare) that was equilibrated with 50 mM Tris, pH 8.0, 150 mM NaCl, 10% glycerol, 1 mM EDTA, 1 mM ATP, and 1 mM DTT. The protein containing fractions were pooled and concentrated, the protein concentration was measured by UV absorption at 280 nm, and aliquots were flash frozen in liquid nitrogen and stored at −80°C.

Rat αSNAP was expressed with an N-terminal TEV cleavable decahistidine tag from a codon-optimized plasmid using the pJexpress414 backbone (DNA 2.0) in *E.coli*. BL21 (DE3) cells. The clarified lysate was loaded onto a 5 mL Ni-NTA agarose column, washed with 50 mL of 50 mM Tris, pH 8.0, 300 mM NaCl, 60 mM imidazole, and eluted in the wash buffer supplemented with 350 mM imidazole. TEV protease was added to pooled fractions, and the sample was left at 4°C overnight. The protein was then run through a Superdex 200 16/600 size exclusion column that was equilibrated with 50 mM Tris, pH 8.0, 150 mM NaCl, and 0.5 mM TCEP. The protein containing fractions were pooled and concentrated, the protein concentration was measured by UV absorption at 280 nm, and aliquots were flash frozen in liquid nitrogen and stored at −80°C.

For the cytoplasmic domains of syntaxin-1A, synaptobrevin-2, and of SNAP-25A used for single molecule experiments, all constructs were cloned into a pTEV5 vector with an N-terminal TEV cleavable hexa-histidine tag. The cytoplasmic domain of rat syntaxin-1A (amino acid range 1-265) (used in Figures 1, 4, 5, and S8) and the cytoplasmic domain of synaptobrevin-2 (used in Figure S1) were fused to a C-terminal biotinylation sequence (GLNDIFEAQKIEWHE) and co-expressed with the BirA gene engineered in pACYC184 (Avidity) to perform in vivo biotinylation. The construct for the cytoplasmic domain of the syntaxin-$1A^{LE}$ mutant (L165A/E166A) was obtained from the construct of the cytoplasmic domain of syntaxin-1A using the QuickChange Kit (Agilent). Cells were grown to OD600 of about 0.8 at 37°C, and then induced with 0.5 mM IPTG at 30°C in the presence of 0.1 mM biotin for 4 hr. SNAP-25A (amino acid range 1-206) and the cytoplasmic domain of synaptobrevin-2 (amino acid range 1-96) were expressed in *E. coli* (DE3) by growing the cells to an OD600 of about 0.8 at 37°C, then induced with 0.5 mM IPTG at 30°C for 4 hr. All proteins were purified by resuspending the cell pellets from a 1 L of culture in PBS (50 mM NaH2PO4, pH 8.0, 300 mM NaCl, 0.5 mM DTT) buffer supplemented with 0.5 mM PMSF and EDTA-free Complete Protease Inhibitor Cocktail tablets (Roche Applied Science). Cells were lysed by sonication and inclusion bodies were spun down by centrifugation at 20,000 rpm for 30 min in a JA-20 rotor (Beckman Coulter). The supernatant was bound to Nickel-NTA agarose beads (QIAGEN) to remove impurities by washing extensively with PBS containing 20 mM imidazole. Proteins were eluted with PBS containing 400 mM imidazole. 100 μg of TEV was added to cleave off the N-terminal hexa-histidine tags and dialyzed overnight in 20 mM Tris, pH 8.0, 50 mM NaCl, 0.5 mM EDTA, 1 mM DTT. The free TEV protease and the cleaved proteins were separated and concentrated on a 1 mL HiTrap Q column (GE Healthcare) with a linear gradient of 0.05 to 0.6 M NaCl in 20 mM Tris, pH 7.5, 0.5 mM TCEP. The cytoplasmic domain of synaptobrevin-2 (amino acid range 1-96) does not bind to ion exchange columns, so instead we concentrated the sample and purified it using a Superdex 75 size exclusion column (GE Healthcare) in 20 mM Tris, pH 7.5, 150 mM NaCl, 0.5 mM TCEP. The protein purity was checked using SDS-PAGE gel electrophoresis (> 95%). The protein concentration was measured by UV absorption at 280 nm.

Proteins labeling

Protein labeling for the single molecule experiments in Figures 1, 4, 5, S1, S3, and S8, was performed by starting with a cysteine-free template and generating single cysteine mutations using QuickChange Kit (Agilent) at surface exposed positions based on the available crystal structures. Labeling sites used in this work are: syntaxin-1A E35C, syntaxin-1A S193C, syntaxin-1A S249C, SNAP-25A K76C, synaptobrevin-2 A72C, and synaptobrevin-2 A82C. Proteins were labeled with the fluorescent dyes Alexa 488 C_5, Alexa 555 C_2, or Alexa 647 C_2 Maleimide (Thermo Fisher Scientific) in TBS overnight on a rotating platform at 4°C. The MUN domain was labeled at the primary amino group (-NH_2) at the N terminus with the fluorescent dye Alexa 555 NHS Ester (Thermo Fisher Scientific) in 50 mM NaH_2PO_4, pH 6.5, 150 mM NaCl, 0.5 mM TCEP. Labeled proteins were separated from free dye by a column packed with Sephadex G50 resin in 20 mM Tris, pH 7.5, 150 mM NaCl, 0.5 mM TCEP (GE Healthcare).

Instrument setup

All single vesicle fusion and single molecule experiments were performed on a prism-type total internal reflection fluorescence (TIRF) microscope using 532 nm (green) laser (CrystaLaser) excitation. Two observation channels were created by a 640 nm single-edge dichroic beamsplitter (FF640-FDi01-25x36, Shemrock): one channel was used for the fluorescence emission intensity of the content dyes or the Alexa 555 dye and the other channel for that of the Cy5 dye that are part of the injected Ca^{2+}-solution or the Alexa 647 dye. The two channels were recorded on two adjacent rectangular areas (45 × 90 μm^2) of a charge-coupled device (CCD) camera (iXon+ DV 897E, Andor Technology USA, South Windsor CT). The imaging data were recorded with the smCamera program (Taekjip Ha, Johns Hopkins University, Baltimore).

Flow chambers were assembled by creating a "sandwich" consisting of a quartz slide and a glass coverslip that were both coated with polyethylene glycol (PEG) molecules consisting 0.1% (w/v) biotinylated-PEG except when stated otherwise, and using double-sided tape to create up to five flow-chambers.

Single molecule experiments

For the experiments described in Figures 1 and 4, the biotinylated and Alexa 647 labeled cytoplasmic domain of syntaxin-1A was tethered to biotinylated-PEG surface, using 0.1 mg/mL streptavidin and conditions that produced a density of about 1000

syntaxin-1A molecules per 45 × 90 μm^2 field of view, followed by buffer wash with TBS (20 mM Tris, pH 7.5, 150 mM NaCl). To assess the uniformity and consistency of the coverage of surface-tethered syntaxin-1A, we counted spots representing surface-tethered syntaxin-1A molecules in three individual frames of data acquisition movies from each of the chambers, which were used to analyze the density of surface-tethered syntaxin-1A between chamber to chamber on the same microscope slide. We found that the tethered syntaxin-1A surface coverage was consistent and reproducible.

For the incorporation experiments shown in Figures 1C, 1H, 4B, 4F, and S8B, unlabeled syntaxin-1A at the same dilution was used in order to avoid FRET from the donor labels attached to labels attached to syntaxin-1A that were added in solution. Each set of experiments that is shown in the same bar chart (Figures 1C, 1H, 4B, 4F, and S8B) was performed on the same microscope slide but in different chambers. The consistency and reproducibility of the syntaxin-1A surface coverage enables comparison of counts of molecules.

For the experiments described in Figures 1A–1F, we formed the initial syntaxin-1A / SNAP-25A complex by incubating 1 μM SNAP-25A for 5 min to surface-tethered syntaxin-1A, followed by removal of unbound proteins by rinsing with TBS (20 mM Tris, pH 7.5, 150 mM NaCl). Subsequently, the surface-tethered syntaxin-1A / SNAP-25A complex was incubated with 1 nM synaptobrevin-2 that was labeled at residue 82 with FRET donor dye Alexa 555, and the MUN domain at the specified concentration or BSA control for 5 min. Unbound proteins were subsequently washed away by rinsing three times with 200 μL TBS. To measure the degree of incorporation of synaptobrevin-2 into ternary SNARE complexes, we counted the number of spots arising from Alexa 555 dye labeled synaptobrevin-2 molecules. To measure FRET efficiency between labels attached to syntaxin-1A and synaptobrevin-2, syntaxin-1A was labeled with FRET acceptor dye (Alexa 647) at residue 249 prior to surface-tethering.

For the experiments described in Figures 1G–1K, we incubated surfaced-tethered syntaxin-1A with 1 nM SNAP-25A that was labeled with FRET donor dye Alexa 555 at residue 76, 1 μM synaptobrevin-2, and the MUN domain at the specified concentration or BSA control for 5 min. Note that we used a higher concentration of synaptobrevin-2 in these experiments than in the experiments shown in Figures 1A–1F in order to increase the yield of ternary SNARE complex formation. Unbound proteins were subsequently washed away by rinsing three times with 200 μL TBS. Experiments to measure the incorporation of SNAP-25A molecules into ternary complex, and for measuring smFRET efficiency between labels attached to SNAP-25A and syntaxin-1A were performed with the specified labels, using the same procedures as in the experiments described for Figures 1A–1F above.

For the experiments described in Figures 4A–4D, we formed the initial syntaxin-1A / Munc18-1 complex by incubating 1 μM Munc18-1 for 5 min to the surface-tethered syntaxin-1A, followed by removal of unbound proteins by washing with TBS. To form ternary SNARE complex, we incubated the surface-tethered syntaxin-1A / Munc18-1 complex with 10 nM synaptobrevin-2 that was labeled with FRET donor dye (Alexa 555) at residue 82, 1 μM SNAP-25A, and the MUN domain at the specified concentration or BSA control. The concentration of labeled synaptobrevin-2 (10 nM) produced a sufficient amount of ternary SNARE complex. Unbound proteins were subsequently washed away by rinsing three times with 200 μL TBS. Experiments to measure the incorporation of synaptobrevin-2 molecules into ternary complex, and for measuring smFRET efficiency between labels attached to synaptobrevin-2 and syntaxin-1A were performed with the specified labels, using the same procedures as in the experiments described for Figures 1A–1F above.

For the experiments described in Figures 4E–4H, we formed the initial syntaxin-1A / Munc18-1 complex by incubating 1 μM Munc18-1 for 5 min to the surface-tethered syntaxin-1A, followed by removal of unbound proteins by washing with TBS. To form ternary SNARE complex, we incubated the surface-tethered syntaxin-1A / Munc18-1 complex with 1 μM synaptobrevin-2, 10 nM SNAP-25A that was labeled with FRET donor dye (Alexa 555) at residue 76, and the MUN domain at the specified concentration or BSA control. The concentration of labeled SNAP-25A (10 nM) produced a sufficient amount of ternary SNARE complex. Unbound proteins were subsequently washed away by rinsing three times with 200 μL TBS. Experiments to measure the incorporation of SNAP-25A molecules into ternary complex, and for measuring smFRET efficiency between labels attached to SNAP-25A and syntaxin-1A were performed with the specified labels, using the same procedures as in the experiments described for Figures 1G–1K above.

For the experiments described in Figure S8, we formed the initial syntaxin-$1A^{LE}$ / Munc18-1 complex by incubating 1 μM Munc18-1 for 5 min to the surface-tethered syntaxin-$1A^{LE}$, followed by removal of unbound proteins by washing with TBS. To form ternary SNARE complex, we incubated the surface-tethered syntaxin-$1A^{LE}$ / Munc18-1 complex with 1 μM SNAP-25A and 10 nM synaptobrevin-2 that was labeled with FRET donor dye (Alexa 555) at residue 82 (top panel) or with 1 μM synaptobrevin-2 and 10 nM SNAP-25A that was labeled with FRET donor dye (Alexa 555) at residue 76 (bottom panel). Unbound proteins were subsequently washed away by rinsing three times with 200 μL TBS. Experiments to measure the incorporation of SNAP-25A and synaptobrevin-2 molecules into ternary complex, and for measuring smFRET efficiency between labels attached to syntaxin-1A and synaptobrevin-2 or syntaxin-1A and SNAP-25A were performed with the specified labels, using the same procedures as in the experiments described for Figure 1 above.

Since extensive washing with protein-free buffer was performed after ternary SNARE complex assembly, it is unlikely that the MUN domain remains bound to the assembled SNARE complex. Thus, the observed differences in smFRET histograms in Figures 1E, 1J, 4C, and 4G are due to genuine differences between SNARE complexes, and not due to effects caused by affecting the conformational space of the fluorescent dyes that were attached to the specific labeling sites.

For the experiments described in Figure 5, we used 50 nm egg phosphatidylcholine (PC) liposomes (Avanti Polar Lipids) to passivate a surface coated with 1 mg/mL biotinylated BSA in order to create an environment surrounded by lipid bilayers (Choi

et al., 2012). We used this method instead of a PEG-coated surface in order to maximize the efficiency of the disassembly process with NSF / αSNAP since a lipid bilayer increases the activity of αSNAP (Winter et al., 2009). The cytoplasmic domain of syntaxin-1A was stochastically labeled with Alexa 555 and Alexa 647 dyes at residues 35 and 249 and surface-tethered to a biotinylated BSA surface surrounded by a lipid bilayer through biotin-streptavidin linkage using 0.1 mg/mL streptavidin and conditions that produced a density of about 200-300 syntaxin-1A molecules per 45 × 90 μm^2 field of view, followed by buffer wash with TBS (20 mM Tris, pH 7.5, 150 mM NaCl). To determine the conformation of syntaxin-1A / SNAP-25A and syntaxin-1A / Munc18-1 complex, 1 μM of SNAP-25A or Munc18-1 was incubated for 5 min to surface-tethered syntaxin-1A and then washed with TBS to remove free proteins that did not form complex (Figures 5A and 5D). The selected FRET labeling pair of syntaxin-1A residues has an estimated α-carbon-to-α-carbon (Cα-Cα) distance of 2.7 nm based on the crystal structure of the syntaxin-1A / Munc18-1 complex (Misura et al., 2000), and is thus expected to produce high FRET efficiency in the closed state of syntaxin-1A when bound to Munc18-1. To form syntaxin-1A / Munc18-1 complex starting from the syntaxin-1A / SNAP-25A complex, we used the disassembling factors (1 μM NSF, 10 μM αSNAP, 1 mM ATP, 1 mM Mg^{2+}) in presence of 1 μM Munc18-1 (Figures 5B and 5E). We performed bulk steady-state fluorescence anisotropy measurements to confirm that the changes in the smFRET efficiencies are due to conformational changes of syntain-1A, and not due to effects caused by affecting the conformational space of the fluorescent dyes that were attached to the specific labeling sites. The steady-state anisotropy was measured with a Fluorolog spectrofluorometer (HORIBA scientific) relative to free Alexa 555 and 647 using an integration time of 2 s. The intramolecular FRET label sites of syntaxin-1A (residues 35 and 249) were labeled with either Alexa 555 or Alexa 647 dyes. For syntaxin-1A doubly labeled with Alexa 555, we used an excitation wavelength of 532 ± 5 nm and an emission wavelength of 575 ± 5 nm. For sytnaxin-1A doubly labeled with Alexa 647, we used an excitation wavelength of 651 ± 5 nm and an emission wavelength of 671 ± 5 nm. The absorbance value for both dye labeled samples at the respective excitation wavelengths were adjusted to 0.05 AU to perform steady-state anisotropy measurements. The fluorescence anisotropy experiments (Table S6) suggest that the orientations of dyes attached to syntaxin-1A residues 35 or 249 are not affected by the presence of SNAP-25A, Munc18-1, or the disassembly factors (NSF, αSNAP, ATP, $MgCl_2$).

Stoichiometry of SNARE complexes in the single molecule experiments

For the stoichiometry of tethered SNARE complexes in single molecule experiments, as mentioned above, the cytoplasmic domain of syntaxin-1A was tethered to the biotinylated-PEG surface at tens of picomolar concentration. To corroborate the notion that at most one syntaxin-1A molecule is incorporated in each individual complex analyzed in the single molecule experiments shown in Figures 1, 4, 5, and S8 we analyzed all single molecule fluorescence intensity time traces involving acceptor dye (Alexa 647) labeled syntaxin-1A (representative examples are shown in Figures 1D and 1I). The traces that exhibit a stepwise disappearance of the acceptor fluorescence intensity due to photobleaching of the dye molecule show a corresponding anti-correlated rise of the donor fluorescence intensity. This implies that there is exactly one acceptor dye in each analyzed fluorescent spot. We determined the acceptor dye labeling efficiency of the cytoplasmic domain of syntaxin-1A by measuring the absorbance of the labeled protein at 280 nm (corresponding to the protein concentration) and 647 nm (corresponding to the dye concentration) using a Nanodrop-1000 Spectrophotometer (NanoDrop Technologies). The ratio of the two measurements was used to estimate the labeling efficiency, yielding 87%. Thus, all fluorescent spots most likely contain exactly one syntain-1A molecule.

To probe the number of SNAP-25A molecules in the observed single complexes, we incubated surface-tethered (unlabeled) syntaxin-1A with an equimolar mixture of 1 nM Alexa 555 labeled SNAP-25A (residue 76) and Alexa 647 labeled SNAP-25A (residue 76), along with 1 μM cytoplasmic domain of synaptobrevin-2. We observed the fluorescence intensity of the Alexa 555 and Alexa 647 dyes in the field of view, and found that only 1.5% ± 0.7 are co-localized, implying that in all likelihood only one SNAP-25A molecule is involved in an individual complex observed in the single molecule experiments shown in Figures 1, 4, 5, and S8.

For the experiments with labeled synaptobrevin-2 (Figures 1A–1F, 4A–4D, and S8A–S8E), a synaptobrevin-2 molecule is included in each observed complex, by definition. In the experiments with unlabeled synaptobrevin-2 (Figures 1G–1K, 4E–4H, and S8A–S8E), synaptobrevin-2 is applied at 1000 fold excess concentration over SNAP-25A, and thus in all likelihood, all complexes that are observed in these experiments include at least 1 synaptobrevin-2 molecule.

Variable stoichiometries occur when SNAREs are mixed in solution in addition to the 1:1:1 syntaxin-1A / SNAP-25A / synaptobrevin-2 complex, e.g., a 2:1 syntaxin-1A / SNAP-25A complex (Brunger, 2005). However, no complexes have been observed with more than one synaptobrevin-2 molecule. Taking into account that our tethered single molecule setup produces isolated syntaxin-1A molecules and single SNAP-25A in each individual complex, all complexes that are observed in the single molecule experiments shown in Figures 1, 4, and 5 most likely have 1:1:1 stoichiometry.

Fluorescence anisotropy binding assays

For the fluorescence binding experiments described in Figures S1A–S1C, the biotinylated and labeled (fluorescent dye Alexa 647) cytoplasmic domain of synaptobrevin-2 was tethered to a biotinylated-PEG surface, using 0.1 mg/mL streptavidin and conditions that produced a density of about 200 synaptobrevin-2 molecules per 45 × 90 μm^2 field of view. Unbound proteins were subsequently washed away by rinsing three times with 200 μL TBS (20 mM Tris, pH 7.5, 150 mM NaCl). Then, labeled (fluorescent dye Alexa 555) MUN domain was diluted to 100 nM and added in solution with the observation buffer consisting of (1% (w/v) glucose, 20 mM Tris, pH 7.5, 150 mM NaCl) in the presence of oxygen scavenger (20 units/mL glucose oxidase, 1000 units/mL catalase) and triplet-state quencher (100 μM cyclooctatetraene). Imaging data were collected at a frame rate of 10 Hz for 200 s with 635 nm laser light

illumination for 5 s in order to localize surface-tethered and labeled synaptobrevin-2 molecules. Illumination was then switched to 532 nm laser light and continued for 200 s in order to monitor binding events of the labeled MUN domain at the positions of the localized synaptobrevin-2 molecules. A stepwise increase in the fluorescence intensity of the Alexa 555 dye represents a binding event. The gaps between bound states represent unbound periods. Dwell times of the unbound and the bound states were plotted in histograms and fit with single exponential functions to extract the association (k_{on}) and dissociation (k_{off}) rates, respectively.

For the bulk fluorescence anisotropy experiments described in Figures S1D and S1E, synaptobrevin-2 was labeled with fluorescent dye Alexa 488 at residue 72 and the cytoplasmic domain of syntaxin-1A was labeled with fluorescent dye Alexa 488 at residue 193. Anisotropy was measured with a Synergy 2 microplate reader (BioTek) using an excitation wavelength of 485 ± 20 nm and emission wavelength of 528 ± 20 nm at 26.5°C. The fluorescent dye labeled samples were diluted to 10 nM concentration in TBS (20 mM Tris, pH 7.5, 150 mM NaCl, 0.5 mM TCEP) for optimal read out.

PM and SV vesicles

We used the same membrane compositions and protein densities as in our previous studies (Lai et al., 2016) except that 1 mol% DAG as added to the PM vesicles (except when stated otherwise in Figure S6) and no additional cholesterol was supplemented (see below). The reconstitution method for PM and SV vesicles is described in detail in Kyoung et al. (2013) and Lai et al. (2014). SV vesicles contained both reconstituted synaptotagmin-1 and synaptobrevin-2 (except for the vesicle association experiments shown in Figure S5 which only reconstituted synaptobrevin-2), while PM vesicles contained reconstituted syntaxin-1A and SNAP-25A. For SV vesicles the lipid composition was phosphatidylcholine (PC) (48%), phosphatidylethanolamine (PE) (20%), phosphatidylserine (PS) (12%), and cholesterol (20%). For PM vesicles the lipid composition was Brain Total Lipid Extract (Avanti Polar Lipids) supplemented 3.5 mol% PIP2, 1 mol% DAG, and 0.1 mol% biotinylated phosphatidylethanolamine (PE). For PM vesicles without PIP2 and/or DAG (Figure S6), 1 mol% DAG and/or 3.5 mol% PIP2 was replaced by an equal amount of POPC. Note that Brain Total Lipid Extract contains PS. Quantitative ^{31}P NMR analysis by Avanti Polar Lipids of two different stocks of Brain Lipid Extract revealed the following average composition of the major components: PC (17%), PE (8%), plasmalogen PE (14%), PS (8%), and sphingomyelin (5%). Among the remaining 48% of other components of Brain Total Lipid Extract is at least 20% cholesterol (Katyal et al., 1985), so at variance with the previously published protocol (Kyoung et al., 2013) cholesterol was not additionally supplemented to the Brain Total Lipid Extract. Dried lipid films were dissolved in 110 mM OG buffer containing purified proteins at protein-to-lipid ratios of 1:200 for synaptobrevin-2 and syntaxin-1A, and 1:800 for synaptotagmin-1.

A 3-5 fold excess of SNAP-25A (with respect to syntaxin-1A) and 3.5 mol% PIP2 were added to the protein-lipid mixture for PM vesicles only. Detergent-free buffer (20 mM HEPES, pH 7.4, 90 mM NaCl, and 0.1% 2-mercaptoethanol) was added to the protein-lipid mixture until the detergent concentration was at (but not lower than) the critical micelle concentration of 24.4 mM, i.e., vesicle did not yet form. For the preparation of SV vesicles, 50 mM sulforhodamine B (Thermo Fisher Scientific) was added to the protein-lipid mixture. The vesicles subsequently formed during size exclusion chromatography using a Sepharose CL-4B column, packed under near constant pressure by gravity with a peristaltic pump (GE Healthcare) in a 5.5 mL column with a ~5 mL bed volume, that was equilibrated with buffer V (20 mM HEPES, pH 7.4, 90 mM NaCl) supplemented with 20 μM EGTA and 0.1% 2-mercaptoethanol. The eluent was subjected to dialysis into 2 L of detergent-free buffer V supplemented with 20 μM EGTA, 0.1% 2-mercaptoethanol, 5 g of Bio-beads SM2 and 0.8 g/L Chelex 100 resin. After 4 hr, the buffer was exchanged with 2 L of fresh buffer V supplemented with 20 μM EGTA, 0.1% 2-mercaptoethanol and Bio-beads, and the dialysis continued for another 12 hr (overnight). We note that for SV vesicles, the chromatography equilibration and elution buffers did not contain sulforhodamine, so the effective sulforhodamine concentration inside SV vesicles is considerably (up to ten-fold) lower than 50 mM.

As described previously (Kyoung et al., 2013), the presence and purity of reconstituted proteins was confirmed by SDS-PAGE of the vesicle preparations (Figure S6), and the directionality of the membrane proteins (facing outward) was assessed by chymotrypsin digestion followed by SDS-PAGE gel electrophoresis. The size distributions of the SV and PM vesicles were frequently analyzed by electron cryo-microscopy, as described previously (Diao et al., 2012).

Single vesicle-vesicle content mixing assay

To monitor SV-PM vesicle association, Ca^{2+}-independent, and Ca^{2+}-triggered fusion we used the single vesicle content mixing assay described in Lai et al. (2014). The surface of the quartz slides was passivated by coating the surface with polyethylene glycol (PEG) molecules which alleviated non-specific binding of vesicles. The same protocol and quality controls (surface coverage and non-specific binding) were used as described previously (Kyoung et al., 2013) except that PEG-SVA (Laysan Bio) instead of mPEG-SCM (Laysan Bio) was used since it has a longer half-life. The surface was functionalized by inclusion of biotin-PEG (Laysan Bio) during pegylation. A quartz slide was assembled into a flow chamber and incubated with neutravidin for 30 min (0.1 mg/mL).

For the fusion experiments described in Figures 2, 3, S2, S6, and S7 biotinylated PM vesicles (100 × dilution) were pre-incubated with the MUN domain, C1C2BMUN, or C1C2BMUNC2C fragment at the specified concentration for 30 min on ice, and then PM vesicles were tethered to the imaging surface by incubation at room temperature (25°C) for 30 min followed by three rounds of washing with 120 μL buffer V, in order to remove unbound PM vesicles (and the MUN domain in protocol "Pre" in Figure 2); each buffer wash effectively replaces the (3 μL) flow chamber volume more than 100 times. For the fusion experiments described in Figure 2, the MUN domain was only present during the specified stages. When specified, the C1C2BMUN or C1C2BMUNC2C fragment was present in all stages in Figures 3, 6, S6, and S7). We found that the pre-incubation of PM vesicles with C1C2BMUN (refers to protocols "All" and

"Pre" in Figure 2; Figures 3, 6, S6, and S7) was important in order to achieve a largest effect on Ca^{2+}-triggered fusion. There was very little change of the distribution of labeled PM vesicles when they were incubated with the C1C2BMUN fragment (at 0.5 μM) prior to surface-tethering, suggesting that the C1C2BMUN fragment does not cause PM vesicle clustering at that concentration (Figure S4).

For the fusion experiments with complete reconstitution described in Figures 6 and S2, biotinylated PM vesicles (100 × dilution) were tethered to the surface by incubation at room temperature (25°C) for 30 min, followed by three rounds of washing with 120 μL buffer V, in order to remove unbound PM vesicles; each buffer wash effectively replaces the (3 μL) flow chamber volume more than 100 times. To form syntaxin-1A / Munc18-1 complexes on the PM vesicles, 1 μM Munc18, 0.5 μM NSF, 5 μM αSNAP, 3 mM ATP, 3 mM Mg^{2+} were added and incubated with the surface-tethered PM vesicles at room temperature (25°C) for 30 min, followed by three rounds of washing with 120 μL buffer V. Then the C1C2BMUN fragment (at 0.5 μM) and 2 μM SNAP-25A were added and also incubated with the surface-tethered PM vesicles at room temperature (25°C) for 30 min, followed by three rounds of washing with 120 μL buffer V supplemented with 2 μM SNAP-25A and 0.5 μM C1C2BMUN fragment. The C1C2MUN fragment and SNAP-25A were present in all stages (Figure 6A).

Subsequently, for the fusion experiments shown in Figures 2, 3, 6, S2, S6, and S7, we started the illumination and recording of the fluorescence from a particular field of view of the flow chamber, and loaded SV vesicles (diluted 100 to 1000 times, depending on the acquisition stage, see below) into the flow chamber. Association of SV vesicles with PM vesicles was monitored for 1 min. The loaded SV vesicle solution was supplemented with 2 μM complexin-1, along with the MUN domain, C1C2BMUN or C1C2BMUNC2C fragment, and SNAP-25A at the same concentrations as used in the previous stage. While continuing the recording, the flow chamber was washed three times (120 μL of buffer V supplemented with the same concentrations of complexin-1, MUN, C1C2BMUN, or C1C2BMUNC2C fragment, and SNAP-25A as used in the previous stage) in order to remove unbound SV vesicles. Subsequently, we continued recording for 1 min to monitor Ca^{2+}-independent fusion events. Thus, in contrast to a previous version of this assay where SV vesicles where incubated with surface-tethered PM vesicles for at least 30 min (Kyoung et al., 2013), monitoring of fusion events was started right after the 1 min SV-PM vesicle association period and buffer washes. Subsequently, Ca^{2+}-solution was injected into the flow chamber consisting of 500 μM Ca^{2+}, 500 nM Cy5 dye molecules (used as an indicator for the arrival of Ca^{2+} in the evanescent field) in buffer V supplemented with the same concentrations of complexin-1, MUN domain, C1C2BMUN, or C1C2BMUNC2C fragment, and SNAP-25A as used in the previous stage. Ca^{2+}-triggered fusion events were monitored within the same field of view upon injection for a 1 min period. The injection was performed at a speed of 66 μL/s by a motorized syringe pump (Harvard Apparatus, Holliston, USA) using a withdrawal method similar to the one described previously (Lai et al., 2014). All experiments were carried out at ambient temperature (25°C). Our procedure resulted in a time series of images over a total of three minutes, consisting of the subsequent 1 min periods of vesicle association, Ca^{2+}-independent, and Ca^{2+}-triggered fusion, plus 5 s intervals for buffer exchanges. The arrival time of Ca^{2+} was determined by monitoring of the Cy5 channel.

For the vesicle association experiments in shown in Figure S5, content-dye labeled, synaptobrevin-2 reconstituted vesicles (diluted 1000 times) were incubated with surface tethered PM-vesicles along with the MUN domain, C1C2BMUN or C1C2BMUNC2C fragment, and labeled vesicles were counted after a 1 min incubation period.

Data collection and analysis

For the single molecule experiments in Figures 1, 4, 5, S1, and S8 we used an observation buffer consisting of (1% (w/v) glucose, 20 mM Tris, pH 7.5, 150 mM NaCl) in the presence of oxygen scavenger (20 units/mL glucose oxidase, 1000 units/mL catalase) and triplet-state quencher (100 μM cyclooctatetraene). Imaging data were collected at a frame rate of 10 Hz for 100 s until most of the dyes photobleached, with 532 nm laser illumination, using the smCamera program and scripts written for MATLAB (MathWorks). For the smFRET experiments shown in Figures 1, 4, 5, and S8, fluorescence intensity histograms were generated (representative examples are shown in Figures 1D, 1I, and 5C) converted to FRET efficiency by

$$E = \frac{I_A - \beta(I_D - \alpha I_A)}{(I_A - \beta(I_D - \alpha I_A) + (I_D - \alpha I_A))},$$

where αI_A corrects for leakage of acceptor emission into donor channel and βI_D corrects for leakage of donor emission into acceptor channel (McCann et al., 2010). The leakages for our instrument were 16.5% for acceptor fluorescence emission leaking into the donor channel, and 1.7% for donor fluorescence emission leaking into the acceptor channel.

For the experiments described in Figures 1 and 4, the populations of properly assembled subconfigurations (Figures 1F, 1K, 4D, and 4H) were calculated as the area under the Gaussian function fit to the high FRET efficiency population divided by the sum of the total efficiency population in the corresponding smFRET histograms in panels E and J, respectively.

For the experiments described in Figure 5, we fit three Gaussian functions to the smFRET histogram of the syntaxin-1A / SNAP-25A complex (green line in Figure 5D) and three Gaussian functions to the smFRET histogram of the syntaxin-1A / Munc18-1 complex (red line in Figure 5D), respectively. The peak position (FRET efficiency = 0.13) of the Gaussian function that fit the low FRET efficiency population in the histogram of the syntaxin-1A / SNAP-25A complex (green line in Figure 5D) was used to define the FRET efficiency of the open state of syntaxin-1A. The peak position (FRET efficiency = 0.71) of the Gaussian function that fit the high FRET efficiency population in the histogram of the syntaxin-1A / Munc18-1 complex (red line in Figure 5D) was used to define the FRET efficiency of the closed state of syntaxin-1A. The FRET efficiencies of the open and closed states were then used as constraints for fitting three Gaussian functions to the FRET efficiency histograms shown in Figure 5. The quantity "% closed state" was calculated as the area

under the Gaussian function fit to the population of the closed state divided by the total area under the fitted three Gaussian functions (Figure 5G; Table S5).

For the fusion experiments described in Figures 2, 3, 6, S2, S6, and S7, in order to increase the throughput of the assay and make better use of the vesicle samples, after intensive washing (3 × 120 μL) with buffer V (supplemented with 20 μM EGTA to remove Ca^{2+} from the sample chamber), we repeated the entire acquisition sequence (SV vesicle loading, counting the number of freshly associated SV-PM vesicles, monitoring of Ca^{2+}-independent fusion, Ca^{2+}-injection, and monitoring of Ca^{2+}-triggered fusion) in a different imaging area within the same flow chamber. Five such acquisition rounds were performed with the same sample chamber. SV vesicles were diluted 1000 × for the first and second acquisition rounds, 200 × for the third and fourth acquisition rounds, and 100 × for the fifth acquisition round in order to offset the slightly increasing saturation of the surface with SV vesicles. The entire experiment (each with five acquisition rounds) was then repeated *n* times (Tables S3, S4, and S7) (referred to as repeat experiment). Among the specified number of repeats there are at least three different protein preparations and vesicle reconstitutions, so the variations observed in the bar charts reflect sample variations as well as variations among different flow chambers.

We detected content dye fluorescent spots in a particular imaging area with the smCamera program. The appearance of a content dye fluorescence spot corresponds to an association of a SV vesicle to a surface-tethered PM vesicle. However, only those spots were subsequently analyzed and counted that showed *exactly one* stepwise increase of the fluorescence intensity during the SV-PM vesicle association period of 1 min that precedes the subsequent fusion periods (Figures 2A, 3A, and 6A). Thus, this procedure excludes SV vesicles that underwent Ca^{2+}-independent fusion during the vesicle association period since fusion leads to a second stepwise fluorescence intensity increase. Moreover, for data acquisition rounds within the same sample chamber, this procedure excludes SV vesicles that were already associated during a previous acquisition round. Stepwise increases in the fluorescence intensity time traces were automatically detected by the computer program described in Kyoung et al. (2013) and manually checked to ensure correct performance of the automated procedure. Collectively, we refer this selected set of content dye fluorescent spots as the analyzed SV-PM vesicle pairs.

In the subsequent Ca^{2+}-independent and Ca^{2+}-triggered fusion periods of 1 min each, a second stepwise increase in content dye fluorescence intensity was counted as a Ca^{2+}-independent and Ca^{2+}-triggered fusion event, respectively. Histograms for Ca^{2+}-independent and Ca^{2+}-triggered fusion events were generated with a time bin of 1 s. Ca^{2+}-triggered fusion histograms were synchronized by the appearance of fluorescence intensity of the Cy5 dye molecules that are part of the injected Ca^{2+}-solution. Histograms were cumulated over all acquisition rounds and repeat experiments. The cumulated histograms were subsequently *normalized* by dividing the histograms by the total number of analyzed SV-PM vesicle pairs for a particular condition (i.e., the sum of the number of analyzed SV-PM vesicle pairs for all acquisition rounds and repeat experiments for a particular condition) (Tables S3, S4, and S7; Figure S2). As a consequence of the normalization of the histograms, the fusion probabilities and amplitudes are normalized with respect to the corresponding number of analyzed SV-PM vesicle pairs. Thus, the normalized fusion probabilities and amplitudes provide information about fusion of associated SV-PM vesicles, independent of the number of associated vesicle pairs. This is a major advantage of our single vesicle method over bulk fusion assays which cannot distinguish between effects that are due to vesicle association or fusion itself (Brunger et al., 2015).

In the bar charts in Figures 2, 3, 6, S6, and S7, the probability of Ca^{2+}-independent fusion per second is calculated by dividing the overall Ca^{2+}-independent fusion probability of the cumulated and normalized histogram during the 1 min observation period by 60. The "Ca^{2+}-triggered amplitude" is the probability of Ca^{2+}-triggered fusion in the cumulated and normalized histogram during the first time bin (1 s) upon Ca^{2+}-injection. The "fusion ratio" is the ratio of the Ca^{2+}-triggered amplitude and the average probability of Ca^{2+}-independent fusion per second. The error bars for the probabilities and amplitudes were calculated as standard deviations for the *n* repeat experiments (Tables S3, S4, and S7) by using individually-cumulated (but globally normalized) histograms for all rounds of a particular repeat experiment. The histograms of the Ca^{2+}-triggered fusion probability (Figure S2) were fit to a single exponential decay function using the Levenberg-Marquardt algorithm. The degree of synchronization was described by the decay rate and error bars for the decay rate were obtained from the covariance matrix of the fit.

MUN domain removal experiment

For the experiments shown in Figure S3, we used the protocol "Pre" shown in Figure 2A, except that 500 nM of labeled MUN domain was mixed with 9.5 μM unlabeled MUN domain. Labeling of the MUN domain was performed with the Alexa 647 fluorescent dye by covalently linking it to the primary amino group. The percentage of MUN domain molecules that are bound to SV vesicles was calculated by co-localizing the spots in "red" channel that detects the fluorescence intensity of Alexa 647 labeled MUN domain molecules and the spots in the "green" channel that detects the fluorescence intensity of content dye labeled SV vesicles. The co-localization was measured before and after MUN domain molecules were washed away by rinsing with buffer V.

Neuronal cultures

For the experiments described in Figure 7, micro-island cultures of hippocampal neurons were prepared and cultured as previously reported (Jockusch et al., 2007; Burgalossi et al., 2012). Briefly, astrocytes for autaptic cultures were obtained from mouse cortices dissected from P0 wild-type animals and enzymatically digested for 15 min at 37°C with 0.25% (w/v) trypsin-EDTA (GIBCO). Astrocytes were plated in T75 culture flasks in DMEM medium (GIBCO) containing 10% FBS and penicillin (100 U/mL)/streptomycin (100 μg/mL), and grown for 7-10 days in vitro (DIV). After this, astrocytes were trypsinized and plated at a density of ~30,000

cells/well onto 32 mm-diameter glass coverslips that were previously coated with agarose (Sigma-Aldrich), and stamped using a custom-made stamp to generate 200 μm × 200 μm substrate islands with a coating solution containing poly-D-lysine (Sigma-Aldrich), acetic acid, and collagen (BD Biosciences). Hippocampi from Munc13-1/2 double-knockout embryo 18 (E18) mice were isolated and digested for 55 min at 37°C in DMEM medium containing 2.5 U/mL papain (Worthington Biomedical Corporation), 0.2 mg/mL cysteine (Sigma), 1 mM $CaCl_2$, and 0.5 mM EDTA. After washing, the dissociated neurons were seeded onto the micro-island plates in pre-warmed Neurobasal medium (GIBCO) supplemented with B27 (GIBCO), Glutamax (GIBCO) and penicillin (100 U/mL)/streptomycin (100 μg/mL) at a density of ~4,000 cell/well. Neurons were allowed to mature for 10-28 days before they were used for experiments, and only islands containing single neurons were examined.

Experiments with Semliki Forest virus

For the experiments described in Figure 7, generation of Semiliki Forest virus constructs with Munc13-1-EGFP, or syntaxin-$1A^{LE}$-IRES-GFP, generation of virus stocks and neuron infection were performed as previously described (Ashery et al., 1999). To activate the frozen viruses (450 μL) including either Munc13-1 or syntaxin-$1A^{LE}$ genes, 450 mL neuronal medium from the neuronal culture was added. 100 μL chymotrypsin (2 mg/mL, Boehringer Mannheim) was added and incubated for 50-55 min at room temperature. In order to inactivate the activity of chymotrypsin, the virus was incubated with 110 μL aprotinin (6 mg/mL, Boehringer Mannheim) for 15 min. Infection of neurons was performed by adding 30 μL of the activated viruses into autaptic Munc13-1/2 double-knockout neuronal cultures, which were placed in the incubator for 12 hr.

Western blotting

For the experiments described in Figure 7, hippocampal neurons prepared from Munc13-1/2 double-knockout embryo 18 (E18) mice were infected with activated Semliki Forest virus expressing GFP, Munc13-1 or syntaxin-$1A^{LE}$. The lysates were harvested after 12 hr for Munc13-1 or 18 hr for syntaxin-$1A^{LE}$ expressing neurons and analyzed by western blotting using anti-Munc13-1 rabbit antibody (SySy, Cat#126 103) or anti-syntaxin-1 mouse antibody (SySy, Cat#110 011). Mouse anti-tubulin (Sigma, Cat#T4026) or rabbit anti-actin (Sigma-A5060) antibody were used as loading controls for Munc13-1 and syntaxin-1A, respectively. For quantitation, goat anti-rabbit IgG-IRDye800 (Rockland, Cat#611-132-122) and goat anti-mouse IgG-IRDye700 (Rockland, Cat#610-130-121) secondary antibodies were used, and imaged on an Odyssey Infrared Imaging System (LI-COR Biosciences). For quantification of syntaxin-$1A^{LE}$ overexpression, the fluorescence signal from the syntaxin-1 band was normalized by the signal from the actin band. For quantification of Munc13-1 overexpression, the fluorescence signal from the Munc13-1 band was normalized by the signal from the tubulin band. Relative syntaxin-1 protein amounts were calculated by normalization to GFP expressing neurons.

Electrophysiology

For electrophysiology experiments described in Figure 7, autaptic cultured neurons (12-14 DIV) were whole-cell voltage-clamped at −70 mV with an Axopatch 700B (Molecular Devices). All traces were analyzed using AxoGraph X (AxoGraph Scientific). Series resistance was within 10 MΩ and was electronically compensated at least 30%–70%. The experiments were performed using a patch-pipette solution containing 136 mM KCl, 17.8 mM, 1 mM EGTA, 0.6 mM, 4 mM NaATP, 0.3 mM Na_2GTP, 15 creatine phosphate, and 5 U/mL phosphocreatine kinase (315-320 mOsmol/L, pH 7.4). The extracellular solution used for all recordings contained 140 mM NaCl, 2.4 mM KCl, 10 mM HEPES, 10 mM glucose, 4 mM $CaCl_2$ and 4 mM $MgCl_2$ (320 mOsml/L), pH, 7.3. Evoked EPSCs were induced by depolarizing the cell from −70 to 0 mV at a frequency of 0.2 Hz. Only a subset of the Munc13 KDO neurons that were infected with the syntaxin-$1A^{LE}$ construct exhibited action-driven potentials, and even fewer exhibited spontaneous release within a 100 s time period. Only those that showed responses were included in the analyses shown in Figures 7D–7N. The size of the ready releasable pool (RRP) was measured after 6 s application of 0.5 M hypertonic sucrose solution. Short-term plasticity was evaluated by recording EPSCs during 10 Hz stimulation trains. All electrophysiological traces were analyzed using Axograph X software (version 1.4.3, AxoGraph Scientific).

QUANTIFICATION AND STATISTICAL ANALYSIS

Origin, MATLAB, and Igor was used for the generation of all curves and graphs. The fusion experiments described in Figures 2, 3, 6, S2, S6, and S7 were conducted at least three times with different protein preparations and vesicle reconstitutions and properties were calculated as mean ± SD, for *n* experimental repeats (specified in Tables S3–S6 and S9) and the statistical significance was assessed using Student's t test with respect to the specified reference experiment. For the smFRET efficiency properties shown in Figures 1F, 1K, 4D, 4H, 5G, and S8E mean values ± SD were calculated for n = 2 subsets of an equal partition of the data. For the single molecule incorporation data in Figures 1C, 1H, 4B, 4F, and S8B mean values ± SD were calculated from n = 3 independent fields of view. All results in Figure 7 are shown as mean values ± SEM, using the specified number of neurons and mice as specified in the figure and figure legend. Statistical significance was assessed using one-way ANOVA followed by post hoc Bonferroni test or by two-tailed Student's t test, where appropriate. For all the statistical test, the significance is defined as: $^*p < 0.05$ $^{**}p < 0.01$ and $^{***}p < 0.001$. No method was used to determine if the data meet assumptions of the statistical approach.

Neuron, Volume *95*

Supplemental Information

Molecular Mechanisms of Synaptic Vesicle Priming by Munc13 and Munc18

Ying Lai, Ucheor B. Choi, Jeremy Leitz, Hong Jun Rhee, Choongku Lee, Bekir Altas, Minglei Zhao, Richard A. Pfuetzner, Austin L. Wang, Nils Brose, JeongSeop Rhee, and Axel T. Brunger

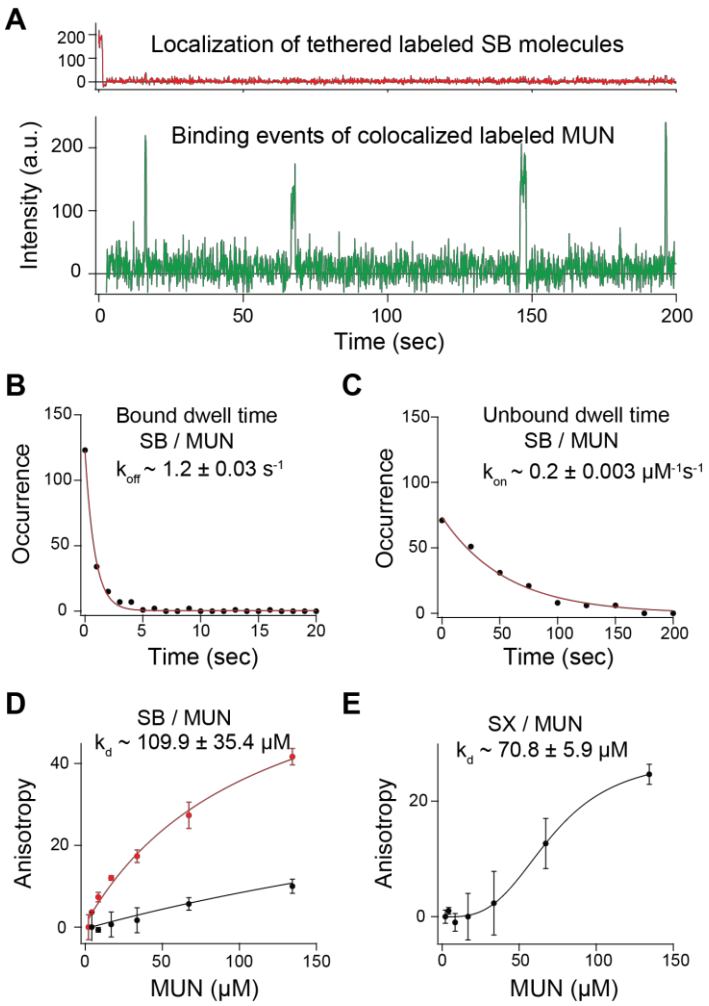

Figure S1. The MUN domain interacts with synaptobrevin-2. Related to Figure 1**.** Single molecule and bulk fluorescence anisotropy binding experiments. (A) Representative single molecule fluorescence intensity time traces showing individual binding events between the surface-tethered cytoplasmic domain of synaptobrevin-2 (SB) and the MUN domain. The fluorescence intensity of fluorescent dye (Alexa 647) labeled SB is colored in red (top trace) and the fluorescence intensity of fluorescent dye (Alexa 555) labeled MUN domain is colored in green (bottom trace). (B-C) Dissociation rate (k_{off}) (B) and association rate (k_{on}) (C) measured by single molecule fluorescence experiments of interactions between the MUN domain and surface-tethered SB molecules. Histograms of the bound and unbound dwell times were fit with single exponentials to extract the dissociation (k_{off}) and association (k_{on}) rate constants, respectively. (D) Bulk fluorescence anisotropy measurements of interactions between SB that was labeled with Alexa 488 at residue 72 and unlabeled MUN domain (red dot in D). As control, a competition experiment was performed in the presence of unlabeled SB at 50 μM (black dot in D). Data points are the mean values of three independent experiments normalized by the first data point, with error bounds defined as standard deviations. Hill equations were fit to estimate the dissociation constant K_d, where the Hill coefficients were constraint to one. (E) Bulk fluorescence anisotropy measurements of interactions between the cytoplasmic domain of syntaxin-1A (SX) that was labeled at residue 193 with Alexa 488 and unlabeled MUN domain. Data points are the mean values of three independent experiments normalized by the first data point, with error bounds defined as standard deviations. The data were fit with a Hill equations in order to obtain an estimate of the dissociation constant K_d.

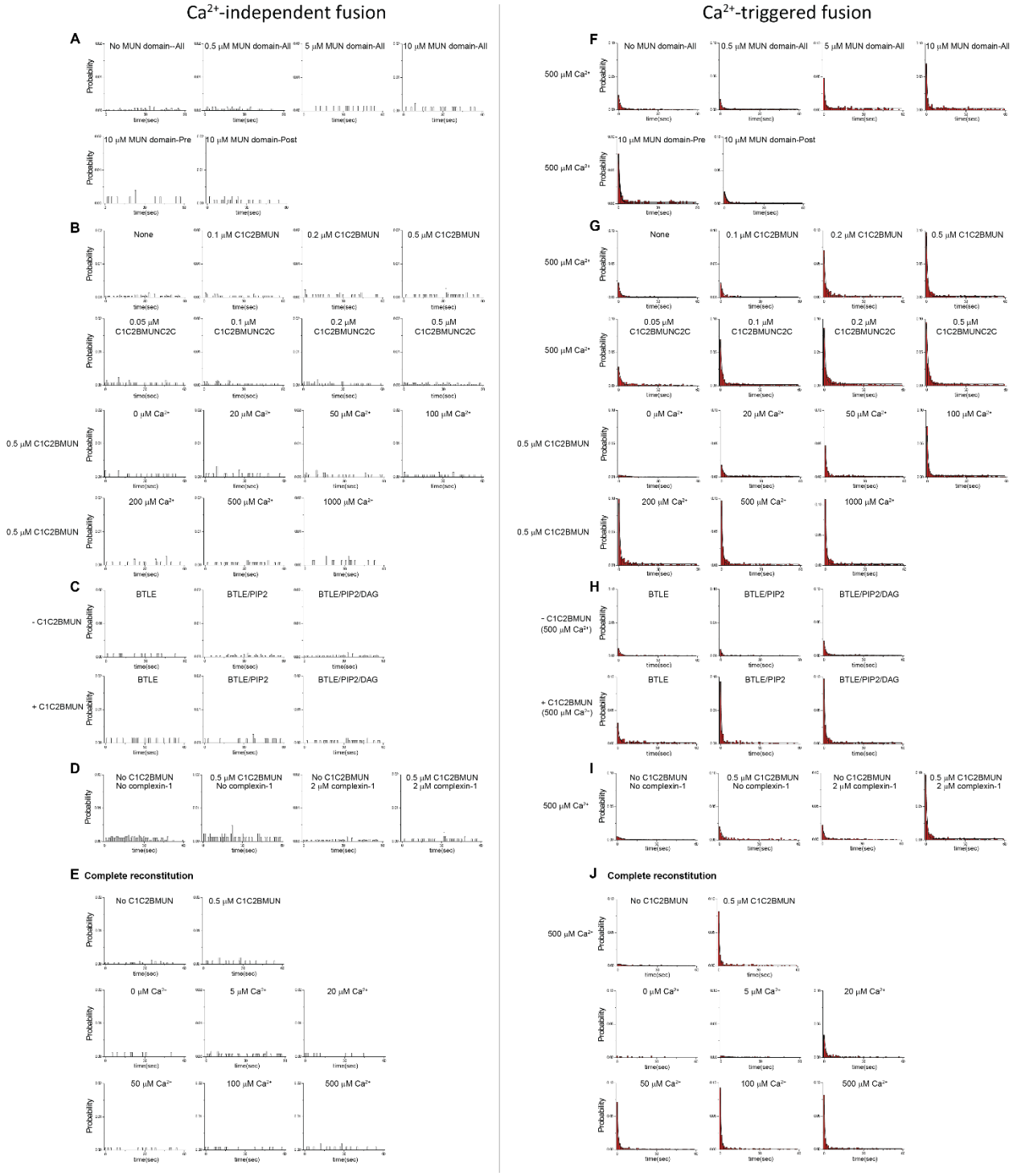
Ca2+-independent fusion
Ca2+-triggered fusion
A
No MUN domain--All
0.5 μM MUN domain-All
5 μM MUN domain-All
10 μM MUN domain-All
10 μM MUN domain-Pre
10 μM MUN domain-Post
B
None
0.1 μM C1C2BMUN
0.2 μM C1C2BMUN
0.5 μM C1C2BMUN
0.05 μM C1C2BMUNC2C
0.1 μM C1C2BMUNC2C
0.2 μM C1C2BMUNC2C
0.5 μM C1C2BMUNC2C
0 μM Ca2+
20 μM Ca2+
50 μM Ca2+
100 μM Ca2+
200 μM Ca2+
500 μM Ca2+
1000 μM Ca2+
0.5 μM C1C2BMUN
C
BTLE
BTLE/PIP2
BTLE/PIP2/DAG
- C1C2BMUN
+ C1C2BMUN
D
No C1C2BMUN
No complexin-1
0.5 μM C1C2BMUN
No complexin-1
No C1C2BMUN
2 μM complexin-1
0.5 μM C1C2BMUN
2 μM complexin-1
E Complete reconstitution
No C1C2BMUN
0.5 μM C1C2BMUN
0 μM Ca2+
5 μM Ca2+
20 μM Ca2+
50 μM Ca2+
100 μM Ca2+
500 μM Ca2+
F
No MUN domain-All
0.5 μM MUN domain-All
5 μM MUN domain-All
10 μM MUN domain-All
500 μM Ca2+
10 μM MUN domain-Pre
10 μM MUN domain-Post
G
None
0.1 μM C1C2BMUN
0.2 μM C1C2BMUN
0.5 μM C1C2BMUN
0.05 μM C1C2BMUNC2C
0.1 μM C1C2BMUNC2C
0.2 μM C1C2BMUNC2C
0.5 μM C1C2BMUNC2C
0 μM Ca2+
20 μM Ca2+
50 μM Ca2+
100 μM Ca2+
200 μM Ca2+
500 μM Ca2+
1000 μM Ca2+
0.5 μM C1C2BMUN
H
BTLE
BTLE/PIP2
BTLE/PIP2/DAG
- C1C2BMUN (500 μM Ca2+)
+ C1C2BMUN (500 μM Ca2+)
I
No C1C2BMUN
No complexin-1
0.5 μM C1C2BMUN
No complexin-1
No C1C2BMUN
2 μM complexin-1
0.5 μM C1C2BMUN
2 μM complexin-1
500 μM Ca2+
J Complete reconstitution
No C1C2BMUN
0.5 μM C1C2BMUN
500 μM Ca2+
0 μM Ca2+
5 μM Ca2+
20 μM Ca2+
50 μM Ca2+
100 μM Ca2+
500 μM Ca2+
Probability
time(sec)

Figure S2. Histograms for Ca^{2+}-independent fusion and Ca^{2+}-triggered fusion. Related to Figures 2, 3, 6, S6, and S7. Experiments were performed in the presence of both synaptotagmin-1, 2 μM full-length complexin-1 and neuronal SNAREs, and in the absence or presence of MUN domain, C1C2BMUN fragment or SNAP-25A as indicated. (A-E) The histograms show the probability of fusion in the absence of Ca^{2+}. Note that the specified Ca^{2+} concentrations refer to a particular experiment, the measurement was performed at 0 μM Ca^{2+} concentration before Ca^{2+} triggering. (F-J) The histograms show the probability of fusion upon 500 μM Ca^{2+}-injection. Both the Ca^{2+}-independent fusion and the Ca^{2+}-triggered fusion histograms (1 second time bins) were cumulated over the 1 min acquisition period for all rounds and repeat experiments and then normalized with respect to the number of analyzed SV-PM vesicle pairs. The Ca^{2+}-triggered histograms were fit to an exponential decay function and the resulting decay rates are shown in the "synchronization" panels in Figures 2, 3, 6, S6 and S7. The number of independent repeat experiments and analyzed SV-PM vesicle pairs are provided in Tables S3-S4 and S7. BTLE: Brain Total Lipid Extract.

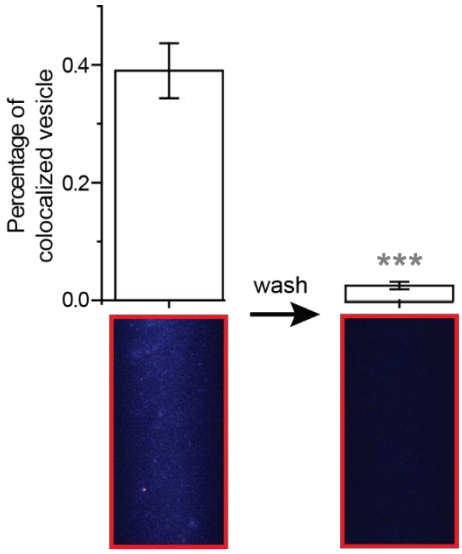

Figure S3. The protocol "Pre" removes all MUN domain molecules after vesicle association. Related to Figure 2. The experimental scheme is identical to the protocol "Pre" shown in Figure 2A, except that 500 nM of labeled MUN domain was mixed with 9.5 μM unlabeled MUN domain. Labeling was performed with the Alexa 647 fluorescent dye by covalently linking it to the primary amino group. The bar graphs show the percentage of labeled MUN domain molecules bound to associated SV-PM vesicle pairs before or after MUN domain-free buffer wash. The corresponding images show the fluorescence intensities of the Alexa 647 labeled MUN domain molecules. Error bars are standard deviations from 10 random imaging locations in the same sample channel. *** $p < 0.001$ by Student's t-test.

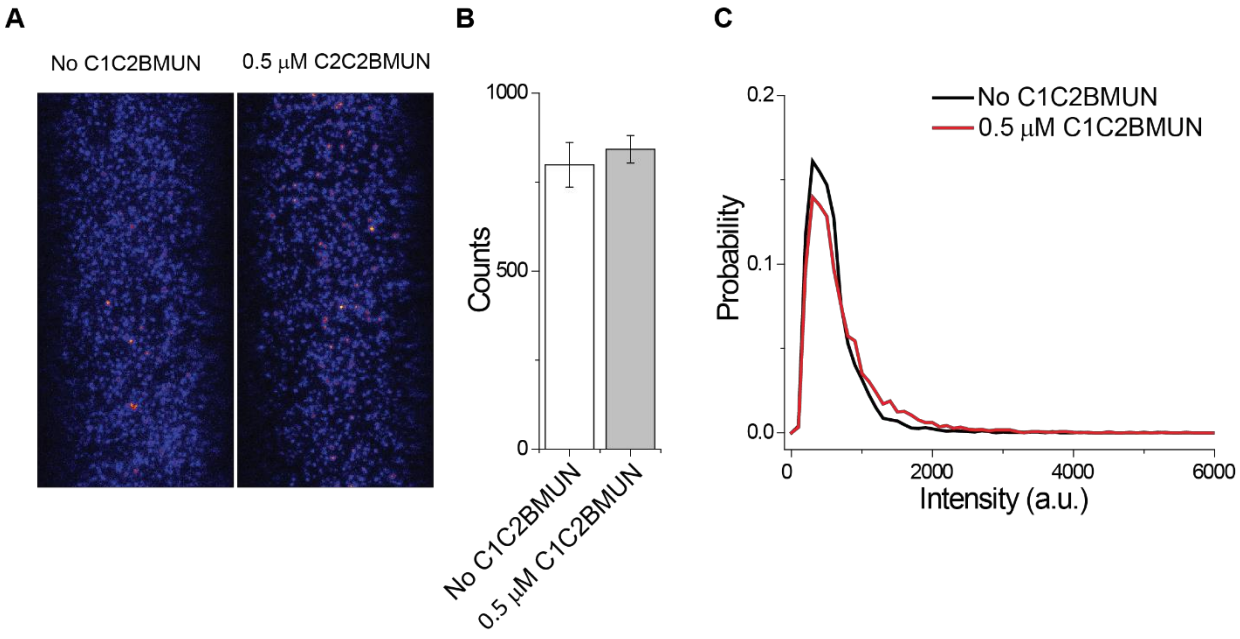

Figure S4. The C1C2BMUN fragment at 0.5 μM does not cause clustering of PM vesicles in solution. Related to Figure 3. (A) Shown are representative fields of view of surface-tethered PM vesicles that labeled with DiD and that were incubated with or without 0.5 μM C1C2BMUN fragment prior to tethering. (B) Average number and standard deviations of spots from 10 randomly chosen fields of view in the sample chamber. Each spot corresponds to at least one surface-tethered PM vesicle. When specified, PM vesicles were incubated with 0.5 μM C1C2BMUN prior to tethering. (C) Probability distribution of the spot intensities obtained from the 10 randomly chosen fields of view.

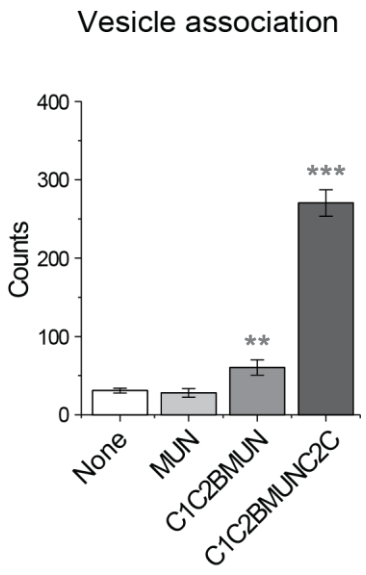

Figure S5. Inclusion of the C2C domain in a Munc13 fragment enhances vesicle association. Related to Figure 3. The bar graphs show the effects of 0.5 μM MUN domain, C1C2BMUN fragment, or C1C2BMUNC2C fragment on the vesicle association between PM vesicles and synaptobrevin-2 reconstituted vesicles with the same lipid composition as that of SV vesicles. Error bars are standard deviations from 10 random imaging locations in the same sample channel. ** $p < 0.01$, *** $p < 0.001$ by Student's t-test, compared to the experiment without Munc13 fragments.

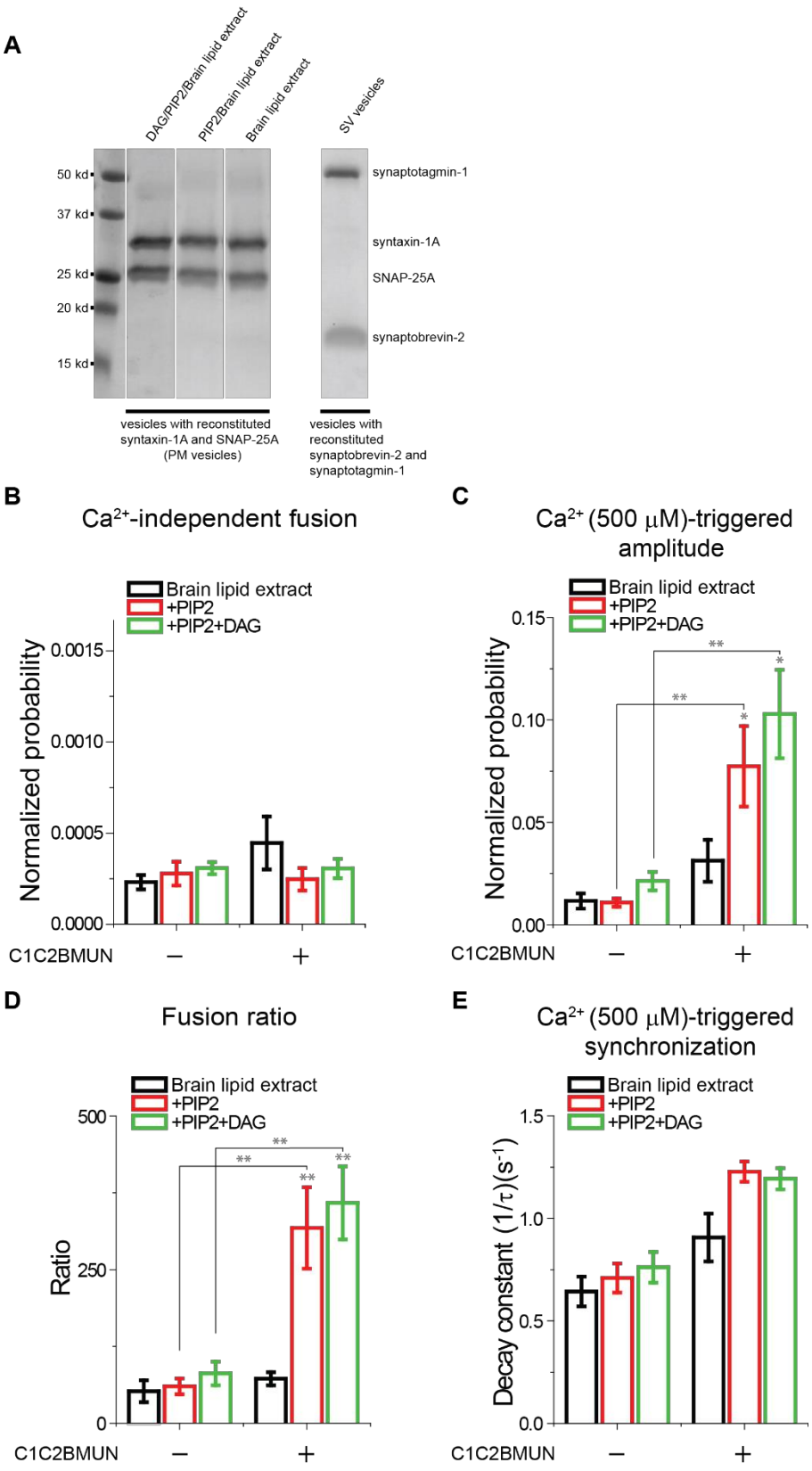
A
DAG/PIP2/Brain lipid extract
PIP2/Brain lipid extract
Brain lipid extract
SV vesicles
50 kd
37 kd
25 kd
20 kd
15 kd
synaptotagmin-1
syntaxin-1A
SNAP-25A
synaptobrevin-2
vesicles with reconstituted syntaxin-1A and SNAP-25A (PM vesicles)
vesicles with reconstituted synaptobrevin-2 and synaptotagmin-1
B
Ca2+-independent fusion
Brain lipid extract
+PIP2
+PIP2+DAG
Normalized probability
0.0015
0.0010
0.0005
0.0000
C1C2BMUN
–
+
C
Ca2+ (500 μM)-triggered amplitude
Brain lipid extract
+PIP2
+PIP2+DAG
Normalized probability
0.15
0.10
0.05
0.00
**
*
C1C2BMUN
–
+
D
Fusion ratio
Brain lipid extract
+PIP2
+PIP2+DAG
Ratio
500
250
0
**
C1C2BMUN
–
+
E
Ca2+ (500 μM)-triggered synchronization
Brain lipid extract
+PIP2
+PIP2+DAG
Decay constant (1/τ)(s-1)
1.5
1.0
0.5
0.0
C1C2BMUN
–
+

Figure S6. Both PIP2 and DAG contribute to the activity of C1C2BMUN. Related to Figure 3. The experimental scheme is identical to that shown in Figure 3A except that different lipid compositions of the PM vesicles are used. (A) SDS-PAGE gel electrophoresis of SV and PM vesicles with reconstituted synaptic proteins. (B-E) The bar graphs show the effects of 0.5 μM C1C2BMUN fragment on the average probability of Ca^{2+}-independent fusion events per second (B), the amplitude of the first 1-sec time bin upon 500 μM Ca^{2+}-injection (C), the ratio of the Ca^{2+}-triggered amplitude to the average probably of Ca^{2+}-independent fusion per second (D), and the decay rate ($1/\tau$) of the histogram upon Ca^{2+}-injection (E). The fusion probabilities and amplitudes were normalized with respect to the corresponding number of analyzed SV-PM vesicle pairs (Table S4). Individual histograms are in Figure S2C and S2H. Panels B-D show means ± SD for multiple independent repeat experiments (Table S4). Panel E shows decay constants and error estimates computed from the covariance matrix upon fitting the corresponding histograms with a single exponential decay function using the Levenberg-Marquardt algorithm. * $p < 0.05$, ** $p < 0.01$ by Student's t-test between the specified experiments (brackets).

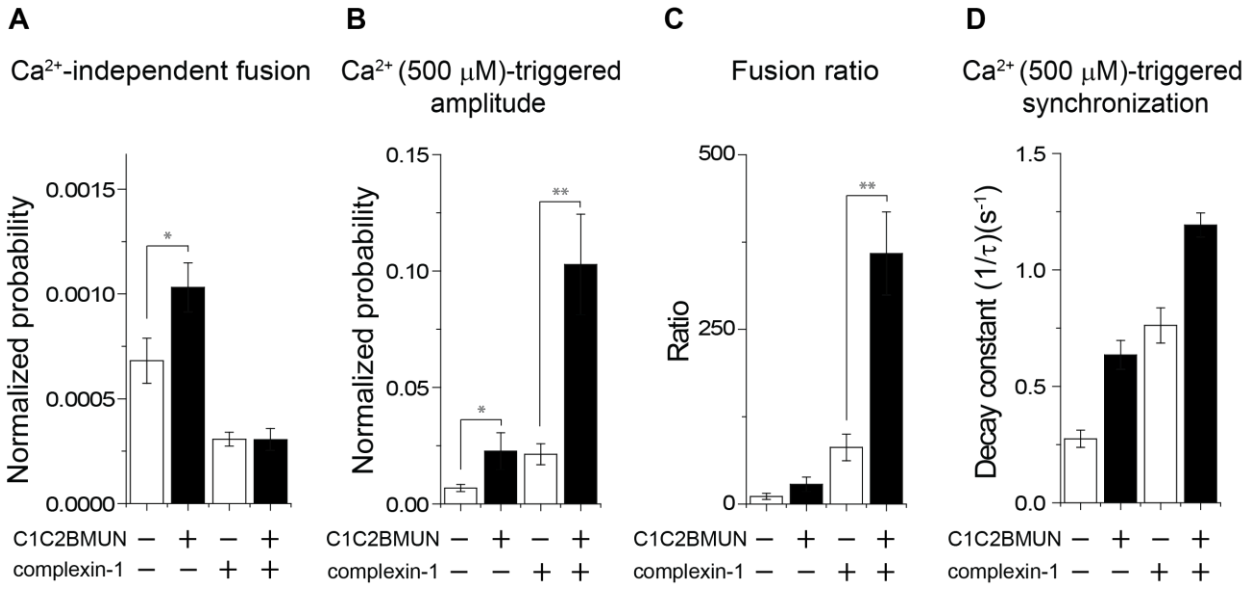

Figure S7. C1C2BMUN increases both Ca^{2+}-independent and triggered fusion probabilities in the absence of complexin-1. Related to Figure 3. The experimental scheme is identical to that shown in Figure 3A except that 2 μM complexin-1 is absent in the specified conditions. (A-D) The bar graphs show the effects of 0.5 μM C1C2BMUN fragment on the average probability of Ca^{2+}-independent fusion events per second (A), the amplitude of the first 1-sec time bin upon 500 μM Ca^{2+}-injection (B), the ratio of the Ca^{2+}-triggered amplitude to the average probably of Ca^{2+}-independent fusion per second (C), and the decay rate ($1/\tau$) of the histogram upon Ca^{2+}-injection (D). The fusion probabilities and amplitudes were normalized with respect to the corresponding number of analyzed SV-PM vesicle pairs (Table S4). Individual histograms are in Figures S2D and S2I. Panels A-C show means ± SD for multiple independent repeat experiments (Table S4). Panel D shows decay constants and error estimates computed from the covariance matrix upon fitting the corresponding histograms with a single exponential decay function using the Levenberg-Marquardt algorithm. * $p < 0.05$, ** $p < 0.01$ by Student's t-test between the specified experiments (brackets). The data in the presence of C1C2BMUN are identical to those shown in Figure 3 and are included here for comparison.

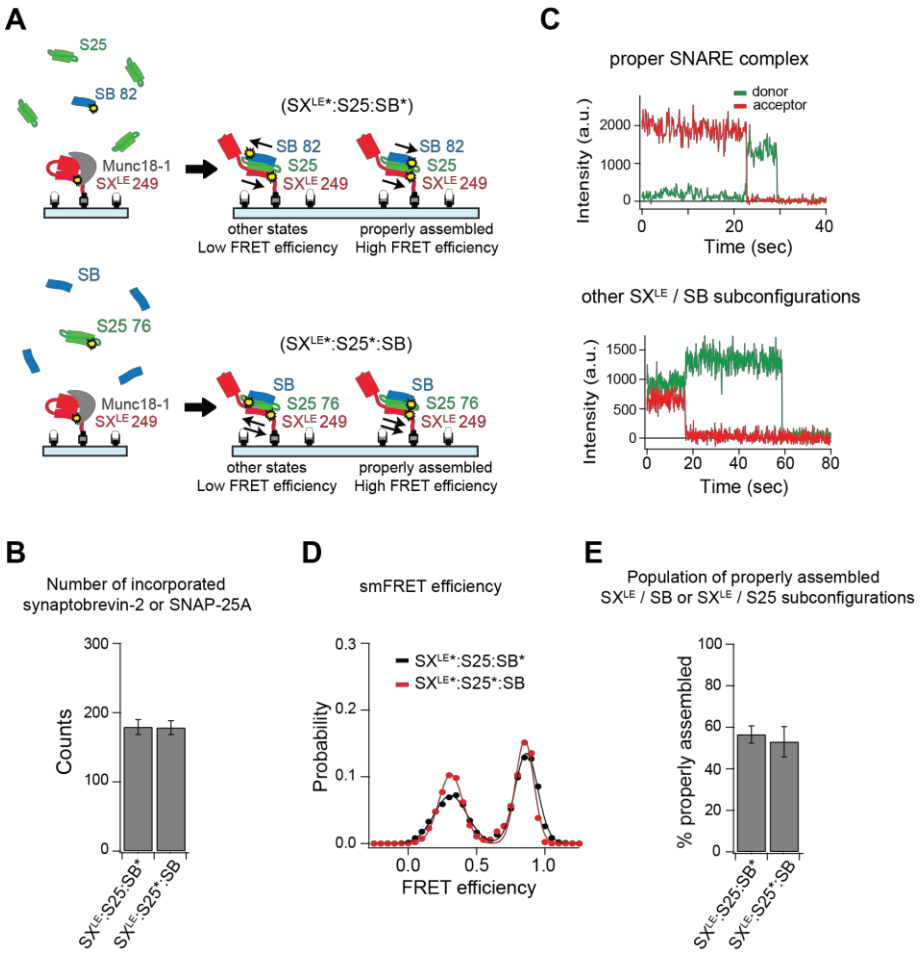

Figure S8. Transfer of syntaxin-1A^{LE} into the ternary SNARE complex beginning from syntaxin-1A^{LE} / Munc18-1 in the absence of Munc13-1 results in mixed SNARE configurations. Related to Figure 7. (A) The cytoplasmic domain of syntaxin-1A^{LE} (SX^{LE}) was tethered on a PEG-passivated microscope slide via streptavidin-biotin linkage. Munc18-1 was added to assemble the SX^{LE} / Munc18-1 complex. SNAP-25A (S25) and the cytoplasmic domain of synaptobrevin-2 (SB) were then added to form ternary SNARE complex. The configurations of the resulting ternary SNARE complex were probed by single molecule experiments. The yellow dots and the asterisks (*) indicate fluorescently labeled residues. The thin arrows represent parallel or antiparallel SX / SB (top panel) or SX / S25 (bottom panel) subconfigurations. The labeling sites are SX^{LE} residue 249, SB residue 82, and S25 residue 76. (B) Beginning with surface tethered SX^{LE} / Munc18-1 complex, SB or S25 incorporation into the ternary SNARE^{LE} complex was measured by counting the number of Alexa-555-labeled SB or Alexa-555-labeled S25 molecules in presence of unlabeled S25 or unlabeled SB, respectively. Shown are means of the counts from three snapshots ± SD (Table S1). (C) Representative fluorescence intensity time traces of properly (top panel) and improperly (bottom panel) assembled SNARE^{LE} complex that were formed starting from surface-tethered SX^{LE} / Munc18-1 complexes. (D) smFRET efficiency histograms for labels attached to SX^{LE} (labeled with Alexa 647) and SB (labeled with Alexa 555) or SX^{LE} (labeled with Alexa 647) and S25 (labeled with Alexa 555). (E) Percent of

properly assembled SX^{LE} / SB or SX^{LE} / S25 subconfigurations. Shown are means ± SD for the two subsets of an equal partition of the data (Table S2).

Table S1. Data summary table for results related to Figures 1C, 1H, 4B, 4F, and S8B: incorporation of labeled synaptobrevin-1 or SNAP-25A into the ternary SNARE complex.

	Alexa 555 label site	conditions	Counts
SX-S25-SB*	SB 82	none	184.0 ± 12.8
SX-S25-SB*	SB 82	0.5 μM MUN	199.6 ± 16.0
SX-S25-SB*	SB 82	10.0 μM MUN	209.6 ± 10.5
SX-S25-SB*	SB 82	10.0 μM BSA	207.8 ± 10.0
SX-S25*-SB	S25 76	none	181.0 ± 8.5
SX-S25*-SB	S25 76	0.5 μM MUN	176.0 ± 10.1
SX-S25*-SB	S25 76	10.0 μM MUN	172.3 ± 16.2
SX-S25*-SB	S25 76	10.0 μM BSA	173.7 ± 17.8
SX-S25-SB*	SB 82	Munc18-1	22.3 ± 3.8
SX-S25-SB*	SB 82	Munc18-1 + 0.5 μM MUN	61.7 ± 8.1
SX-S25-SB*	SB 82	Munc18-1 + 10.0 μM MUN	239.3 ± 19.3
SX-S25-SB*	SB 82	Munc18-1 + 10.0 μM BSA	47.0 ± 2.0
SX-S25*-SB	S25 76	Munc18-1	39.3 ± 2.1
SX-S25*-SB	S25 76	Munc18-1 + 0.5 μM MUN	104.7 ± 8.7
SX-S25*-SB	S25 76	Munc18-1 + 10.0 μM MUN	336.7 ± 8.5
SX-S25*-SB	S25 76	Munc18-1 + 10.0 μM BSA	37.0 ± 4.6
SX^{LE}-S25-SB*	SB 82	Munc18-1	179.3 ± 10.8
SX^{LE}-S25*-SB	S25 76	Munc18-1	178.3 ± 10.0

Table S2. Data summary table for results related to Figures 1E, 1F, 1J, 1K, 4C, 4D, 4G, 4H, and S8E: percent properly assembled syntaxin-1A / synaptobrevin-2 or syntaxin-1A / SNAP-25A subconfiguration.

	Alexa 647 label site	Alexa 555 label site	conditions	percent properly assembled	Number of analyzed traces
SX*-S25-SB*	SX 249	SB 82	none	56.9 ± 5.0	82
SX*-S25-SB*	SX 249	SB 82	0.5 µM MUN	72.4 ± 2.1	84
SX*-S25-SB*	SX 249	SB 82	10.0 µM MUN	90.9 ± 1.2	92
SX*-S25-SB*	SX 249	SB 82	10.0 µM BSA	57.3 ± 2.1	84
SX*-S25*-SB	SX 249	S25 76	none	57.6 ± 3.2	83
SX*-S25*-SB	SX 249	S25 76	0.5 µM MUN	58.8 ± 4.5	101
SX*-S25*-SB	SX 249	S25 76	10.0 µM MUN	57.8 ± 3.1	130
SX*-S25*-SB	SX 249	S25 76	10.0 µM BSA	54.0 ± 1.8	99
SX*-S25-SB*	SX 249	SB 82	Munc18-1 + 0.5 µM MUN	95.8 ± 6.0	23
SX*-S25-SB*	SX 249	SB 82	Munc18-1 + 10 µM MUN	94.9 ± 0.6	69
SX*-S25*-SB	SX 249	S25 76	Munc18-1 + 0.5 µM MUN	95.9 ± 5.8	26
SX*-S25*-SB	SX 249	S25 76	Munc18-1 + 10 µM MUN	93.8 ± 2.4	179
SX*^{LE}-S25-SB*	SX^{LE} 249	SB 82	Munc18-1	56.5 ± 4.1	79
SX*^{LE}-S25-SB*	SX^{LE} 249	SB 82	Munc18-1 + 10 µM MUN	89.9 ± 2.3	99
SX*^{LE}-S25*-SB	SX^{LE} 249	S25 76	Munc18-1	53.0 ± 7.3	74
SX*^{LE}-S25*-SB	SX^{LE} 249	S25 76	Munc18-1 + 10 µM MUN	53.9 ± 2.4	87

Table S3. Data summary table for the fusion experiments related to Figure 2¶.

(PM vesicles)	Ca^{2+}-independent fusion events	Ca^{2+}-triggered fusion events	Number of analyzed SV-PM vesicle pairs	Repeats *n*
No MUN domain, protocol All	45	272	2945	6
0.5 µM MUN domain, protocol All	34	172	1903	4
5 µM MUN domain, protocol All	14	144	687	3
10 µM MUN domain, protocol All	18	219	902	4
10 µM MUN domain, protocol Pre	11	124	506	4
10 µM MUN domain, protocol Post	22	87	952	3

¶Among each repeat experiment there are at least three different protein preps and vesicle reconstitutions, so the variations observed in the bar charts reflect sample variations as well as variations among different flow chambers. For the definition of the repeat experiments see STAR Methods.

Table S4. Data summary table for the fusion experiments related to Figures 3, S6 and S7¶.

(PM vesicles)	Ca^{2+}-independent fusion events	Ca^{2+}-triggered fusion events	Number of analyzed SV-PM vesicle pairs	Repeats *n*
None	45	272	2945	6
0.1 µM C1C2BMUN	33	209	2173	6
0.2 µM C1C2BMUN	22	301	1338	6
0.5 µM C1C2BMUN	29	326	1357	9
0.05 µM C1C2BMUNC2C	31	151	1263	4
0.1 µM C1C2BMUNC2C	38	433	1842	6
0.2 µM C1C2BMUNC2C	33	404	1536	5
0.5 µM C1C2BMUNC2C	53	580	2374	6
0 µM Ca^{2+}	19	39	1035	3
20 µM Ca^{2+}	19	99	936	3
50 µM Ca^{2+}	25	227	1441	7
100 µM Ca^{2+}	28	290	1345	5
200 µM Ca^{2+}	18	307	1123	4
500 µM Ca^{2+}	29	326	1357	9
1000 µM Ca^{2+}	15	210	736	4
BTLE only (No C1C2BMUN)	13	58	942	3
BTLE/PIP2 (No C1C2BMUN)	35	160	2647	5
BTLE/PIP2/DAG (No C1C2BMUN)	45	272	2945	6
BTLE only (C1C2BMUN)	18	101	671	3
BTLE/PIP2 (C1C2BMUN)	16	151	772	5
BTLE/PIP2/DAG (C1C2BMUN)	29	326	1357	9
No C1C2BMUN (No complexin-1)	97	113	2038	4
0.5 µM C1C2BMUN (No complexin-1)	51	94	837	6
No C1C2BMUN (2 µM complexin-1)	45	272	2945	6
0.5 µM C1C2BMUN (2 µM complexin-1)	29	326	1357	9

¶Among each repeat experiment there are at least three different protein preps and vesicle reconstitutions, so the variations observed in the bar charts reflect sample variations as well as variations among different flow chambers. For the definition of the repeat experiments see STAR Methods. BTLE: Brain Total Lipid Extract.

Table S5. Data summary table for results related to Figures 5D-5G: percent closed state of syntaxin-1A in the presence of accessory proteins.

Initial complex	Disassembly factors (NSF, αSNAP, ATP, Mg^{2+})	Accessory protein	FRET efficiency	percent closed state	Number of analyzed traces
SX	none	none	E_1= 0.13 ± 0.13 E_2= 0.41 ± 0.15 E_3= 0.71 ± 0.15	13.3± 0.4	155
SX	none	S25	E_1= 0.13 ± 0.13 E_2= 0.37 ± 0.07 E_3= 0.71 ± 0.15	12.9 ± 3.7	70
SX	none	Munc18-1	E_1= 0.13 ± 0.14 E_2= 0.44 ± 0.16 E_3= 0.71 ± 0.13	80.6 ± 2.5	132
SX-S25	Yes	none	E_1= 0.13 ± 0.11 E_2= 0.55 ± 0.19 E_3= 0.71 ± 0.16	4.1 ± 0.2	101
SX-S25	Yes	Munc18-1	E_1= 0.13 ± 0.10 E_2= 0.36 ± 0.11 E_3= 0.71 ± 0.13	90.1 ± 4.2	107
SX-S25	Yes (– Mg^{2+})	Munc18-1	E_1= 0.13 ± 0.13 E_2= 0.40 ± 0.06 E_3= 0.71 ± 0.18	12.3 ± 3.8	51

Table S6. Steady-state fluorescence anisotropy measurements of labeled syntaxin-1A related to Figure 5¶.

Constructs	Steady state anisotropy (r)
Alexa 555	0.19 ± 0.01
Alexa 555 (linked to SX 35:249)	0.21 ± 0.01
Alexa 555 (linked to SX 35:249) + 1 µM S25	0.21 ± 0.02
Alexa 555 (linked to SX 35:249) + 1 µM Munc18-1	0.20 ± 0.03
Alexa 555 (linked to SX 35:249) + 1 µM NSF + 10 µM αSNAP + 1 mM ATP + 1 mM Mg^{2+}	0.21 ± 0.01
Alexa 555 (linked to SX 35:249) + 1 µM NSF + 10 µM αSNAP + 1 mM ATP + 1 mM Mg^{2+} + 1 µM Munc18-1	0.20 ± 0.02
Alexa 647	0.12 ± 0.10
Alexa 647 (linked to SX 35:249)	0.17 ± 0.06
Alexa 647 (linked to SX 35:249) + 1 µM S25	0.17 ± 0.09
Alexa 647 (linked to SX 35:249) + 1 µM Munc18-1	0.16 ± 0.07
Alexa 647 (linked to SX 35:249) + 1 µM NSF + 10 µM αSNAP + 1 mM ATP + 1 mM Mg^{2+}	0.18 ± 0.03
Alexa 647 (linked to SX 35:249) + 1 µM NSF + 10 µM αSNAP + 1 mM ATP + 1 mM Mg^{2+} + 1 µM Munc18-1	0.16 ± 0.08

¶Steady state fluorescence anisotropy measurements of Alexa 555 or Alexa 647 dyes linked to syntaxin-1A (SX) at both residues 35 and 249, either in isolation or in presence accessory proteins at the specified concentrations. SNAP-25A (S25), Munc18-1, or the disassembly factors NSF / αSNAP / ATP / $MgCl_2$ did not affect the fluorescence anisotropy of Alexa 555 or Alexa 647 labeled SX at residues 35 and 249 (SX 35:249). Shown are the means ± SD for n = 3 replicates.

Table S7. Data summary table for the fusion experiments related to Figure 6¶

(complete reconstitution)	Ca^{2+}-independent fusion events	Ca^{2+}-triggered fusion events	Number of analyzed SV-PM vesicle pairs	Repeats *n*
No C1C2BMUN	22	82	2244	4
0.5 µM C1C2BMUN	16	171	1018	6

(complete reconstitution)	Ca^{2+}-independent fusion events	Ca^{2+}-triggered fusion events	Number of analyzed SV-PM vesicle pairs	Repeats *n*
0 µM Ca^{2+}	8	12	773	4
5 µM Ca^{2+}	20	36	1245	4
20 µM Ca^{2+}	9	84	862	4
50 µM Ca^{2+}	13	209	1327	5
100 µM Ca^{2+}	14	200	1100	4
500 µM Ca^{2+}	16	171	1018	6

¶Among each repeat experiment there are at least three different protein preps and vesicle reconstitutions, so the variations observed in the bar charts reflect sample variations as well as variations among different flow chambers. For the definition of the repeat experiments see STAR Methods.